# The radiation balance of Midmar Dam in KwaZulu-Natal, South Africa

**by**

**LINDUMUSA MYENI**

**Submitted in fulfilment of the academic requirements of**

**Master of Science**

in Agrometeorology

School of Agricultural, Earth and Environmental Sciences

College of Agriculture, Engineering and Science

University of KwaZulu-Natal

Pietermaritzburg

South Africa

November 2016

## PREFACE

The research contained in this dissertation was completed by the candidate while based in the Discipline of Agrometeorology, School of Agricultural, Earth and Environmental Sciences of the College of Agriculture, Engineering and Science, University of KwaZulu-Natal, Pietermaritzburg Campus, South Africa. The research was financially supported by Water Research Commission and National Research Foundation.

The contents of this work have not been submitted in any form to another university and, except where the work of others is acknowledged in the text, the results reported are due to investigations by the candidate.

_____

Signed: Professor MJ Savage

Date: 21 November 2016

## DECLARATION 1: PLAGIARISM

I, I, Lindumusa Myeni, declare that:

(i) the research reported in this dissertation, except where otherwise indicated or acknowledged, is my original work;

(ii) this dissertation has not been submitted in full or in part for any degree or examination to any other university;

(iii) this dissertation does not contain other persons' data, pictures, graphs or other information, unless specifically acknowledged as being sourced from other persons;

(iv) this dissertation does not contain other persons' writing, unless specifically acknowledged as being sourced from other researchers. Where other written sources have been quoted, then:

a) their words have been re-written but the general information attributed to them has been referenced;

b) where their exact words have been used, their writing has been placed inside quotation marks, and referenced;

(v) where I have used material for which publications followed, I have indicated in detail my role in the work;

(vi) this dissertation is primarily a collection of material, prepared by myself, published as journal articles or presented as a poster and oral presentations at conferences. In some cases, additional material has been included;

(vii) this dissertation does not contain text, graphics or tables copied and pasted from the Internet, unless specifically acknowledged, and the source being detailed in the dissertation and in the References sections.

_____

Signed: Lindumusa Myeni

Date: 21 November 2016

## DECLARATION 2: PUBLICATIONS

My role in each paper and presentation is indicated. The * indicates corresponding author.

1. Savage MJ, Pasi JM, Myeni L*, Clulow AD. Monin-Obukhov Similarity Method for Open Water Evaporation. Paper presentation to 18th SANCIAHS Symposium, Durban, South Africa in September 2016. Presented by MJ Savage.
2. Savage MJ, Pasi JM, Myeni L*, Clulow AD. 2016. Open water evaporation measurement using micrometeorological methods. Unpublished Water Research Commission Report No. K5/2335.

## ABSTRACT

Energy balance models driven by the difference between net irradiance ($R_n$) and water-stored heat flux ($G$), the available energy flux, are the most accurate methods of estimating open water evaporation after the direct measurement of open water evaporation and are often used as a reference method against which other methods are compared. However, measurements of the available energy flux above water storage may not be readily available. The available energy flux is measured directly with greater difficulty because it involves significant financial investment in instrumentation and extensive field work on a reservoir. The lack of the available energy flux data above water storages could be solved by using the models that estimate available energy flux from meteorological data that is readily available in most standard weather stations.

The modified Penman-Monteith model seems to be the most promising technique to estimate the available energy flux for open water evaporation from different water storages of different sizes. The modified Penman-Monteith model utilises the concepts of equilibrium temperature to estimate the water-body temperature of the storage using an iterative procedure. The estimated water-body temperature is essential for computing $G$ and the outgoing infrared irradiance ($L_u$) from the water surface. Therefore, in this study, the Daily Penman, Monteith, Equilibrium Temperature Hargreaves-Samani (DPMETHS) model, implemented in Excel to incorporate the daily solar radiation estimation model which utilizes the daily minimum and maximum air temperature to infill any gaps of missing solar irradiance data was used to estimate the available energy flux. The DPMETHS model to estimate the available energy flux for open water evaporation is on its developmental stage and has not been used in any known study. Therefore, there was a need to evaluate the performance of the DPMETHS model to estimate the available energy flux above water from different climatic conditions using the land-based meteorological data. However, there was a vital need to understand the factors enhancing temporal and spatial variability of the radiation balance at water storage to model available energy flux at water storage with confidence.

The net radiation balance is the balance between the net solar radiation and net infrared radiation under steady atmospheric conditions

Measurements of the available energy flux above open water were performed from 12th February to 4th April in 2016 at Midmar Dam, KwaZulu-Natal, South Africa. Radiative fluxes acquired using the net radiometer were accompanied by water temperature profile measurements from which $G$ was computed. The results of this study showed that the solar irradiance ($R_s$) was the dominant component of $R_n$ during the day while infrared irradiance was the dominant component of $R_n$ during night. The cloud cover, reflection coefficient of water, air temperature and surface water temperature ($SWT$) were the main factors that control the temporal and spatial variability of the radiation balance above open water surface. The spatial variation of $R_n$ above open water was mainly due to the spatial variability in $SWT$ since with constant emissivity, $L_u$ depends on $SWT$ alone. The *in-situ* measurement of $SWT$ compared well to the Landsat-8 estimate of $SWT$. The observed average of 1.5 to 2 $^oC$ variability of $SWT$ across Midmar Dam implies the very low spatial variability of $L_u$ which is temperature dependent. Therefore, the low spatial variability of $SWT$ is associated with low spatial variation of $R_n$ across the dam. Despite the high spatial resolution and freely availability of Landsa-8 data, remote sensing methodology still needs calibration and validation with ground truth data and are unlikely to yield daily $R_n$.

The variability of the available energy flux over water indicated that the $R_n$ was the dominant component of the available energy flux at water surface. However, $G$ showed a similar diurnal variation to $R_n$ with comparable magnitudes and peaked at the same time as the peak in $R_n$. During the daytime, $R_n$ fluxes were positive, corresponding to a source of the energy flux while during night-time, $R_n$ fluxes were negative, corresponding to a loss of energy flux from the water surface.

To evaluate the performance of the DPMETHS model to simulate $R_n$ above Midmar Dam, model estimates of $R_n$ were compared to the measurements of $R_n$ above water surface at Midmar Dam. Results indicated a good relationship between the daily estimates of $R_n$ predicted from the DPMETHS model and the daily $R_n$ measured above water, with slope ($m$) of 0.76, regression coefficient exceeding 0.70 and the root mean square error (RMSE) of 3.04 MJ $m^{-2}$. The mean bias error (MBE) of 0.70 MJ $m^{-2}$ indicated that the model often over-simulated $R_n$. The estimated $R_n$ and measured $R_n$ fluxes were not statistically different at the 99.5 % level of confidence. The under-simulation of $R_n$ during overcast days was attributed to under-

simulation of $L_d$ due to poor estimation of cloud fraction using the Brunt's formula that was established only for clear-skies. The relative lack of validity of the assumption that the $SWT$ is equal to the $T_{air}$ together with the use of wind speed measured at the land-based station which was less than the wind speed at water surface as a model inputs resulted in the model under-simulating $L_u$ which resulted on the over-simulation of $R_n$ on some of the days.

Model estimates of $R_n$ were compared to the measurements of $R_n$ for the Stratus station at the eastern Pacific Ocean. Results indicated a good relationship between the daily $R_n$ estimated using the DPMETHS model and $R_n$ measured above ocean, with $m$ of 0.62, regression coefficient exceeding 0.76 and RMSE of 5.67 MJ $m^{-2}$. The MBE of 5.45 MJ $m^{-2}$ indicated that the model often over-simulated $R_n$. The estimated $R_n$ and measured $R_n$ fluxes for the Stratus station at the eastern Pacific Ocean were statistically different at the 99.5 % level of confidence. The over-simulation of $R_n$ at the ocean was attributed to the poor model input data available at the ocean. The presence of the low, thick stratus clouds above the ocean emitted greater $L_d$ than expected and resulted on the poor simulations of $L_d$ at the ocean.

The availability of long-term meteorological dataset at Cedara station near Midmar Dam enables the unique opportunity to investigate the potential impacts of climate change on the radiation balance of Midmar Dam. This study showed evidence of the impacts of climate change on the radiation balance of Midmar Dam. Climate changes attributed to the global increase in the concentrations of total carbon dioxide threaten to increase the long-term air temperatures of the earth with consequent increase in $R_n$ due to increases in $L_d$.

This study showed that $R_n$ can be simulated well from standard weather station data using the DPMETHS model. The DPMETHS model performed successfully on the Midmar Dam study and to a lesser extent at the eastern Pacific Ocean. Despite challenges encountered during this study, results produced are generally acceptable and it is believed that the DPMETHS model can be used to estimate $R_n$ for open water at different climatic conditions. However, a better and reliable method of measuring or estimating $G$ is required since $G$ fluxes were measured with great difficulty using thermocouples. Therefore, model estimates of $G$ were not compared to unreliable measurements of $G$ in this study.

## ACKNOWLEDGMENTS

First and foremost, I would like to thank my loving God for giving me the opportunity to write this dissertation. I would also like to thank my lovely family and empowering friends for their support and for believing in me throughout the study period. I would also like to express my sincere gratitude to my supervisor Prof.  Savage for the continuous support through this research, for his patience, motivation, and immense knowledge.

Several special acknowledgements deserve specific mention:

the staff of the Department of Water and Sanitation offices and KwaZulu-Natal Wildlife at Midmar for allowing the use of their facilities for this work;

this work would not have been possible without the technical support from: JM Pasi (University of KwaZulu-Natal), Dr. AD Clulow (University of KwaZulu-Natal), S Strydom (University of KwaZulu-Natal), NC Mbangiwa (University of KwaZulu-Natal);

Mr B Gijsbertsen (University of KwaZulu-Natal) for his assistance with remote sensing and GIS;

Mrs MA Savage (University of KwaZulu-Natal) for the administration and support towards my research is well acknowledged;

Agriculture Research Council for meteorological data from their nearby stations;

Umgeni Water and Department of Water and Sanitation for supplying water level and surface area data of Midmar Dam during study period;

Woods Hole Oceanographic Institution for the (online) Status data in the eastern Pacific Ocean;

University of KwaZulu-Natal, National Research Foundation, and Water Research Commission (South Africa) as part of project K5/2355 for funding.

## TABLE OF CONTENTS

**Page**

## LIST OF TABLES

**Table** **Page**

## LIST OF FIGURES

**Figure** **Page**

# CHAPTER 1 : INTRODUCTION

## 1.1 Background

South Africa is a water-scarce country where annual evaporation exceeds annual rainfall in most parts of the country. According to DWAF (2013), the mean annual precipitation of 450 mm in South Africa is far below the global mean annual precipitation of about 860 mm. The high temporal and spatial variability of rainfall in semi-arid regions such as South Africa results in water resources being not uniformly distributed throughout the region (Mukheibir, 2007). To ensure water security at various times of the year, water is stored in reservoirs (DWAF, 2013). Water demands due to increases in human population and economic development are projected to increase in the near future, resulting in a greater gap between supply and demand under current water resources management habits which involves storing water in open dams (McKenzie and Craig, 2001). CSIR (2010) reported that about 70 % of the total mean annual runoff is captured in about 569 large dams in South Africa.

Significant amounts of water may be lost from open water storages to the atmosphere as water vapour and this phenomenon is referred to as an open water evaporation (McJannet *et al*., 2013). Schulze (2011) stresses the seriousness of water loss from open water storages in South Africa given the projected increase in evaporation due to climate change reported by Mukheibir and Sparks (2003). Evaporation rates information is required by water resources managers for many different purposes such as irrigation scheduling, management of wetlands, catchment water balance studies, dam design, and municipal and industrial water allocations (Finch and Hall, 2001). Estimation of evaporation rates is important in the study of soil, plant and atmosphere continuum as well as in hydrology and climate studies (McMahon *et al*., 2013). However, water resources managers often overlook the open water evaporation from dam storages, leading to inefficient dam operating rules and poor water allocations (van Dijk and van Vuuren, 2009).

Evaporation is a significant component in the hydrological cycle and it is therefore critical that it can be understood and quantified (Savage *et al*., 2004). There are several methods that have been successfully applied to estimate open water evaporation worldwide. However, each technique applies to a specific spatial and temporal scale, and some are therefore more suitable than others under specific conditions (Tanny *et al*., 2008). According to Savage (2010), currently there is no single accepted method that is reliable and results in adequate resolution

that can provide accurate temporal and spatial evaporation measurements or modelling estimates of open water evaporation. According to Finch and Hall (2001), each method has its own advantages and disadvantages, in terms of the method, theoretical assumptions, accuracy, complexity, cost, fetch requirements and power consumption. The choice of the technique to be used is highly dependent on the availability of data, level of accuracy of the output results and the representation of results (Finch and Hall, 2001).

There is a vital need to develop and improve the relatively inexpensive methods to estimate open water evaporation from readily available measurements with reliable accuracy and acceptable precision to calibrate new technologies. For operational purposes, such as water resources management, irrigation management and hydrologic studies, where near real time estimates of evaporation are needed, the energy balance approach (Eq. 1.1) driven by the available energy flux (i.e. $R_n - G$) seems to be the most promising technique to estimate open water evaporation due to its superior resolution of measurements and data requirements (Huntington and McEvoy, 2011).

$$R_n - G = LE + H \tag{1.1}$$

where $R_n$ is net irradiance (W m$^{-2}$) which is the net balance between the net solar irradiance and the net infrared irradiance at water surface, $G$ is the water-stored heat flux (W m$^{-2}$), $R_n - G$ is the available energy flux for open water evaporation, $E$ is evaporation flux (kg s$^{-1}$ m$^{-2}$, equivalent to mm s$^{-1}$), $L$ = 2.43 MJ kg$^{-1}$ is the specific latent energy of vaporisation and $H$ is the sensible heat flux (W m$^{-2}$).

The energy balance techniques are the most accurate methods of estimating open water evaporation after the direct measurement of the open water evaporation and are often used as a standard method against which other methods are compared (Finch, 2001). Mengistu and Savage (2010) showed that open water evaporation from reservoirs can be computed as a residual of the energy balance, given that $R_n$, $G$ and $H$ fluxes above water surface can be estimated or measured. According to Finch and Calver (2008), the main disadvantage of the energy balance techniques is the large number of the high frequency measurements required and the difficulties in measuring some of them. Consequently, energy balance techniques are a relatively expensive techniques and have only been used in intense research studies. The energy balance techniques for estimating open water evaporation require either estimation or

measurement of the available energy flux which may not be readily available in the water storage of interest, especially in developing countries (Duan, 2014). The lack of the available energy flux data above water storages hinders routine computations of the open water evaporation based on the energy balance methods (McJannet *et al*., 2013). However, McMahon *et al*. (2013) argue that these limitations could be solved by using the models that estimate available energy flux from meteorological data that is readily available in most standard weather stations.

### 1.2 Justification

The Penman model (1948) combines aerodynamic and energy balance aspects, as well as meteorological factors, which can more accurately describe open water evaporation (Jensen, 2010). Monteith (1965) modified the Penman model by including a surface resistance term which resulted in the widely-used Penman-Monteith model. The original Penman model was based on assumption that there was no change in $G$, which resulted in poor estimation of open water evaporation (McCuen and Assmussen, 1973). Finch (2001) stresses the significance of considering $G$ while estimating open water evaporation. Edinger *et al.* (1968) proposed the concept of equilibrium temperature which was defined by Finch (2001) as the equilibrium temperature at which water temperature is being driven to by the net heat exchange. Therefore, for water at the equilibrium temperature, the net heat flux exchange is zero (Finch and Hall, 2001). MacJennet *et al*. (2008) used the concept of equilibrium temperature with the Penman-Monteith model to account for $G$ while assuming that the water body is uniformly mixed with no thermal stratification and the surface resistance of water is zero, and obtained good estimates of open water evaporation from different water storages of different sizes compared to the original Penman-Monteith model. The modified Penman-Monteith model was further developed by Savage *et al.* (2016) and implemented in Excel to incorporate the daily solar radiation estimation model introduced by Hargreaves and Samani (1982) which utilizes the daily minimum and maximum air temperature to infill any gaps of missing solar irradiance data. Therefore, in this study, the Daily Penman, Monteith, Equilibrium Temperature Hargreaves-Samani (DPMETHS) model of Savage *et al.* (2016), assuming energy balance closure, was used to estimate the available energy flux above open water. The development of the DPMETHS model is part of a Water Research Commission (WRC) project which aims to measure and model open water evaporation using land-based meteorological data. This WRC project considered the two aspects of the modelling of the open water evaporation i.e. energy

balance and radiation balance of the water surface. However, the focus of the current study was on the radiation balance of the water surface. The DPMETHS model utilises the concepts of equilibrium temperature to estimate the water-body temperature at the water storage using an iterative procedure. The estimated water-body temperature is essential for computing $G$ and the outgoing infrared irradiance from the water surface (McMahon *et al.*, 2013). Consequently, water-body temperature is one of the paramount parameters in the model and yet it is rarely measured above water storage. Furthermore, the temporal and spatial variability of water-body temperature on water storages are not well understood (Duan, 2014).

The DPMETHS model to estimate the available energy flux for open water evaporation is on its developmental stage and has not been used in any known study. Therefore, the estimates of the available energy flux from the DPEMETS model need to be tested for goodness of fit against measurements of the available energy flux under different climatic conditions before the model can be utilised with confidence to estimate the available energy flux for open water evaporation from the land-based measurements. Unless this is the case, the DPMETHS model is unlikely to be accepted by users other than the model developers. Therefore, there was a need to evaluate the performance of the DPMETHS model to estimate the available energy flux above water at different climatic conditions using the land-based meteorological data. However, there was a vital need to understand the factors enhancing temporal and spatial variability of the radiation balance at water storage for accurate modelling of the available energy flux at water storage.

Climate change is predicted to hit South Africa harder than countries in the north and will be felt first through it impacts on scarce water resources of this region (Schulze, 2011). Climate change has already altered, and will continue to alter the different components of the hydrological cycle such as evaporation (IPCC, 2014). However, the impacts of climate change on evaporation are not yet fully understood given that different components of evaporation will be affected differently (CSIR, 2010). Furthermore, the lack of a long-term record of $R_n$ data over water surface hindered the evaluation of the potential impacts of climate change on the $R_n$, one of the drivers of open water evaporation. The availability of long-term meteorological dataset at Cedara station near Midmar Dam enables the unique opportunity to investigate the potential impacts of climate change on the radiation balance of Midmar Dam. Therefore, this current study also investigates the potential impacts of climate change on the radiation balance of Midmar Dam.

## 1.3 Aim

Available energy flux on water storages is the main driver of the energy balance techniques for estimating open water evaporation and yet are measured with difficulty. The main aim of this study was to understand the factors enhancing temporal and spatial variability of the radiation balance at water storage and to evaluate the performance of the DPMETHS model to simulate the available energy flux above open water at Midmar Dam and for an eastern Pacific Ocean site.

## 1.4 Objectives

- To improve an understanding of the variability of the radiation balance and available energy above open water storage and assessing the factors that affect the radiation balance above open water;
- To evaluate the performance of the DPMETHS model to simulate the daily available energy flux at Midmar Dam and at the ocean Pacific Ocean;
- To investigate the potential impacts of climate change on the radiation balance of Midmar Dam.

## 1.5 Outline of dissertation

Chapter 1 introduces the study with an overview of the significance of an available energy flux on quantifying open water evaporation. The models that have been successfully used to estimate an available energy flux from the standard meteorological data are also introduced.

Chapter 2 provides detailed information on the radiation balance of the open water surfaces and focuses on the factors that control the temporal and spatial variability of the radiation balance components. The theoretical background of measuring and modelling the available energy flux at open water surfaces is also explained explicitly.

Chapter 3 provides the detailed procedure used on both laboratory and outdoor calibrations of the instrumentation at the Agrometeorology Instrument Mast system. The procedure on the

experiment set-up at Midmar Dam is also provided. The detailed procedure for data collection, data processing and data analysis is also explained explicitly.

In Chapter 4 the radiation data acquired from the water-based station were compared against the radiation data from Agrometeorology Instrument Mast system for the same period. The factors that control the temporal and spatial variability of the radiation balance of the Midmar Dam were investigated. The temporal variability of the available energy flux at Midmar Dam was also investigated. Furthermore, the performance of the DPMETHS model to simulate daily radiative fluxes at Midmar Dam and at the ocean was also evaluated.

Chapter 5 provides the summary of the conclusions and recommendations for future research.

# CHAPTER 2 : LITERATURE REVIEW

## 2.1 Radiation balance

### *2.1.1 Introduction*

The net radiation balance is the balance between the net solar radiation and net infrared radiation under steady atmospheric conditions (illustrated in Figure 2.1). This sub-section aims to improve the understanding of the radiation balance at water surfaces. The factors enhancing temporal and spatial variability of the radiation balance at water surfaces are also explained. Furthermore, the methods used to estimate available energy flux are also explained explicitly.

### *2.1.2 Radiation balance above open water surface*

The term radiation refers to the continual emission of energy from the surface of all bodies with temperature greater than 0 K (Liou, 2002). However, Howell *et al.* (2010) defined radiation as the transmission of energy from one body to another by means of electromagnetic waves with or without intervening physical medium. Incoming solar radiation from the sun referred to as shortwave irradiance ($R_s$) may be defined as the radiation in the visible and near-visible portions of electromagnetic spectrum that is within the range of wavelength 250 to 2800 nm (Dozier, 1980). Howell *et al.* (2010) defined $R_s$ which includes both direct and diffuse shortwave radiation as the radiant energy reaching a horizontal plane at the earth's surface. Furthermore, $R_s$ is expressed as energy amount per unit time per unit interval. The diffuse radiation component can be noticed by blocking out the sun's direct rays and observing the diffuse component (Sinclair *et al*., 1992). Liou (2002) referred to the sum of the direct and diffuse components as the total solar radiation (which excludes infrared radiation).

Some of $R_s$ in the form of shortwave radiation reaches the water bodies in diffused form, after scattering by clouds, dust and different gases such as nitrogen, oxygen and ozone in the atmosphere (Allen *et al.*, 1998). Furthermore, part of the $R_s$ that actual reaches the water body is reflected into space (Figure 2.1). The reflection coefficient depends on transient factors, such as the angle of incidence of the solar beam, colour and the nature of the surface (Allen *et al.*, 1998). The reflection coefficient of water is much lower than that of vegetation. Consequently, the water surface absorbs more solar irradiance than vegetation (Arya, 2001). Finch and Hall (2001) reported that about 92% of the solar irradiance striking the surface of the water body is

absorbed. Finch and Calver (2008) argue that the amount of absorption is highly dependent on the wavelength of the radiation i.e. near-infrared radiation is absorbed much less as compared to blue light. The reflection coefficient of water directly determines the amount of solar irradiance absorbed by the water surface (Brutsaert., 2013). According to Allen *et al.* (1998), the reflected solar irradiance cannot be absorbed or transmitted through the water surface. Therefore, reflected solar irradiance is not utilized on water surface.

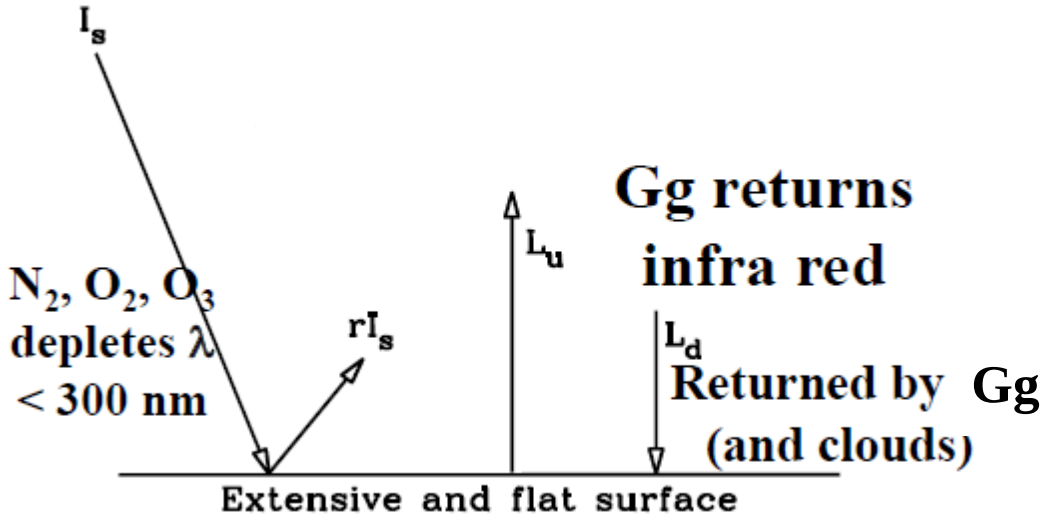


**Figure 2.1: Schematic diagram showing radiation balance on earth's surface, where Gg are the greenhouse gases (Savage, 2012).**

The absorbed solar irradiance from the sun on water surface is converted to heat energy which excites electrons and warms the top layer of water (Jensen, 2010). According to Finch and Calver (2008), most of the solar irradiance is absorbed within the top one meter of the water surface. Water surface is the primary energy storage medium mainly due to its high heat capacity compared to vegetation, soil minerals, and soil organic matter (Brutsaert, 1982). For vegetation, the partioning of the solar irradiance is straight forward and the soil heat flux tends to be relatively small. Therefore, solar irradiance absorbed at the soil surface, is the available energy flux for evaporation. However, for open water, solar irradiance penetrates the water column and absorbed at greater depths and is not immediately available for open water evaporation (Granger and Hedstrom, 2011). The quantity of the solar irradiance that penetrates the water column is highly dependent on the colour of water and turbidity (Finch and Hall,

2001). Finch and Calver (2008) noted that the absorbed solar irradiance is transferred to greater depths through movement from wind and convection while heat is slowly transferred throughout the water column, it often does not reach all the way to the bottom. Furthermore, the lowest strata of water remained near 4 °C, while the surface water temperature fluctuated both diurnally and seasonally (Finch and Calver, 2008).

According to Liou (2002), if the water surface could only absorb energy, the temperature of the water will be infinitely rising. The temperature of water is much lower than that of the sun, therefore, water emits infrared radiation with wavelengths longer than those from the sun (Henderson-Sellers, 1996). Gates (1980) defined emitted infrared radiation ($L_u$) as the radiation originating at terrestrial sources with temperatures ranging between 200 and 370 K and have wavelengths greater than 2800 nm. The quantity of $L_u$ is highly dependent on the surface water temperature, humidity and emissivity at low latitudes (Allen *et al*., 1998). According to Liou (2002), most of the radiant energy emitted by the water surface is contained in the wavelength region of 4000 to 10000 nm and can be explained by Stefan–Boltzmann law based on radiant energy emission by a black body as:

$$L_{u\,wet} = \varepsilon\sigma T^4 \tag{2.1}$$

where $\varepsilon$ is the emissivity of the water surface, $\sigma$ is the Stefan-Boltzmann constant ($5.67\times10^{-8}$ W m$^{-2}$ K$^{-4}$) and $T$ is the surface water temperature of the surface (K).

In the atmosphere, greenhouse gases and clouds selectively transmit, absorbed or reflect $L_u$ (Liou, 2002). According to Kirchhoff's law it is apparent that $L_u$ that is absorbed by the atmosphere would be reradiated (Koberg, 1964). Consequently, greenhouse gases such as water vapour and carbon dioxide on the atmosphere emit infrared radiation in all directions (Koberg, 19964). According to Gates (1980), some of $L_u$ goes back to the water surface while some of it escapes in the atmospheric window into space (Figure 2.1). Ohring and Clapp (1980) defined atmospheric window as the transparent region, with wavelength of about 7000 to 12000 nm where neither water vapour nor carbon dioxide absorb appreciable radiation. Therefore, during clear-skies, energy of that wavelength band passes through the atmosphere unimpeded. According to Stefan-Boltzmann law, if the water surface is warmer than the overlaying atmosphere which is the normal state of affairs, the atmosphere will receive more terrestrial radiation than it emits (Liou, 2002). Arya (2001) reported that about 90 % of the infrared

radiation radiated to space by the earth, is absorbed by the atmosphere. Furthermore, much of this infrared radiation is sent back or counter radiated to the water surface and effectively prevents the water surface from excessive cooling at night. The re-radiation back of infrared radiation to the earth is called the greenhouse effect and keeps the earth's temperature almost constant (Ramanathan *et al*., 1989). Brunt (1934) showed that the incoming infrared irradiance ($L_d$) can be expressed by:

$$L_d = \sigma T^4 \left[0.44 + 0.08 \left(\frac{e_{air}}{100}\right)^{0.5}\right] \tag{2.2}$$

where the emissivity is assumed to be unity, $T$ is the surface air temperature (K) and $e_{air}$ is the atmospheric water vapour pressure (Pa).

According to de Bruin (1982), $R_n$ is given by:

$$R_n = R_s + rR_s - L_u + L_d \tag{2.3}$$

All terms are in W m$^{-2}$. $L_u$ depends on surface water temperature and emissivity while $L_d$ is influenced by atmospheric temperature, humidity, and cloud fraction (Finch and Calver, 2008). The sign conversion used in Eq. (2.3) is that all the radiative fluxes directed toward the water surface are positive while the radiative fluxes directed away from the water surface are negative.

### 2.2 Diurnal and seasonal variability of the radiation balance

The downward components of the radiation balance are controlled by the solar zenith angle which varies with time of the day, season, and latitude (Wang and Liang, 2009). Furthermore, the downward components of the radiation balance are controlled by the atmospheric conditions such as the amount and composition of clouds, atmospheric water vapour amount, and aerosol loading. According to Federer (1968), the downward components of the radiation balance can be assumed to be relatively constant over relatively large surface areas except under partially cloudy skies. The amount of $R_s$ reaching water surface depends on the turbidity of the atmosphere and the presence of clouds which reflect and absorb major parts of the radiation (Finch and Calver, 2008). Therefore, cloud amount and type are important, as well as latitude, season and time of the day in determining the solar radiation reaching water surface. Clouds cover increase scattering and absorption of the solar radiation in the atmosphere (Finch and Hall, 2001). Consequently, less $R_s$ reaches the earth's surface during cloudy or overcast days than during clear-sky days. Allen *et al.* (1998) reported that on clear-sky day, incoming solar radiation is about 75 % of the extraterrestrial radiation while on an overcast day, the radiation

is scattered in the high turbidity atmosphere, however about 25 % of the extraterrestrial radiation may still reach the earth's surface mainly as diffuse sky radiation. The intensity of $R_s$ increases from sunrise until noon and then decrease until sunset and the peak solar energy levels received will vary by latitude and season (Arya, 2001). The intensity of $R_s$ received at the earth's surface depends on the sun and the sun's angle (Blonquist *et al*., 2010). Therefore, different locations of the globe have different typical solar radiation levels in each season. According to Hatzianastassiou and Vardavas (2001), at the beginning of the year the intensity of $R_s$ is high and then slowly drops to their lowest point around June in the southern hemisphere. After June, it begins to rise again for the rest of the year and reach the peak in December or January.

The upward components of the radiation balance are controlled by the water surface characteristics such as reflection coefficient of water surface, water emissivity, surface water temperature ($SWT$) and humidity above the water surface (Finch and Hall, 2001). The fluxes of $R_n$ above water surface shows a substantial daily and seasonal variation (Wang *et al*., 2014). According to Brotzge and Duchon (2000), $R_s$ is the dominant component of $R_n$ during the day. However, infrared irradiance is the dominant component of $R_n$ during night. Mahmud *et al.* (2015) noted that during the daytime, $R_n$ was directed towards the water surface while at night the $R_n$ was much smaller in magnitude and directed away from the water surface. Consequently, the water surface warmed up during the daytime, while it cooled during the night-time, especially during the clear-sky and calm weather conditions.

### *2.1.4 Spatial variability of the net irradiance above water surface*

Sima *et al.* (2013) reported that open water evaporation was under-estimated when point measurements of $SWT$ were used instead of the satellite-derived averaged $SWT$. These results were attributed to the higher shoreline measurements of $SWT$ than the satellite-derived $SWT$ which resulted on over-estimation of the net infrared irradiance which reduced $R_n$. According to Wang *et al.* (2014), any spatial variation of $R_n$ above open water is mainly due to the spatial variability in $SWT$. According to Alcântara *et al*. (2010), the main meteorological factors influencing variability of $SWT$ are solar irradiance and wind speed. However, Kristovich and Laird (1998) argue that cloudless is also one of the significant factors determining variability of $SWT$. Finch and Hall (2001) stresses that the spatial variation in $SWT$ can be large over

fshort-time scales during calm conditions and clear sky days with high solar irradiance. However, Swancar (2015) reported that energy exchange due to water-stored heat flux also had a significant influence on $SWT$ at Lakes Calm and Starr. According to Alcântara *et al*. (2010), during daytime, water near the shore responded to the atmospheric conditions very quickly compared to offshore water. As consequence, water near the shore is always warmer than offshore water. However, during night-time the processes are inverted.

McMahon *et al*. (2013) argued that the $SWT$ data are not readily available at standard automatic weather stations and difficult to measure due to high wind turbulence at water surface. According to Lamaro *et al*. (2013), conducting water temperature surveys using conventional limnological sampling involves significant financial investment in instrumentation and extensive field work on a reservoir. Furthermore, $SWT$ for larger reservoirs are directly measured with great difficulty and high uncertainties due to high spatial variation in $SWT$ over short-time scale. Consequently, spatial variability of $SWT$ is often estimated using several satellites with relative accuracy (Steissberg *et al*., 2005). Furthermore, satellites provide synoptic and frequent data acquisition over large areas (Alcântara *et al*., 2011). According to (Chuvieco, 2002, cited by Lamaro *et al*., 2013), satellite information allows to obtain data in digital format that can be easily combined with other geographic information and used to generate quantitative models. The Landsat-8 images are freely distributed through the U.S. Geological Survey and is the one of the satellites that has been used to assess spatial variability of $SWT$ in reservoirs (e.g. Alcântara *et al*., 2010). Sima *et al.* (2013) reported good agreement between Landsat-8 estimates of $SWT$ and the *in-situ* measurements $SWT$. Landsat-8 was officially launched in year 2013 and deployed into orbit with two instruments on-board of which one is the Thermal Infrared Sensor (TIRS) with two spectral bands in the long-wave infrared that can be used to retrieve $SWT$ (Rozenstein *et al*., 2014). The satellite-derived $SWT$ need to be calibrated with long-record of ground truth $SWT$ data which may not be always readily available in the reservoir of interests (Schott *et al*., 2001). Furthermore, the thermal infrared data from the satellite need to be corrected for the emissivity and atmospheric effects for quantitative assessment of $SWT$ (Li *et al*., 2013). The major limitation of using Landsat-8 data to access daily variability of $SWT$ is that this satellite acquire data once in every 16 days at any given location and does not record data at night (Alcântara *et al*., 2011). Furthermore, the spatial resolution of the TIRS data of 100 m limits the application of the Landsat-8 data on assessing

variability of $SWT$ over small irrigation waters storages and open lakes (Rozenstein *et al*., 2014).

## 2.2 Available energy flux for open water evaporation

### *2.2.1 Introduction*

The difference between $R_n$ and $G$ fluxes, is a measure of the available energy flux that drive the processes of open water evaporation in a reservoir (Finch and Calver 2008).

### *2.2.2 Measuring available energy flux*

Federer (1968) argues that if water is unlimited at the evaporative surface, the energy flux used in evaporation (latent energy) may be equal to the $R_n$ which is generally measured by a net radiometer. However, Finch and Gash (2001) stress the significance of considering $G$ in the energy balance techniques and concluded that the accurate measurement or estimation of $G$ is a paramount input parameter for open water evaporation studies. According to Mengistu and Savage (2010), $G$ is determined from water temperature profile measurements using the (Brutsaert, 1982) equation as:

$$G = \rho_w c_w \Delta z \frac{\Delta T_w}{\Delta t} \tag{2.4}$$

where $\rho_w$ is the density of water, $c_w$ is the specific heat capacity of water, $\Delta z$ is the depth increment in water profile, $\Delta T_w$ is the average water temperature difference from one averaging time to another for depth increment and $\Delta t$ is the change in time for the averaging period.

### *2.2.3 Modelling available energy flux*

Geraldo-Ferreira *et al.* (2011) argues that $R_n$ is not strictly a micrometeorological parameter due to its dependency on the temperature, emissivity and reflection of the underlying surface. Furthermore, $R_n$ is measured with difficulty since it is the sum of four distinct variables. Consequently, $R_n$ is measured in only a few number of standard weather stations. According to Dong *et al.* (1992), net radiometers are expensive, requiring continuous calibration and maintenance to ensure accurate estimates of $R_n$. Furthermore, Dong *et al.* (1992) noted that the net radiometers that are placed permanently in the field are subject to damage by ultraviolet radiation, which degrades both the black sensing surfaces and the polyethylene domes. Geraldo-

Ferreira *et al*. (2011) argues that meteorological data measured in standard meteorological stations can be used to model $R_n$ in order to replace the use of the expensive net radiometers. The number of models used to estimate $R_n$ from standard meteorological data varies with the level of complexity and data input requirements (Wang *et al*., 2009). These models require measurements of the solar irradiance, air temperature and water vapour pressure (Blonquist *et al*., 2010). Iziomon *et al*. (2000) stressed that $R_n$ should be determined from models which are universally applicable and relatively easy to utilise.

Brutsaert (1982) showed that $G$ can be indirectly determined from water temperature profile measurements obtained by thermocouples. However, the lack of the temporal and spatial water temperature profile data at water storages hinders routine estimation of $G$ from water temperature profile (Winter *et al*., 2003). Tanny *et al*. (2008) argued that turbulent water waves of different temperatures travelling past the thermocouple could results on significant errors on $G$ estimated from water temperature profile. Consequently, $G$ is often estimated using heat storage models for lakes based on the readily available data at the nearby meteorological weather station and some characteristics of the water storage such as water level and turbidity (Duan, 2014).

The Penman model applied to open water by Penman (1948) was the first equation to combine both energy balance and aerodynamic aspects to estimate daily evaporation (McMahon *et al*., 2013). The energy balance aspect depends on the solar irradiance which provides the energy required to evaporate water while the aerodynamic aspect depends on wind, humidity, and temperature by which energy is removed from the evaporative surface (King *et al*., 2015). According to McMahon *et al*. (2013), this approach eliminates $SWT$ parameter which is not readily available at standard automatic weather stations and difficult to measure due to high wind turbulence at water surface. Monteith (1965) modified the Penman model by including a surface resistance term which resulted on the widely-used Penman- Monteith model. Penman-Monteith model is a physically based equation that has been successfully applied in many different locations worldwide to estimate both open water evaporation and evaporation from different vegetation covers (Finch and Hall, 2001). When the Penman-Monteith model is applied to estimate open water evaporation, it requires land-based inputs of the solar irradiance, sunshine hours or cloudiness, air temperature, relative humidity and wind speed from a nearby

weather station which are used to calculate $R_n$ (McMahon *et al*., 2013). Valiantzas (2006) noted that one of the disadvantages of the Penman-Monteith model is that $R_n$ is usually computed indirectly from the readily available meteorological data measured at the nearby automatic weather stations.

The main limitation of the Penman-Monteith model is the lack of validity of an assumption that the water column is well mixed and there is no change in $G$ (Finch and Gash, 2001). Edinger *et al*. (1968) proposed a useful model based on the concept of an equilibrium temperature and associated time constant, determined from land-based meteorological data to estimate $G$ (Finch, 2001). According to McMahon *et al*. (2013), the equilibrium temperature model has been developed further by Keijman (1974), Fraederich *et al.* (1977), de Bruin (1982) and Finch and Gash (2002). McJannet *et al*. (2008) noted that a modification of the model was since deeper water bodies can store more heat than shallow water bodies. Consequently, they are not in thermal equilibrium and the surface temperature may be greater than or less than the equilibrium temperature. Finch (2001) defined equilibrium temperature as the temperature which the water temperature is being driven to by the net energy flux exchange. For water at the equilibrium temperature, the net rate of energy flux exchange is zero (Finch and Hall, 2001). From this, an expression for the temperature of a well-mixed body of water as a function of time and water depth was derived. The water-body temperature estimated from this expression can then be used to calculate $G$ and $L_u$ from the water surface (Finch and Calver, 2001). McJannet *et al*. (2008) used the concept of equilibrium temperature applied to the Penman-Monteith model to account for $G$. The modified Penman-Monteith model allows adjustment to the amount of the energy available flux for evaporation based on changes in $G$ (McJannet *et al*., 2008).

### *2.2.4 Description of the DPMETHS model for computing available energy flux*

The model description provided by McJannet *et al*. (2008) form the basis of the daily time-step DPMETHS spreadsheet implemented model of Savage *et al.* (2016) that is used in this study to estimate available energy flux. The DPMETHS model computes available energy flux from the daily measurements of $R_s$, maximum and minimum air temperature ($T_{air}$), minimum and maximum relative humidity ($RH$) and wind speed ($U$) acquired at nearby land-based weather station. According to Finch and Hall (2001), $R_s$ reaching the water surface is reduced by $rR_s$ based on the reflection coefficient of water surface ($r$) and net outgoing infrared irradiance.

According to de Bruin (1982), the net infrared irradiance is calculated from $T_{air}$ at 09h00, the estimated daily-average water temperature and cloudiness factor ($C_f$) while $R_n$ at water surface is calculated from:

$$R_{net\ wet} = R_s - rR_s + L_d - L_{u\ wet} \tag{2.5}$$

where $r$ is approximately 0.08 (Finch and Hall, 2001) and $L_d$ is calculated from:

$$L_d = \sigma(T_a + 273.15)^4(C_f + (1 - C_f)(1 - 0.261\exp(-7.77\times10^{-4}T_a^2)) \tag{2.6}$$

where $\sigma = 4.9\times10^{-9}$ MJ m$^{-2}$ K$^{-4}$ is the modified for daily time-scale Stefan-Boltzmann constant. $C_f$ is determined using the procedure presented by Jegede *et al*. (2006):

for $I_s / I_{s\ \mathrm{clear}} \leq 0.9$, where:

$$I_{s\ clear} = I_{s\ extra}(0.75 + 2\times10^{-5}h) \tag{2.7}$$

where $I_{s\ clear}$ is the clear-sky solar irradiance (MJ m$^{-2}$), and where $I_{s\ extra}$ is the extra-terrestrial solar irradiance (MJ m$^{-2}$) and $h$ is the site latitude (m). $I_{s\ extra}$ is calculated using standard astronomical equation involving day of year, latitude, declimination and sunset hour angle, then:

$$C_f = 1.1 - I_s/I_{s\ clear} \tag{2.8}$$

Otherwise if $I_s/I_{s\ clear} > 0.9$ then:

$$C_f = 2(1 - I_s/I_{s\ clear}) \tag{2.9}$$

In Eq. 2.5, $L_{u\ wet}$ is the outgoing infrared irradiance emitted by the water surface at temperature $T_{water}$ (K) and is calculated using:

$$L_{u\ wet} = 0.97\sigma(T_{water} + 273.15)^4 \tag{2.10}$$

$L_{u\ wet}$ (MJ m$^{-2}$) is approximated using Taylor series expansion at $T_a$ by:

$$L_{u\ wet} = 0.97\sigma(T_a + 273.15)^4 + 4\sigma(T_a + 273.15)^3(T_{water\ i-1} - T_a) \tag{2.11}$$

where the factor 0.97 corresponds to the emissivity of water (Anderson 1954, cited by Jensen, 2010) and $T_a$ is the air temperature at reference height (°C).

Within the DPMETHS model, changes to water-body temperature and $G$ are highly susceptible to the equilibrium temperature and a water-body time constant. The time constant is directly affected by the water depth and it governs the rate of change in water temperature between consecutive days as it dictates the time that would be required to reach equilibrium (McJannet *et al*., 2008). The daily-average water temperature on day $i$, $T_{water\ i}$ (°C), is calculated from

the average water temperature of the previous day ($T_{water\ i}$ - 1), a water-body time constant $\tau$ (days) and an equilibrium temperature $T_e$ (°C):

$$T_{water\ i} = T_e + (T_{water\ i-1} - T_e)\ \exp(-t/\tau) \tag{2.12}$$

The $\tau$ is calculated based on the de Bruin (1982) method:

$$\tau = \frac{\rho_w c_w d}{4\sigma(T_{wet} + 273.15)^3 + f(U)(\Delta_{Twet} + \gamma)} \tag{2.13}$$

where $\rho_w$ is density of water (kg m$^{-3}$), $c_w$ is the specific heat capacity of water (0.004185 MJ kg$^{-1}$ K$^{-1}$), and $d$ is the water depth (m), $T_{wet}$ is the wet bulb temperature, γ is the psychrometric constant, $\Delta_{Twet}$ (kPa °C$^{-1}$) is the slope of the temperature saturation water vapour vs temperature relationship curve at the wet bulb temperature and $f(U)$ is the wind functions that are usually derived empirically for particular location. The $f(U)$ above water is computed using the Harbeck (1962) method:

$$f(U_2) = 7.127A^{-0.05}U_2 \tag{2.14}$$

where $f(U_2)$ is the wind function for wind speed measured at a height of 2 m above the surface (MJ m$^{-2}$ kPa$^{-1}$) and *A* is the surface area of the water storage (m$^2$).

The equilibrium temperature, $T_e$ (°C), is calculated based on equation of de Bruin (1982):

$$T_e = T_{wet} + \frac{R_{net\ wet}}{4\sigma(T_{wet} + 273.15)^3 + f(u)(\Delta_{wet} + \gamma)} \tag{2.15}$$

The one-day change in heat energy flux storage of water, *S* (MJ m$^{-2}$) between day *i* and *i* - 1 is given by:

$$S = \rho_w c_w d\ (T_{water\ i} - T_{water\ i-1}) \tag{2.16}$$

# CHAPTER 3 : METHODS AND MATERIALS

## 3.1 Study site description

The study was conducted at Midmar Dam at Umgeni Catchment in KwaZulu-Natal Midlands at about 3 km south-west of town Howick outside Pietermaritzburg, South Africa (29º 30'S, 30º10'E, elevation 985 m) from 7th July 2015 to 4th April 2016 (Figure 3.1). Some of the characteristics of the Midmar Dam are described in Table 3.1.

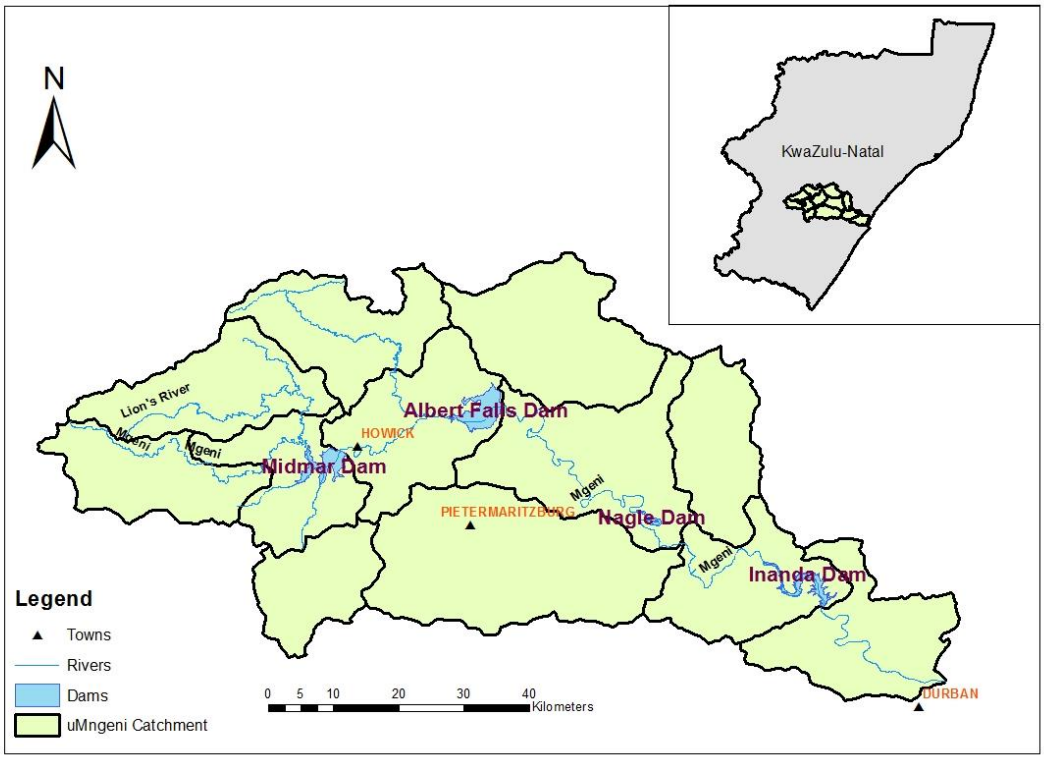


**Figure 3.1: Map showing the location of the Midmar Dam in the Umgeni catchment in KwaZulu-Natal midlands.**

The primary purpose of the dam is for municipal and industrial water use (Department of Water Affairs and Forestry, 2007). According to Simpson and Dickens (2006), Midmar Dam supplies approximately 374 million kilolitres of water to about 4.8 million people each year in the Howick, Pietermaritzburg and Durban regions. Midmar Dam is the first of a cascade of four large dams on the Umgeni River system (Figure 3.1). Outflow from Midmar Dam feeds Albert Falls Dam which subsequently feeds Nagle and Inanda Dams downstream (Simpson and Dickens, 2006). Consequently, the three large reservoirs in the Umgeni River system are directly affected by the quality and quantity of the outflow from Midmar Dam. According to Mengistu and Savage (2010), this area receives summer rainfall and the summer season is

characterized by warm and wet days with $T_{air}$ exceeding 30 $^{o}$C in summer while the winter season is characterized by cold and dry days with $T_{air}$ below 20 $^{o}$C and during night-time it may decrease to below 0 $^{o}$C.

**Table 3.1: Some characteristics of Midmar Dam (adapted from Mengistu and Savage (2010)).**

| Characteristic | Description |
|---|---|
| Location | 29$^{o}$ 30'S, 30$^{o}$10'E |
| Elevation | 985 m |
| Mean maximum $T_{air}$ | 30 $^{o}$C |
| Mean minimum $T_{air}$ | 20 $^{o}$C |
| Mean annual precipitation | 992 mm |
| Maximum daily evaporation | 3.9 mm |
| $A$ | 1793.15 ha |
| Total capacity | 235.5 Million m$^3$ |

### 3.2 Experimental setup

Land-based and water-based stations were used during the study. At the land-based station, measurements of $R_s$, $T_{air}$, $RH$, rainfall, $U$ and wind direction were monitored. At the water-based station, measurements of the components of the $R_n$ flux were monitored using a four-component net radiometer mounted at 1.5 m above the water surface. The measurements of the air temperature and relative humidity were also acquired at 1.5 m above water. The surface water temperatures were monitored using a pair of infrared thermometers with a field of view 22.0$^{o}$, mounted at 1.5 m above the water surface. Furthermore, water temperatures at different depths of water were also monitored using Type-E thermocouples.

### 3.3 Instrumentation

The components of $R_n$ are generally measured by net radiometers. There are different models of net radiometers available at the market. The comprehensive study of different net radiometers by Blonquist *et al.* (2009) revealed that accuracy of the estimates of $R_n$ increases with the cost of the net radiometer and the four-component CNR4 net radiometer (Kipp & Zonen, Delft, Netherlands) was one of the most accurate net radiometers. Therefore, in this study a four-

component CNR4 net radiometer which was the most recent model of the radiometer with the most improved features was used. According to Kipp and Zonen (2014), the four-component CNR4 net radiometer consists of a pair of pyranometers and pyrgeometers, with one pair facing upward and the other pair facing downward. The pyranometer measures the solar irradiance while the pyrgeometer measures the infrared irradiance. The four-component CNR4 net radiometer covers the total spectral range between 0.3 and 42 μm, which covers both the solar radiation and the infrared radiation while the gap between these two produces negligible errors (Kipp and Zonen, 2014). The details of all equipment used in station systems are provided in Table 3.2.

**Table 3.2: Details of the equipment used for land-based and water-based weather station systems at Midmar Dam during the study period.**

| **Stations** | **Land-based** | **Water-based** |
|---|---|---|
| Sensors | Solar irradiance (CM3[1]), relative humidity and air temperature (HC2S3[2]), wind speed and direction (03002-L[3]) all at 2 m and rain gauge (TR-525I[4]) at 1.2 m | Net radiometer (CNR4[5]), relative humidity and air temperature (HC2S3[2]), two IRT (SI-111[6]) all at 1.5 m above water and five Type-E thermocouples at different water depths i.e. 20, 40, 80, 120, 160 mm water |
| Field Data loggers | CR1000[7]. All measurements were every 5 s and averaged/totalled every 2 min, 60 min and daily time steps outputs | CR3000[8]. All measurements were every 5 s and averaged every 30 min time step outputs |
| Power details | Connected to two 12 A h battery | Connected to a 12 A h battery |
| Data storage method | Stored in datalogger memory and SD card | Stored in SD card |
| Software | The station software included Loggernet 4.2[8] for scheduled connection to data logger and download of data | The station software included Loggernet 4.2[8] for scheduled connection to data logger and download of data |

| | | |
|---|---|---|
| Data collection method | data were downloaded from the data logger and SD card using laptop | data were downloaded from the data logger and SD card using laptop |

[1]Pynarometer, Kipp & Zonen, Delft, Netherlands; [2]RH and T probe, Campbell Scientific Inc., Logan, Utah, USA; [3]RM Young wind sentry, Campbell; [4]rain gauge, Texas Electronics, Inc, Shilling Way, Dallas, USA; [5]net radiometer, Kipp & Zonen; [6]infrared thermometers, Apogee Instruments Inc., Logan, USA; [7]CR1000, Campbell; [8]CR3000, Campbell; [9]Loggernet, Campbell

### 3.4 Equipment testing and calibration

Before setting equipment at the experiment sites, laboratory test and calibration of equipment were done.

#### *3.4.1 Laboratory equipment test*

Laboratory tests were conducted to evaluate the performance and functioning of the different sensors used as well as to validate the created datalogger programs before deploying the equipment to the study sites. The main aim of these tests was to detect and replace any faulty sensor as well as to evaluate the correctness of the created datalogger programs.

3.4.1.1 Testing the land-based station sensors

The sensors for measuring $R_s$, $T_{air}$, $RH$, rainfall, $U$ and wind direction as well as a rain gauge were connected to the CR1000 datalogger and monitored over a period. To test the air temperature and relative humidity sensor, a humid atmosphere was artificially created around the sensor by blowing on the sensor. Measurements of the air temperature and relative humidity were viewed through PC200W program (Campbell Scientific Inc.) which allowed observation of data at 5 s scan intervals. After blowing on the sensor, relative humidity readings rose as high as 95 % indicating that the sensor was working correctly. Temperature readings of the sensor averaged at 24 ºC which was equal to the room temperature of the day, and partly indicated the correct functioning of the air temperature and relative humidity sensor. The greater measurements of the solar irradiance were observed when the light from the torch was directed to the sensor while solar irradiances were approximately zero when the sensor was shaded. These observations indicated the correct functioning of the pyranometer. The wind sentry was tested by blowing on the sensor with a fan. The greater wind speed measurements

were observed during the blowing on the sensor compared to sensor not blow on. These observations indicated the reasonable functioning of the wind sentry. The rain gauge was tested using a volume calibration. Measured amount of water were poured into the receiving area of the rain gauge using a syringe. The volume of water added was recorded each time the gauge tips. The manufacturer claims that the rain gauge tips after every 0.25 mm of water. The number of tips were in reasonable agreement with the volume of water added, which indicated the correct functioning of the rain gauge.

3.4.1.2 Testing the water-based station sensors

The procedure used to test the four-component CNR4 net radiometer at the laboratory was adapted from the procedure provided by Savage and Heilman (2009) based on the recommendations of Kipp and Zonen (2014). The four-component CNR4 net radiometer sensor was connected to the CR3000 datalogger and the components of $R_n$ were monitored over a period. The test was conducted by directing the torch at the net radiometer sensors. The torch was shone on 'up-facing' and 'down-facing' sensors at different times, respectively. The data collected was viewed through PC200W program which allowed the observation of data at 5 s scan intervals. The observations showed a difference of less than 10 % after comparing the 'up-facing' pyranometer and the 'down-facing' one and the same was also noted for the pyrgeometer. The multimeter test using an alternating voltage was also conducted to further evaluate the functioning of the pyranometers and pyrgeometers in the net radiometer. When the pyranometers were shaded with hands, the solar irradiance readings were approximately zero. However, when the pyranometers were exposed to light, the positive readings of the solar irradiances were observed. The fluxes of the net short-wave solar irradiance which is the difference between incoming solar irradiance and the reflected solar irradiance were always positive. The values of the reflection coefficient which is the ratio of the incoming solar irradiance and the reflected solar irradiance were found to range between 0 and 1. These observations indicated the correct functioning of the pyranometers. When hot objects were placed in front of the pyrgeometers, the thermal radiation caused pyrgeometers to generate positive voltages since the surface temperature of the hot object was greater than the pyrgeometers temperatures. When the pyrgeometers were shone at the wall of the room, the thermal radiation caused pyrgeometers to generate negative voltages since the surface temperature of the wall was cooler than the pyrgeometers temperatures. These observations indicated the correct functioning of the pyrgeometers. The air temperature and relative humidity

sensor at water-based station was tested using the same procedure as the air temperature and relative humidity sensor for the land-based station. The comparisons between the measurements of the air temperature and relative humidity measured at water-based and land-based showed a difference of less than 5 %. These observations indicated the correct functioning of both air temperature and relative humidity sensors. The infrared thermometers were tested using the procedure of Savage and Heilman (2009).

### *3.4.2 Calibration of the station systems*

Both systems were also setup at the Agrometeorology Instrument Mast system (AIM system) of Savage *et al.* (2014), for seven months (March to October of year 2015) to test the functioning of both instrumentation and datalogger programs in the outdoor as well as to calibrate the systems against the known standard AIM system before the systems. The AIM system is located (29.628 °S, 30.403 °E, at elevation of 671.3 m) near the Rabie Saunders Building of the University of KwaZulu-Natal, Pietermaritzburg, South Africa. The data acquired from both land-based and water-based station systems were compared against the data from the AIM system for the same period.

## 3.5 Systems set-up

After the calibration, land-based and water-based station systems were installed at Midmar Dam (Figure 3.2). The land-based station was installed near the dam at 100 m away from the shore on the 7$^{th}$ July 2015 while the water-based station was installed above water at 30 m away from the shore on the 12$^{th}$ February 2016 (Figure 3.3). The systems collected data between 12$^{th}$ February and 4$^{th}$ April 2016 for the current study apart from when there were power or data collection problems.


**Figure 3.2: Location of the land and water-based stations at Midmar Dam during the study period.**

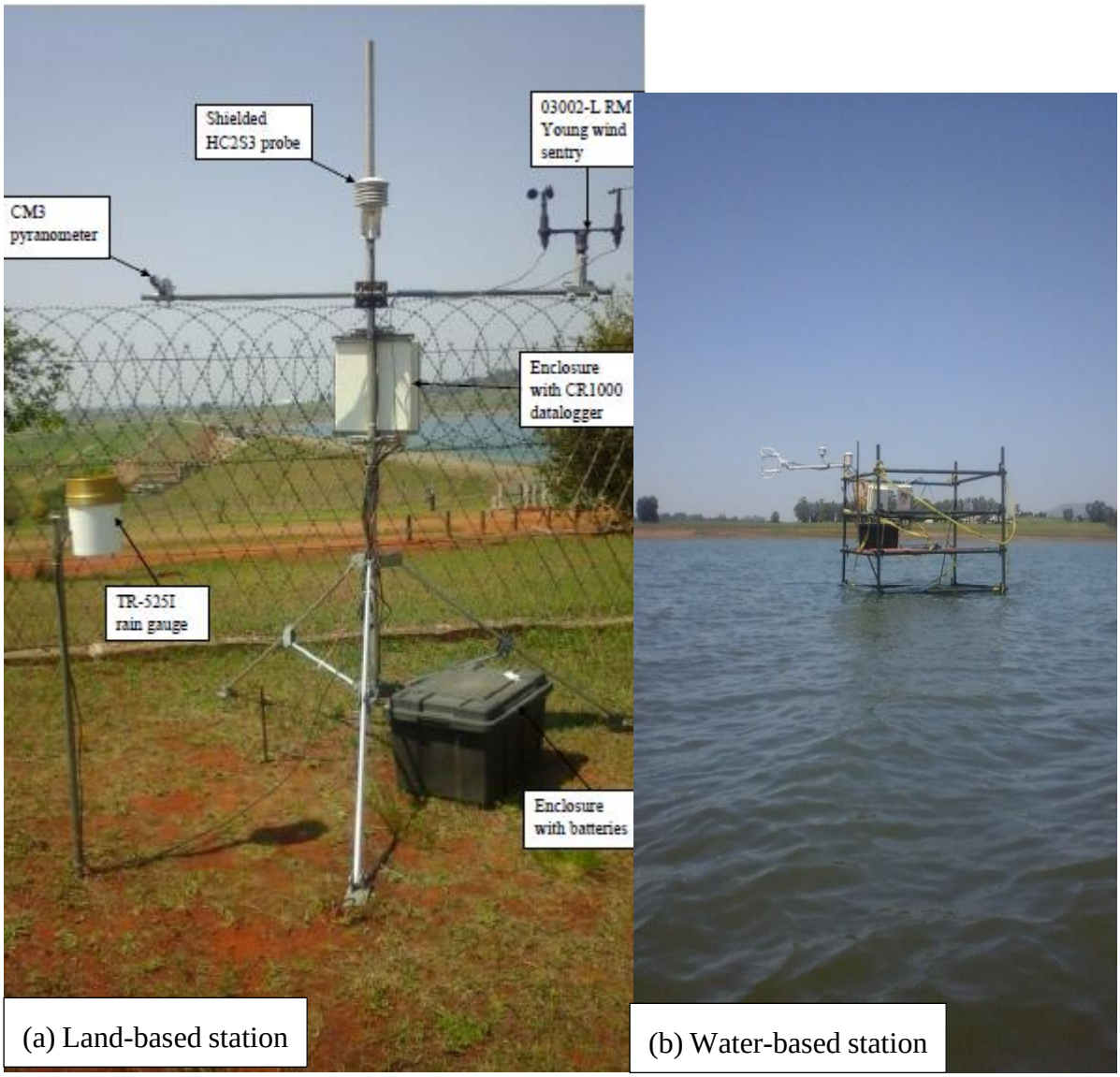


**Figure 3.3: Land and water-based stations at Midmar Dam during the study period.**

### 3.6 Data collection and processing

The meteorological data from both land-based and water-based stations were downloaded from the dataloggers after every few weeks and imported into a spreadsheet. The downloaded data underwent data quality control-routine to identify missing data, errors, possible error corrections and suspect data as well as to ensure that data were consistent and met the data quality objectives. Furthermore, data quality control was important not only in obtaining accurate data but also for monitoring the operation of the observing system. When an abnormal observation was reported, the cause was identified and any maintenance, calibration of both faulty sensor and datalogger program were carried out. Only land and water data that passed the quality control tests were used for data analysis. The measured water-based data at

timestamp of 30-min were averaged to match the daily resolution of the radiative fluxes estimated using the daily DPMETHS model. To obtain complete data sets for modelling purposes, the missing, faulty and suspect data on the land-based weather station at Midmar Dam were filled by the observations available from the nearby weather stations monitored by Agricultural Research Council (Cedara and Everdon). The location of the different stations where data used in this study were obtained is described in Table 3.3. Furthermore, the daily water depth and surface area data of Midmar Dam which are input to the DPMETHS model were acquired from Umgeni Water.

**Table 3.3: Location of the different stations used in the study**

| Station name | Latitude (S) | Longitude (E) | Elevation (m) |
|---|---|---|---|
| Land-based | 29°29'35.76" | 30°11'52.80" | 1045 |
| Water-based | 29°30'53.66" | 30°10'50.72" | 1045 |
| Everdon | 29°27'19.90" | 30°16'25.80" | 1077 |
| Cedara | 29°32'30.80" | 30°15'53.90" | 1068 |

### 3.7 Data analysis

Both land-based and water-based measured meteorological data from 24 February to 4 April 2016 i.e. day of year (DOY) 54 to 94 were used for analysis and modelling purposes at Midmar Dam. Good quality meteorological daily data obtained from the land-based station as well as the surface area and water depth of the dam data were used as input to the DPMETHS model to estimate daily $R_n$ and $G$. Model estimates of $R_n$ and $G$ were compared to the measurements of $R_n$ and $G$ for the above water surface. The model simulations were compared against the measured estimates by using simple linear regression and other statistics given Page *et al.* (1979). For the error analysis, the following statistics were used:

$$RMSE = \sqrt{\frac{\sum_{i=1}^{n}(R_{ne} - R_n)^2}{n}} \tag{3.1}$$

$$MBE = \frac{\sum_{i=1}^{n}(R_{ne} - R_n)}{n} \tag{3.2}$$

where $RMSE$ and $MBE$ are the root mean square error, and mean bias error, respectively. $R_{ne}$ is the modelled net irradiance, $R_n$ is the measured net irradiance, $n$ is the number of observations.

A term by term comparison of the actual difference between $R_{ne}$ and $R_n$ for the short-term performance of the DPMETHS model was conducted using $RMSE$ while for long-term performance, $MBE$ was used. To justify whether the difference between $R_{ne}$ and $R_n$ was significant or not, the student t-test was used. Walpole and Myers (1989) showed that t-value can be calculated from the $RMSE$ and $MBE$ errors, as:

$$t = \sqrt{\frac{(n-1)MBE^2}{RMSE^2 - MBE^2}} \tag{3.3}$$

### 3.8 Landsat-8 surface water temperatures data collection and processing

Images acquired during the study period were downloaded from the website of the United States Geological Survey (USGS) (http://glovis.usgs.gov/). Two Landsat-8 images covering Midmar Dam were collected during the study period (i.e. acquired on the 25th February and 12th March). However, only the image acquired on the 25th February had cloud cover less than 60% and was used in this study. At-sensor thermal infrared sensor (TIRS) provides data measured at a wavelength region are generally stored in Digital Numbers (DNs) at spatial resolution of 100 m. The TIRS provide two thermal bands (band 10 and 11). However, only thermal band 10 was used to compute $SWT$ in this study. The choice of this band was based on its greater range of wavelength and it's not being saturated as also noted by Lamaro *et al.* (2013). The Ilwis 3.8 free software was used to write script which was used to convert TIRS data into surface water temperatures. The script used utilized the following procedure as recommended by the USG (2013):

The radiance rescaling factors provided in the metadata file were used convert the DN values to TOA spectral radiance using:

$$L_{\boldsymbol{\lambda}} = M_{\mathbf{L}} Q_{\mathbf{cal}} + A_{\mathbf{L}} \tag{3.4}$$

where $L_{\boldsymbol{\lambda}}$ is the TOA spectral radiance (Watts/ ($m^2$ srad μm)), $M_{\mathbf{L}}$ is the Band-specific multiplicative rescaling factor from the metadata (RADIANCE_MULT_BAND_x, where x is

the band number), $Q_{\mathbf{cal}}$ is the quantized and calibrated standard product pixel values (DN), $A_{\mathbf{L}}$ is the band-specific additive rescaling factor from the metadata (RADIANCE_ADD_BAND_x).

The TOA spectral radiances were then converted to brightness temperatures using the thermal constants provided in the metadata file:

$$T = \frac{K_2}{\ln(\left(\frac{K_1}{L_\lambda} + 1\right)} \tag{3.5}$$

where $T$ is the at-satellite brightness temperature (K), $K_1$ is the Band-specific thermal conversion constant from the metadata (K1_CONSTANT_BAND_x) and $K_2$ is the Band-specific thermal conversion constant from the metadata (K2_CONSTANT_BAND_x).

The at-satellite brightness temperatures were used to compute surface water temperatures using:

$$SWT = \frac{T}{(1 + w) \times \left(\frac{T}{p}\right) \times \ln(\varepsilon)} \tag{3.6}$$

where $SWT$ is surface water temperature (K), $w$ is the RADIANCE_MULT_BAND at 11.5 µm, $p$ is the Plack's constant ($6.626 \times 10^{-34}$ J s) and $\varepsilon$ is 0.97 corresponds to the infrared emissivity of water.

Water-surface temperature values estimated for the image were extracted by interpolating the location of the sampling sites using ArcGIS 10.3 software. Finally, temperatures in Kelvin were converted into $^{o}$C by subtracting 273.15 from the Kelvin using a raster calculator in ArcGIS.

### 3.9 Acquisition of the ocean data

The hourly solar irradiance, incoming infrared irradiance, air temperature, sea surface temperature, relative humidity, wind speed and direction, rain fall and barometric pressure data of the ocean were acquired from Station 32ST0 (Stratus), owned and maintained by Woods Hole Oceanographic Institution (http://www.ndbc.noaa.gov/station_page.php?station=32ST0). The detailed information about the Stratus station and the measurement descriptions can be found at: http://www.ndbc.noaa.gov/measdes.shtml. The data acquired between 10$^{th}$ September and 24$^{th}$ October 2016 were used for the modelling purposes and the choice of these data was based on long record of quality data available from the ocean station.

### 3.10 Acquisition of the long-term historical data at Cedara station

The daily $R_s$, $T_{air}$, $RH$, $U$ and sunshine duration as well as rainfall data were acquired from Cedara station, owned and maintained by Agricultural Research Council. The meteorological data from 1 January 1966 to 31 December 2015 (50 years) were used to investigates the potential impacts of climate change on the radiation balance of Midmar Dam. The choice of these data was based on long-term records of data available at the nearest weather station at Midmar Dam. The missing data were patched using the procedure provided by Savage *et al.* (2016). Furthermore, the history daily water depth and surface area data of Midmar Dam which are input to the DPMETHS model were acquired from Department of Water and Sanitation.

# CHAPTER 4 : RESULTS AND DISCUSSION

## 4.1 Introduction

This Chapter contains results and discussion of results as listed in the aims and objectives section (Section 1.3 and 1.4, respectively). The results of the calibration of the four-component CNR4 net radiometer at the AIM system of Savage *et al* (2014) are discussed at Section 4.2. The discussion in Section 4.2, is on the comparisons between the radiation balance components from the four-component net radiometers (i.e. CNR4 and CNR1) at the AIM system. The climatic conditions overview during the data collection at Midmar Dam is discussed in Section 4.3. The results and findings for the radiation balance of the open water surface at Midmar Dam are discussed in Section 4.4. The discussion in Section 4.4.1, is on the factors that control the temporal variability of the radiation balance of the open water surface. The discussion in Section 4.4.1.1 is on the impacts of clouds cover on the radiation balance of the open water. The discussion in Section 4.4.1.2, is on the temporal variability of reflection coefficient of water ($r$) and its role on the radiation balance of the open water. Section 4.4.1.3, discusses the temporal variability of air temperature ($T_{air}$) and surface water temperature ($SWT$) and their effects on the radiation balance of open water surface. The discussion in Section 4.4.2, is on the impacts of the spatial variability of $SWT$ on the spatial variability of the radiation balance of open water surface at Midmar Dam. The results and findings for the temporal variability of the above-water available energy flux are discussed in Section 4.5. The discussion in Section 4.6, is on the modelling of the radiative fluxes above water at Midmar Dam using a daily time-step DPMETHS model that utilizes the land-based measurements as model inputs. The results and findings for the comparisons between meteorological measurements made over water and land-based measurements are discussed in Section 4.6.1. The discussion in Section 4.6.2, is on the comparisons between the measured and the modelled daily radiative fluxes above water at Midmar Dam. The discussion in Section 4.7, is on the modelling of the radiative fluxes for an eastern Pacific Ocean at different climatic conditions using a daily time-step DPMETHS model. The discussion in Section 4.8, is on the potential impacts of climate change on the radiation balance of Midmar Dam using the long-term radiative daily data generated using the Cedara data as an inputs to the DPMETHS model.

## 4.2 Calibration of the CNR4 net radiometer

As part of the four-component CNR4 net radiometer calibration, radiative fluxes acquired from the water-based station at the AIM system were compared against the radiative fluxes from the four-component CNR1 net radiometer also at the AIM system for the same period. Radiation data between 27th and 29th July 2015 i.e. day of year (DOY) 207 to 209 were used for comparison and the choice of these data sets was based on quality of data available from both four-component net radiometers under clear-sky conditions (Kipp and Zonen, 2014).

### *4.2.1 Solar irradiance*

The comparisons between the solar irradiances $R_{s\_CNR4}$ and $R_{s\_CNR1}$ indicated a good agreement with both following the same diurnal variability, positive during daytime and zero during night-time (Figure 4.1). The regression graph of $R_{s\_CNR4}$ and $R_{s\_CNR1}$ indicated that about 99 % variation in $R_{s\_CNR4}$ can be explained by the $R_{s\_CNR1}$ (Figure 4.2). The observed strong linear relationship between these data sets indicated the correct functioning of the 'up facing' pyranometer in the four-component CNR4 net radiometer.

### *4.2.2 Reflected solar irradiance*

The comparisons between the reflected solar irradiances $rR_{s\_CNR4}$ and $rR_{s\_CNR1}$ indicated a good agreement with both closely following the same diurnal variability, positive during daytime and zero during night-time (Figure 4.3). The regression graph of $rR_{s\_CNR4}$ and $rR_{s\_CNR1}$ indicated that about 99 % variation in $rR_{s\_CNR4}$ can be explained by the $rR_{s\_CNR1}$ (Figure 4.4). The observed strong linear relationship between these data sets indicated the correct functioning of the 'down facing' pyranometer of the four-component CNR4 net radiometer.

### *4.2.3 Incoming infrared irradiance*

The comparisons between the incoming infrared irradiances $L_{d\_CNR4}$ and $L_{d\_CNR1}$ indicated reasonable agreement with both following the same diurnal variability although the peaks of $L_{d\_CNR1}$ were greater than $L_{d\_CNR4}$ (Figure 4.5). However, these observations indicated the correct functioning of the 'up facing' pyrgeometer of the four-component CNR4 net radiometer.

### *4.2.4 Outgoing infrared irradiance*

The comparisons between the outgoing infrared irradiances $L_{u\_CNR4}$ and $L_{u\_CNR1}$ indicated a reasonable agreement with both following the same diurnal variability although the fluxes of $L_{u\_CNR1}$ were greater than fluxes of $L_{u\_CNR4}$ (Figure 4.6). However, these observations indicated the correct functioning of the 'down facing' pyrgeometer of the four-component CNR4 net radiometer.

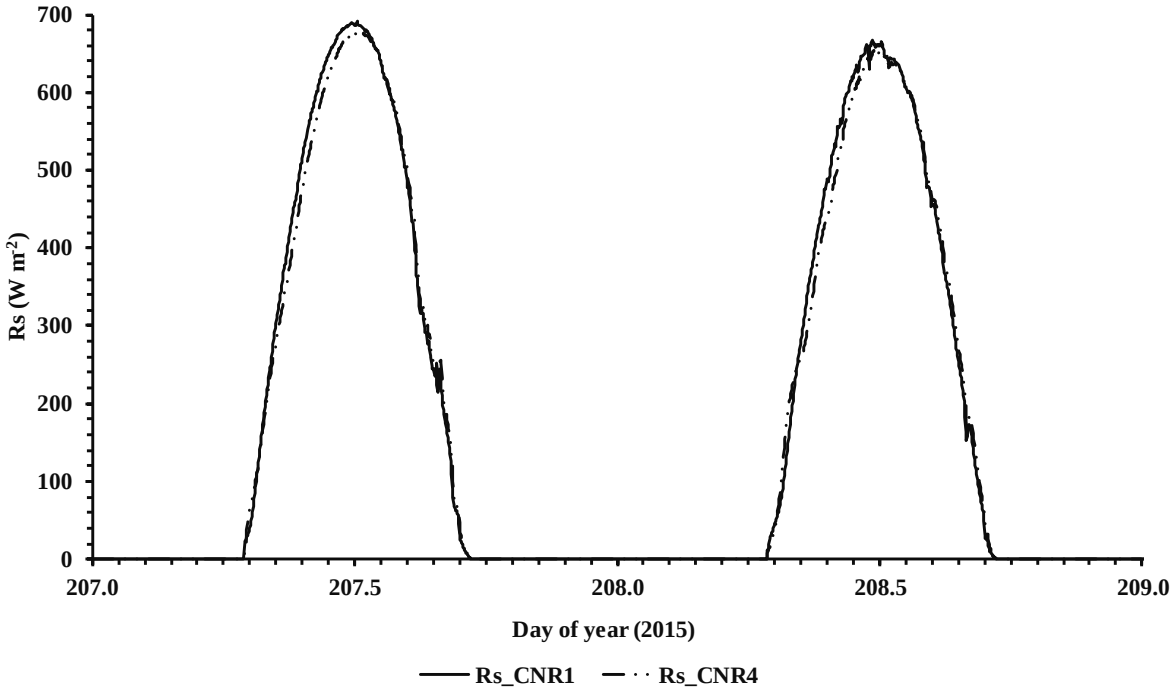


**Figure 4.1: Comparisons between $R_{s\_CNR4}$ and $R_{s\_CNR1}$ for a two-day period (27th and 29th July 2015) at the AIM site.**

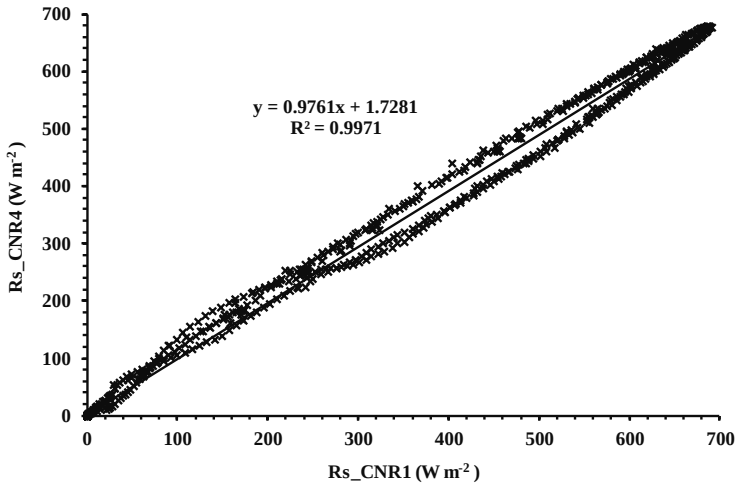


**Figure 4.2: Regression plot of $R_{s\_CNR4}$ vs $R_{s\_CNR1}$ for a two-day period (27th and 29th July 2015) at the AIM site.**

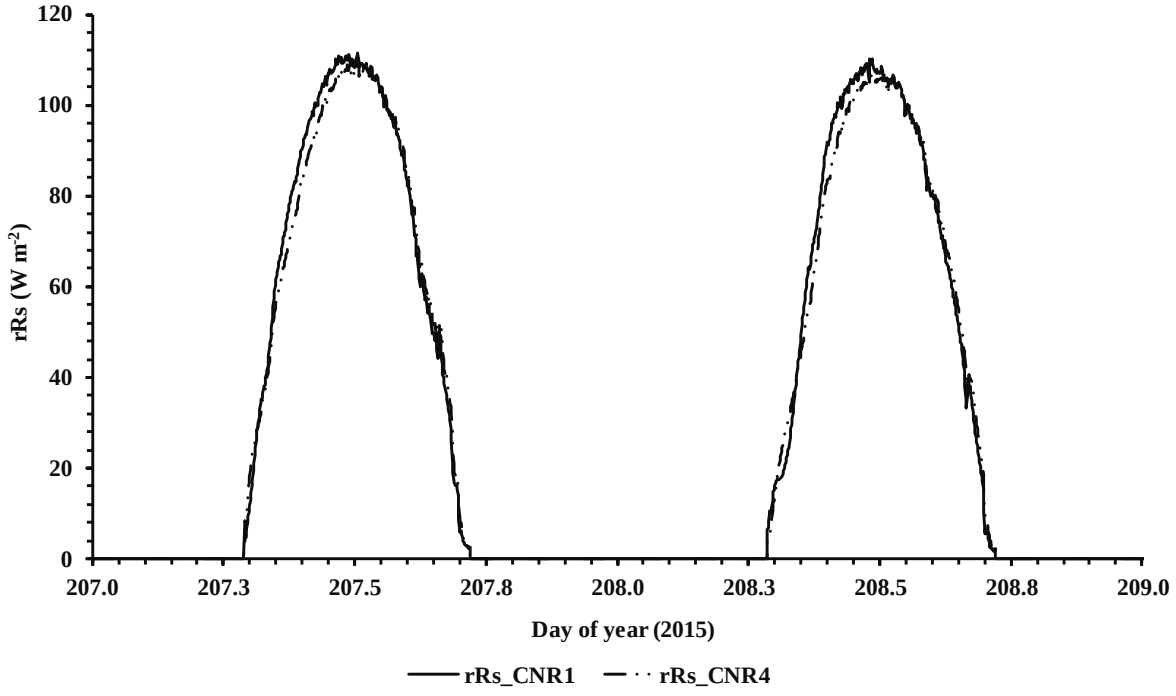


**Figure 4.3: Comparisons between $rR_{s\_CNR4}$ and $rR_{s\_CNR1}$ for a two-day period (27th and 29th July 2015) at the AIM site.**

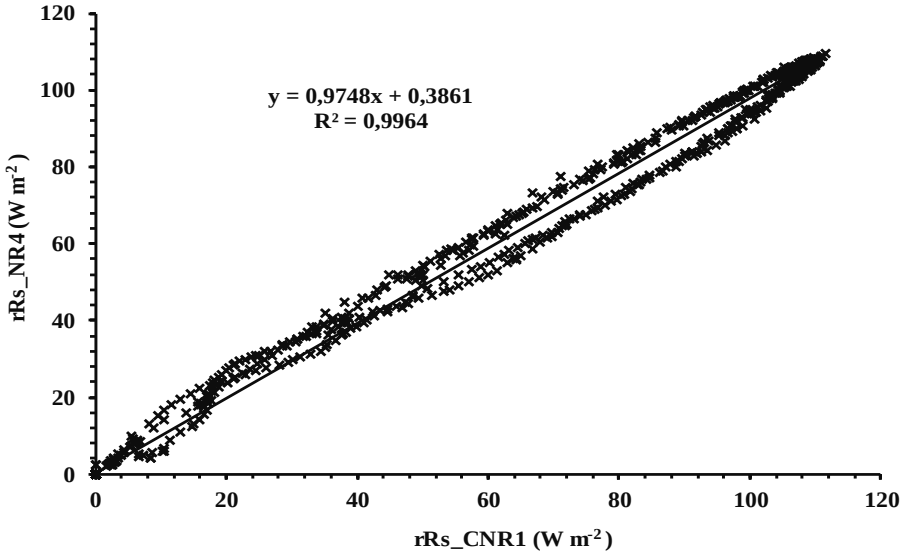


**Figure 4.4: Regression plot of $rR_{s\_CNR4}$ vs $rR_{s\_CNR1}$ for a two-day period (27th and 29th July 2015) at the AIM site.**

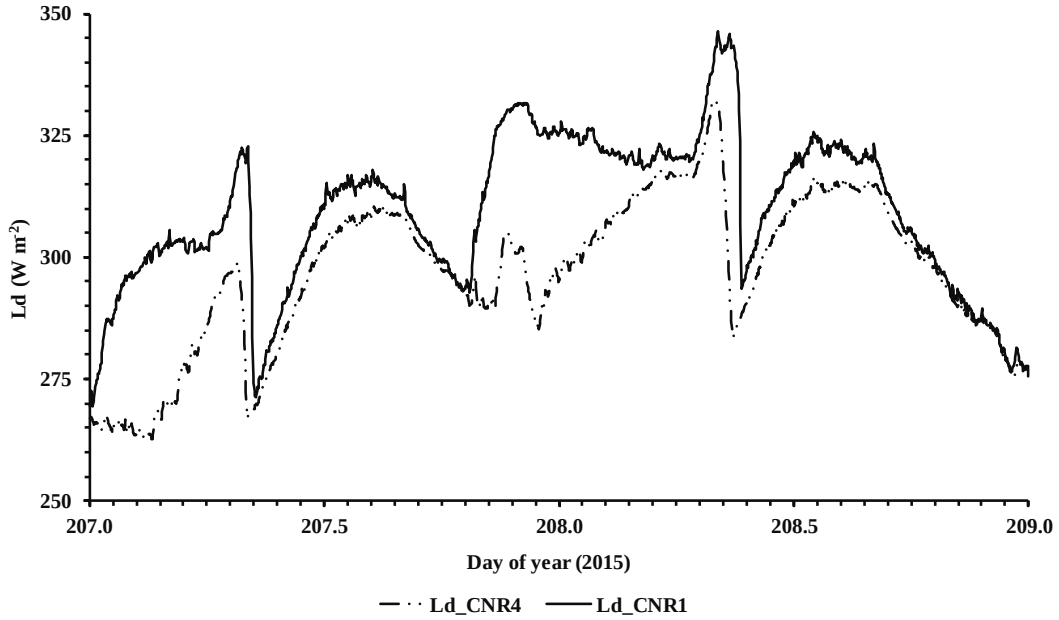


**Figure 4.5: Comparisons between $L_{d\_CNR4}$ and $L_{d\_CNR1}$ for a two-day period (27th and 29th July 2015) at the AIM site.**

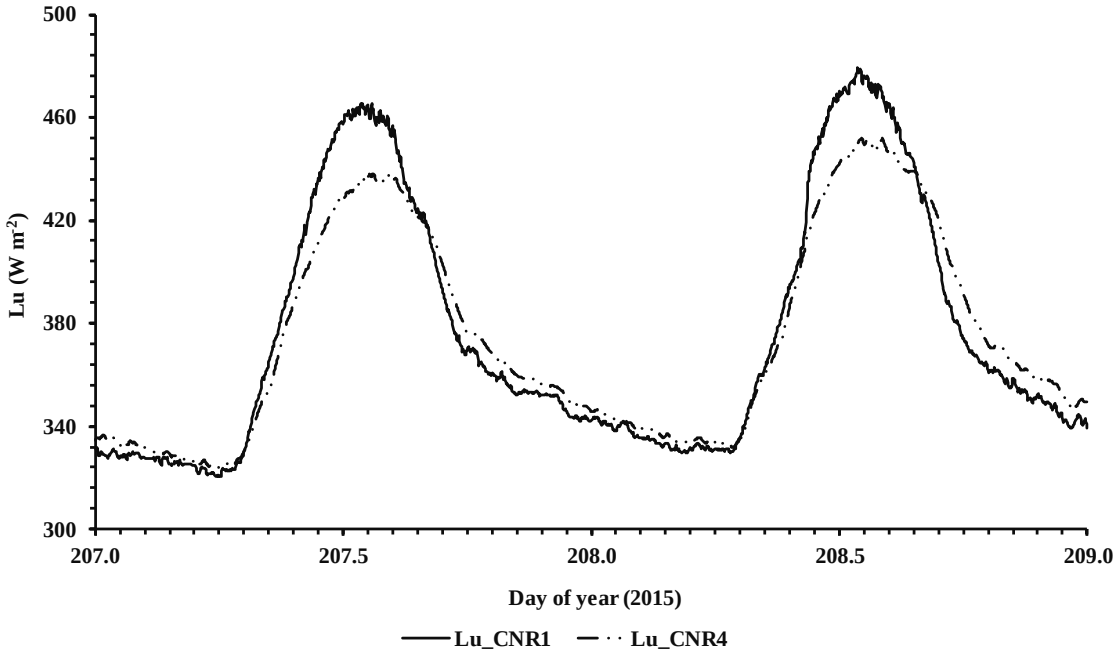


**Figure 4.6: Comparisons between $L_{u\_CNR4}$ and $L_{u\_CNR1}$ for a two-day period (27th and 29th July 2015) at the AIM site.**

### *4.2.5 Net irradiance*

The two-day comparison period between $R_n$ data obtained from the four-component CNR4 net radiometer ($R_{n\_CNR4}$) and $R_n$ data obtained from the four-component CNR1 net radiometer ($R_{n\_CNR1}$) indicated that $R_{n\_CNR4}$ and $R_{n\_CNR1}$ followed the same diurnal variability, $R_n$ being positive during daytime and negative during night-time (Figure 4.7). However, $R_{n\_CNR1}$ was greater than $R_{n\_CNR4}$ during night-time. The regression graph of $R_{n\_CNR4}$ and $R_{n\_CNR1}$ indicated that about 99 % variation in $R_{n\_CNR4}$ can be explained by the $R_{n\_CNR1}$ (Figure 4.8). The observed strong linear relationship between these data sets indicated the correct functioning of the data logger program used to compute $R_n$ from the measured radiation balance components using four-component CNR4 net radiometer.

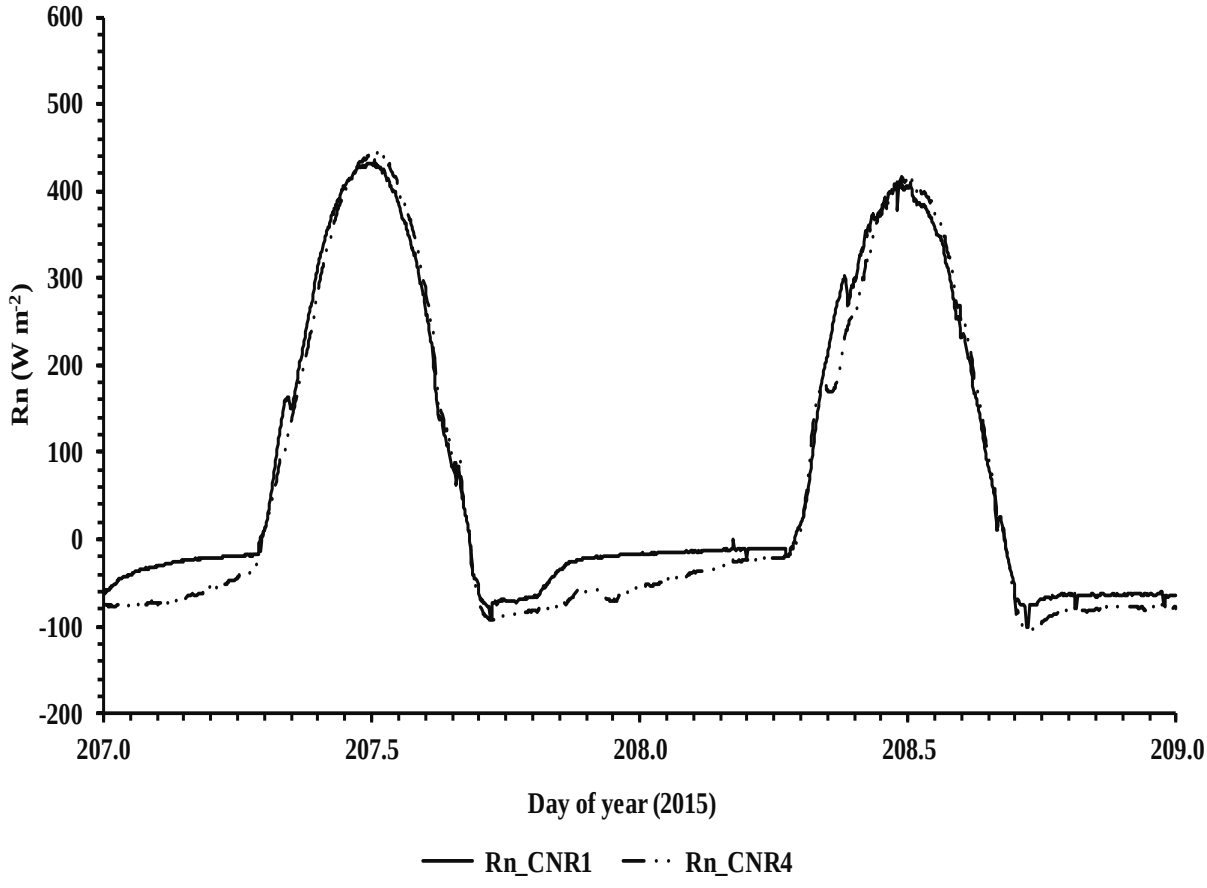


**Figure 4.7: Comparisons between $R_{n\_CNR4}$ and $R_{n\_CNR1}$ for a two-day period (27th and 29th July 2015) at the AIM site.**

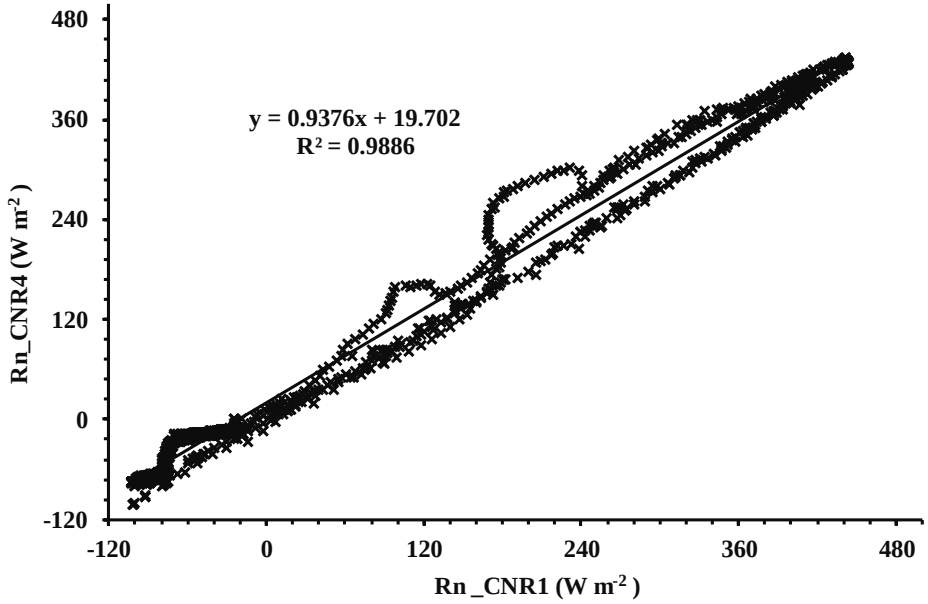


**Figure 4.8: The regression plot of $R_{n\_CNR4}$ vs $R_{n\_CNR1}$ for a two-day period (27th and 29th July 2015) at the AIM site.**

### *4.2.6 General comments*

There were differences between radiation balance components from the four-component net radiometers due to the difference in levelling of these four-component net radiometers since the CNR4 net radiometer was mounted at 1.5 m above the surface while the CNR1 net radiometer was mounted at 3 m above the surface. However, good relationships were observed between these data sets which indicated that the components of the CNR4 net radiometer were functioning properly.

## 4.3 Climatic conditions during study period at Midmar Dam

The land-based microclimate measurements reported were acquired at Midmar Dam between from 24 February to 4 April 2016 i.e. DOY 54 to 94, inclusively. Daily-average $T_{air}$ ranged between 14.5 and 24.9 °C on DOY 82 and 66, respectively. Minimum $T_{air}$ recorded were as low as 10.3 °C (DOY 88) with maxima as high as 34.8 °C (DOY 67) illustrated the wide range of temperature conditions experienced during the measurement period. A rainfall total of 108.6 mm was measured over the entire measurement period (DOY 54 - 94). Daily $R_s$ recorded were as low as 2.18 MJ m$^{-2}$ (DOY 67) with maxima as high as 26.76 MJ m$^{-2}$ (DOY 60) illustrated

the wide range of $R_s$ experienced during the measurement period. Minimum $RH$ as low as 13.1 % (DOY 90) with maxima as high as 100 % (on most of the days) illustrated the wide range of humidity conditions experienced during the experiment. Daily-average $U$ were generally low and ranged between 0.26 and 1.71 m $s^{-1}$, but maximum $U$ as high as 10.70 m $s^{-1}$ (DOY 57) were recorded. Prevailing winds were from the southeast, east and south which correspond to water to land wind flows at the water-based station as also noted by Mengistu and savage (2010).

## 4.4 Radiation balance of the water surface at Midmar Dam

Radiation balance of water is the balance between the net solar radiation and net infrared radiation at water surface. Measurements or estimates of $R_n$ are required for accurate modelling of open water evaporation. However, $R_n$ over water is measured with difficulty since it is the sum of four distinct variables. Furthermore, $R_n$ is measured by net radiometers which are expensive, requiring continuous calibration and maintenance to ensure accurate estimates of $R_n$. Consequently, $R_n$ is often estimated using the models that utilize meteorological data that are readily available in most standard weather stations. However, for accurate modelling of $R_n$ over water surface, it is vital to understand the factors enhancing temporal and spatial variability of the radiation balance of water storage.

### *4.4.1 Factors enhancing temporal variability of the radiation balance over water surface*

#### *4.4.1.1 Cloud cover*

To evaluate the effect of cloudiness on the radiation balance of the water surface at Midmar Dam, the radiation balance under clear-sky day (DOY 60) was compared with the radiation balance under overcast day (DOY 67), as shown in Figure 4.9. The $R_n$ fluxes were minimal (ranged between -33 to 111 W $m^{-2}$) for the overcast day compared to a clear-sky day (ranged between -92 to 860 W $m^{-2}$). However, during both overcast and clear-sky days the $R_n$ fluxes followed the same diurnal variability as the $R_s$ fluxes although $R_s$ fluxes were always greater than $R_n$ fluxes. The $R_s$ fluxes were minimal (130 W $m^{-2}$) for the overcast day while maximum (1015 W $m^{-2}$) for the clear-sky day. The maximum $R_s$ fluxes were observed during mid-day (local time 12h30). The minimal $R_s$ fluxes during overcast day are attributed to $R_s$ being

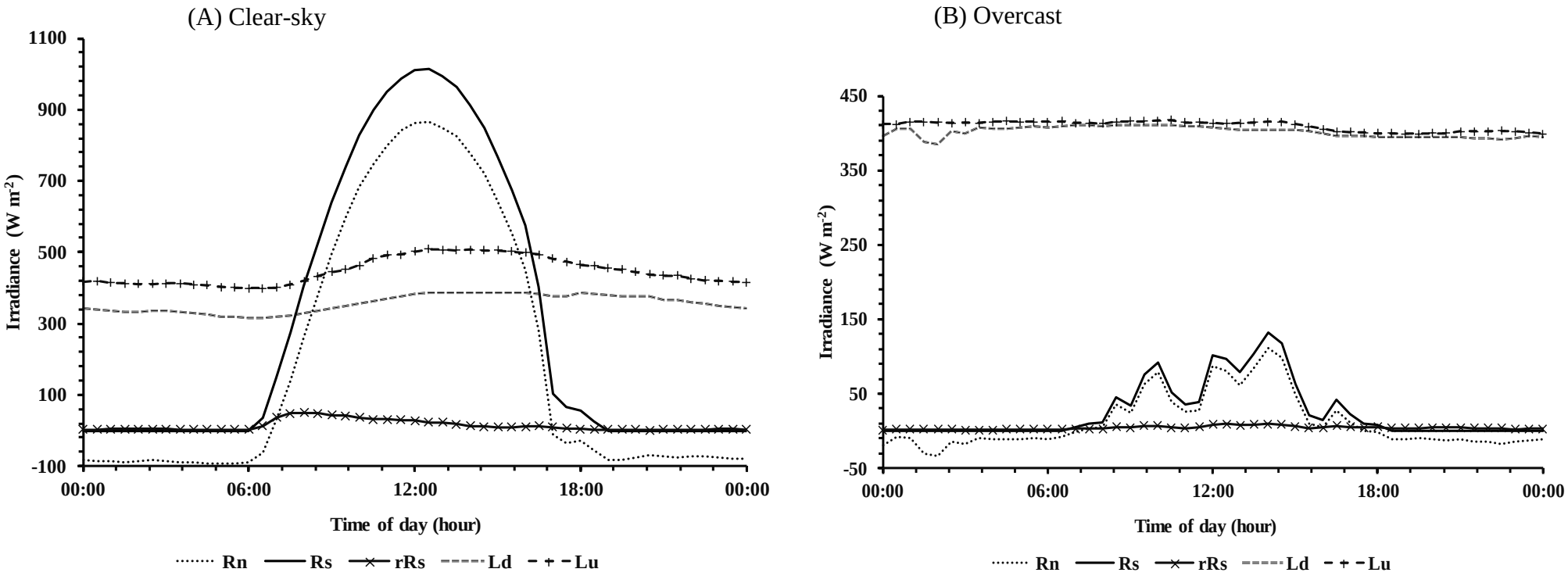


**Figure 4.9 : Radiative fluxes above open water at Midmar Dam for clear-sky (3th March 2016) and overcast conditions (8th March 2016).**

scattered and reflected or absorbed by clouds, also noted by Finch and Hall (2001). The $rR_s$ fluxes followed the same diurnal variability as the $R_s$ during both clear-sky and overcast days. However, $rR_s$ fluxes showed minimal diurnal variability compared to $R_s$ during both clear-sky and overcast days. During the overcast day, $R_n$ fluxes were always (day and night) dominated by $L_u$ and $L_d$, respectively while during the clear-sky day, $R_n$ fluxes were dominated by $R_s$ during the daytime and dominated by $L_u$ and $L_d$, respectively during the night-time. However, during both overcast and clear-sky days the $R_n$ fluxes were always directed towards the water surface during day, while at night the $R_n$ fluxes were much weaker and directed away from the water surface and these observations were consistent with results reported by Mahmud *et al.* (2015). These observations were more pronounced under clear-sky day than overcast day. The night-time radiative cooling (negative $R_n$ fluxes) is attributed to a much greater $L_u$ than $L_d$ during night-time where $R_s$ was zero, as also noted by Arya (2001). During clear-sky day, $L_u$ was much greater than $L_d$ while during overcast day the difference between $L_u$ and $L_d$ was minimal indicated that greater $L_d$ was emitted during the overcast day compared to the clear-sky day. Cloud cover had no effect on $L_u$ since with constant emissivity, $L_u$ depends on surface water temperature alone.

*4.4.1.2 Reflection coefficient of water*

*4.4.1.2 (a) Variability of reflection coefficient of water*

The reflection coefficient of water ($r$) directly determines the amount of $R_s$ absorbed by the water surface. The diurnal variability of $r$ indicated that $r$ was higher just after the sunrise (local time 06h30) and decrease to minimal during late mid-day (local time 14h30) and then start to increase to its maximum during the sunset (local time 17h30) for water at Midmar Dam for the 29th March 2016 (cloudless) is presented in Figure 4.10. The observed diurnal variability of $r$ indicated that high $r$ were observed during lower sun's angles (during sunrise and sunset) and lower $r$ were observed during the daytime when the sun was perpendicular to the water surface. These observations were consistent to the results reported by Finch and Hall (2001) who noted that at lower sun's angles, there is high water reflectivity.

Measurements of $r$ at 30-minute timestamp were used to calculate the daily-average $r$. The temporal variability of the daily $r$ for the entire study period indicated that $r$ ranged between 0.05 and 0.14 (Figure 4.11). The maximum daily $r$ values were observed during the days with

high rainfall, for example DOY 67, 68 and 93 with rainfall of 46, 18, and 7 mm, respectively. The thunderstorms resulted on the presence of suspended particulate matter which may increase $r$. A turbid water body reflected more $R_s$, as consequence measured $R_n$ fluxes were low during

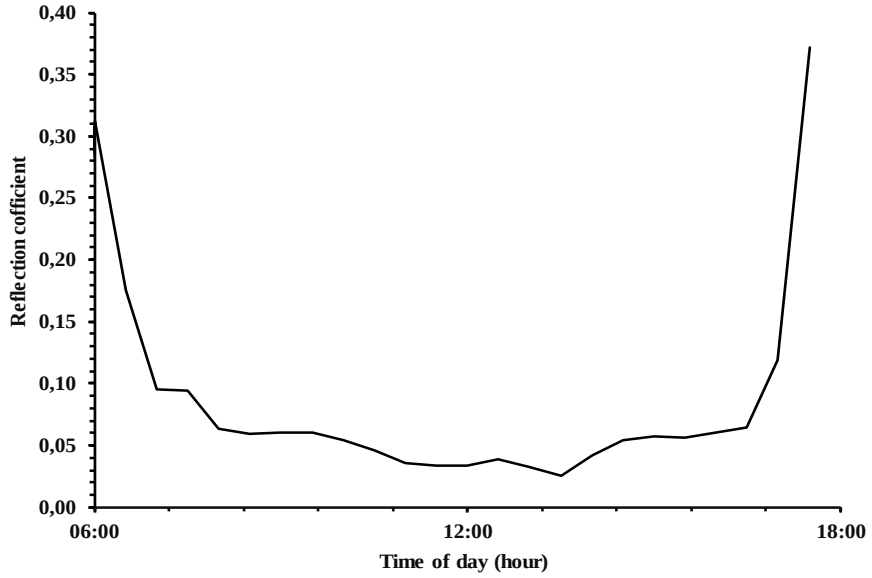


**Figure 4.10: The diurnal variability of reflection coefficient of water at Midmar Dam for the 29th March 2016 (cloudless).**

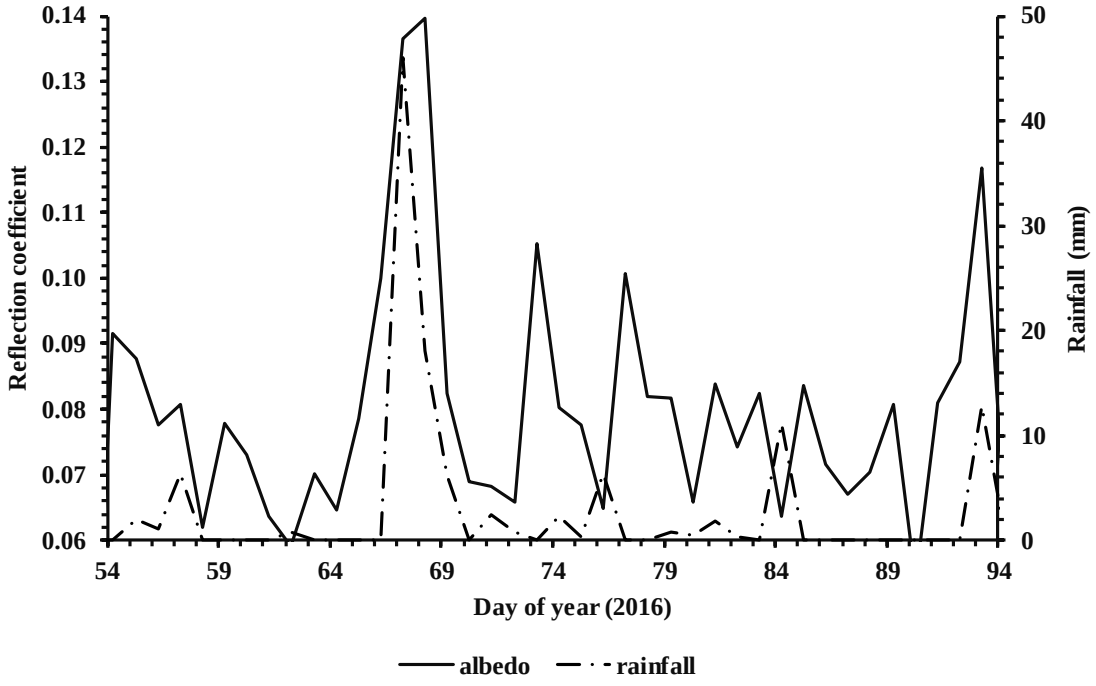


**Figure 4.11: The temporal graph showing the daily reflection coefficient of water measured at Midmar Dam from 24th February to 4th April 2016.**

the day just after heavy rain as also noted by Finch and Hall (2001). Furthermore, the greater cloud cover during rainy days could have increased the $r$ values as also noted by Timofeyev and Vasil′ev (2008). However, a daily-average of 0.08 was observed during the entire study period which is in consistent with the $r$ used in the DPMETHS model.

*4.4.1.2 (b) Effects of reflection coefficient on radiation balance over water surface*

To evaluate the effect of $r$ on the radiation balance over water surface, a constant $r$ of 0.08 was used to calculate $rR_s$ from measurements of $R_s$ above water surface. The comparison between the calculated daily $rR_s$ and observed daily $rR_s$ indicated that for high values of $rR_s$ (> 1.2 MJ $m^{-2}$), the calculated $rR_s$ fluxes were always greater than the observed $rR_s$ fluxes (Figure 4.12). However, for low values of $rR_s$ (< 0.4 MJ $m^{-2}$), the calculated $rR_s$ fluxes were equal to the observed $rR_s$. For the entire study period, the calculated $rR_s$ fluxes were greater than the observed $rR_s$ fluxes by an average of 0.64 MJ $m^{-2}$. These observations imply that assuming a constant $r$ of 0.08 during computation of $rR_s$ could result in slight under-simulation of $R_n$ due to over-estimation of $rR_s$ which reduces $R_s$.

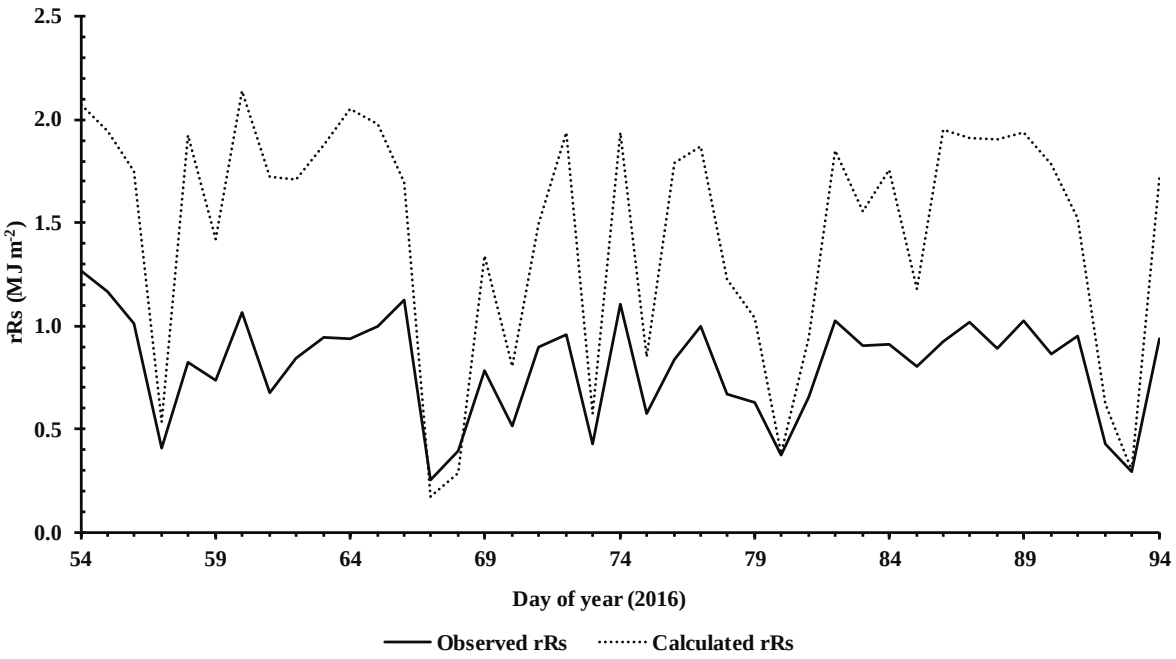


**Figure 4.12: The temporal graph showing the calculated daily $rR_s$ and observed daily $rR_s$ above open water at Midmar Dam from 24th February to 4th April 2016.**

*4.4.1.3 Air and surface water temperature*

To evaluate the effect of $T_{air}$ and $SWT$ on the radiation balance over water surface at Midmar Dam, the variability of both $T_{air}$ and $SWT$ (an average of the two infrared thermometers) acquired above open water were investigated since both $L_u$ and $L_d$ are temperature dependent. The diurnal variability of $T_{air}$ and $SWT$ indicated minimal of the both $T_{air}$ and $SWT$ were observed just before the sunrise (local time 06h30) while maximum temperatures were observed during late afternoon (local time 15h30) (Figure 4.13). During the daytime, $T_{air}$ was warmer than $SWT$ while during the night-time the observations were inverted. The observed diurnal variability of $SWT$ indicated that water surface warms up during the daytime while cools during the night-time. These observations are attributed to $R_n$ fluxes being always directed towards the water surface during the day, while at night the $R_n$ fluxes are much weaker and directed away from the water surface as also noted by Mahmud *et al.* (2015).

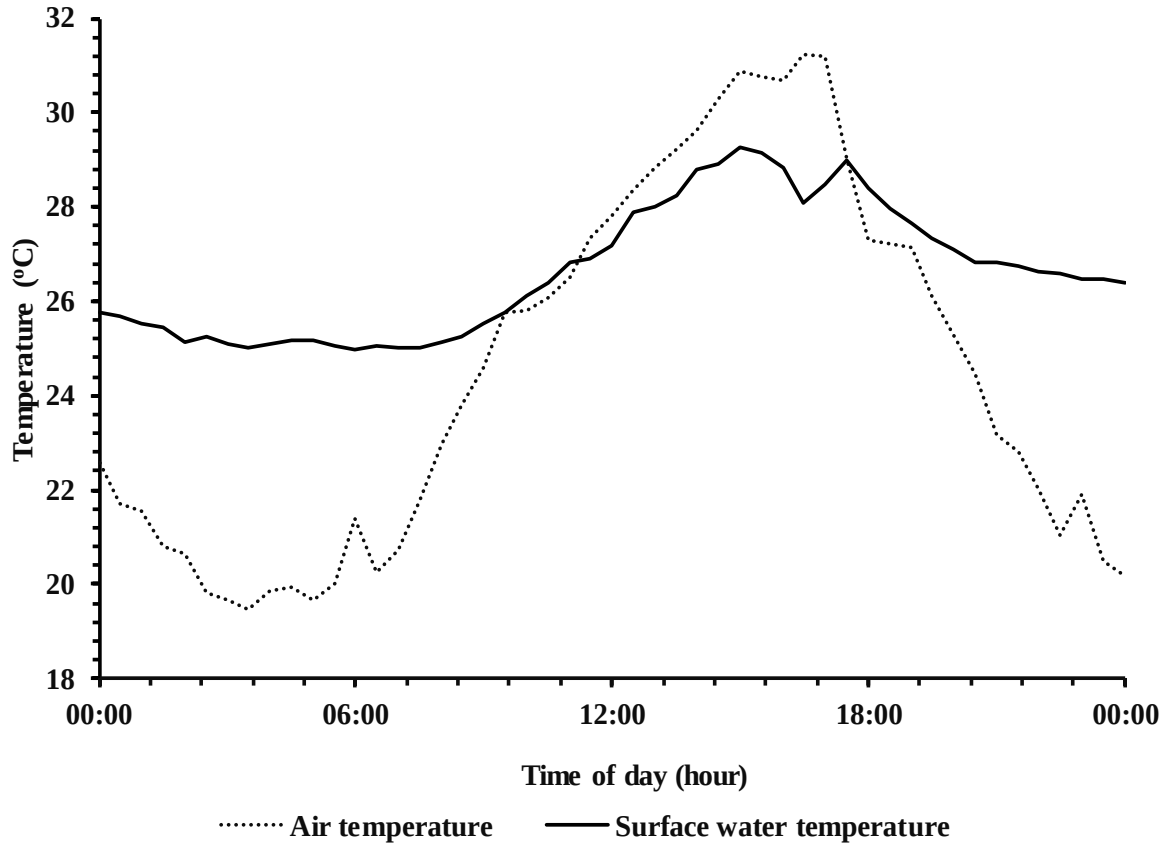


**Figure 4.13: The diurnal variation of the air temperature and surface water temperature at Midmar Dam for the 6th March 2016 (cloudless).**

For entire study period, the comparison between $T_{air}$ and $SWT$ indicated that the daily-average $SWT$ was always warmer than average $T_{air}$ by 3.7 $^{o}$C although both $T_{air}$ and $SWT$ showed similar variability (Figure 4.14). However, $T_{air}$ exhibited a wider range (ranged between 11 and 33 $^{o}$C) than $SWT$ (ranged between 21.5 and 30 $^{o}$C). These results are consistent with observations reported by Lorenzzetti *et al*. (2015). The reduced diurnal range in $SWT$ is attributed to the greater specific heat capacity of water than air. Consequently, water requires a significant amount of energy to change its temperature compared to air. The large heat capacity of water and the absorption of $R_s$ over a large depth combine to reduce the diurnal range of $SWT$ as also noted by Jacobs *et al.* (2008).

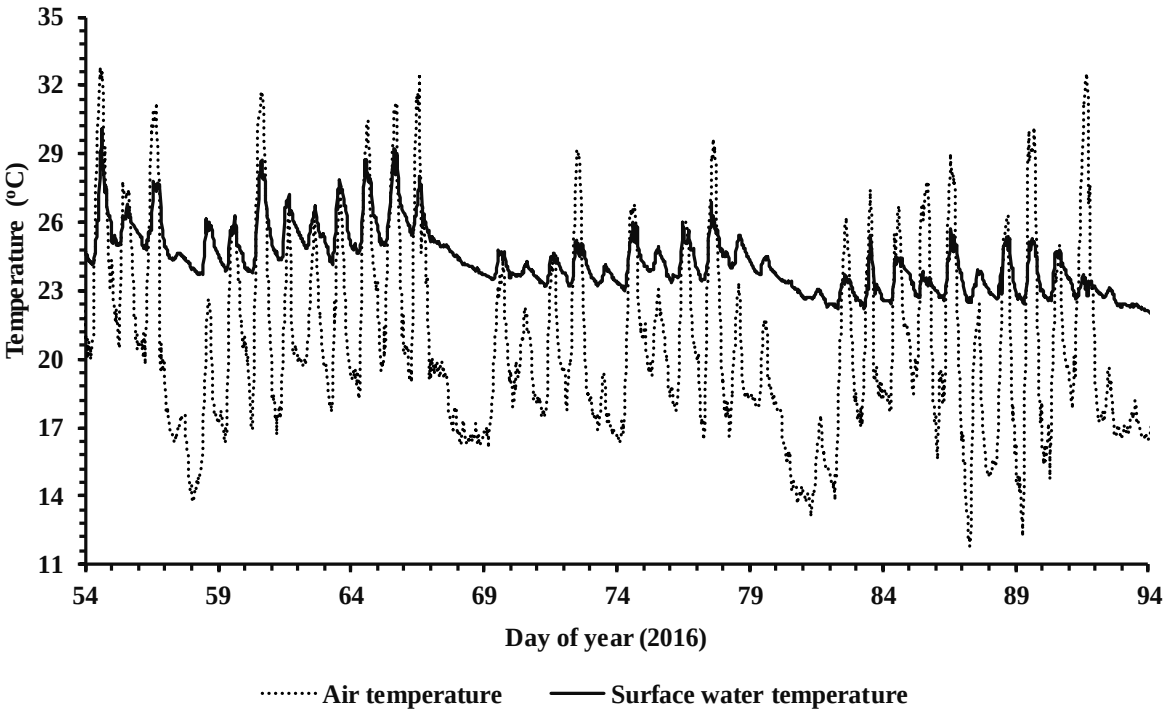


**Figure 4.14: Temporal graph showing variability of the daily-average $T_{air}$ and $SWT$ at Midmar Dam from 24th February to 4th April 2016.**

### *4.4.2 Spatial variability of the radiation balance above water at Midmar Dam*

The downward components of radiation balance can be assumed to be relatively constant over relatively large surface areas except under partially cloudy skies (Federer, 1968). Therefore, any spatial variation of $R_n$ above open water is mainly due to the spatial variability in $SWT$ since with constant emissivity, $L_u$ depends on $SWT$ alone (Wang *et al.*, 2014). However, conducting water temperature surveys using conventional limnological sampling involves

significant financial investment in instrumentation and extensively field work on a reservoir. The spatial variation of $SWT$ across Midmar Dam estimated using Landsat-8 data was used to evaluate the spatial variability of $R_n$ as affected by the variation of $L_u$ which is proportional by the fourth power on $SWT$. There were two Landsat-8 images covering Midmar Dam collected during this study period (i.e. acquired on the 25th February and 12th March). However, only the image acquired on the 25th February had cloud cover less than 60 % and was used in this study. The spatial variability of $SWT$ across Midmar Dam indicated that $SWT$ ranged between 23.4 and 26.0 ºC (Figure 4.15).

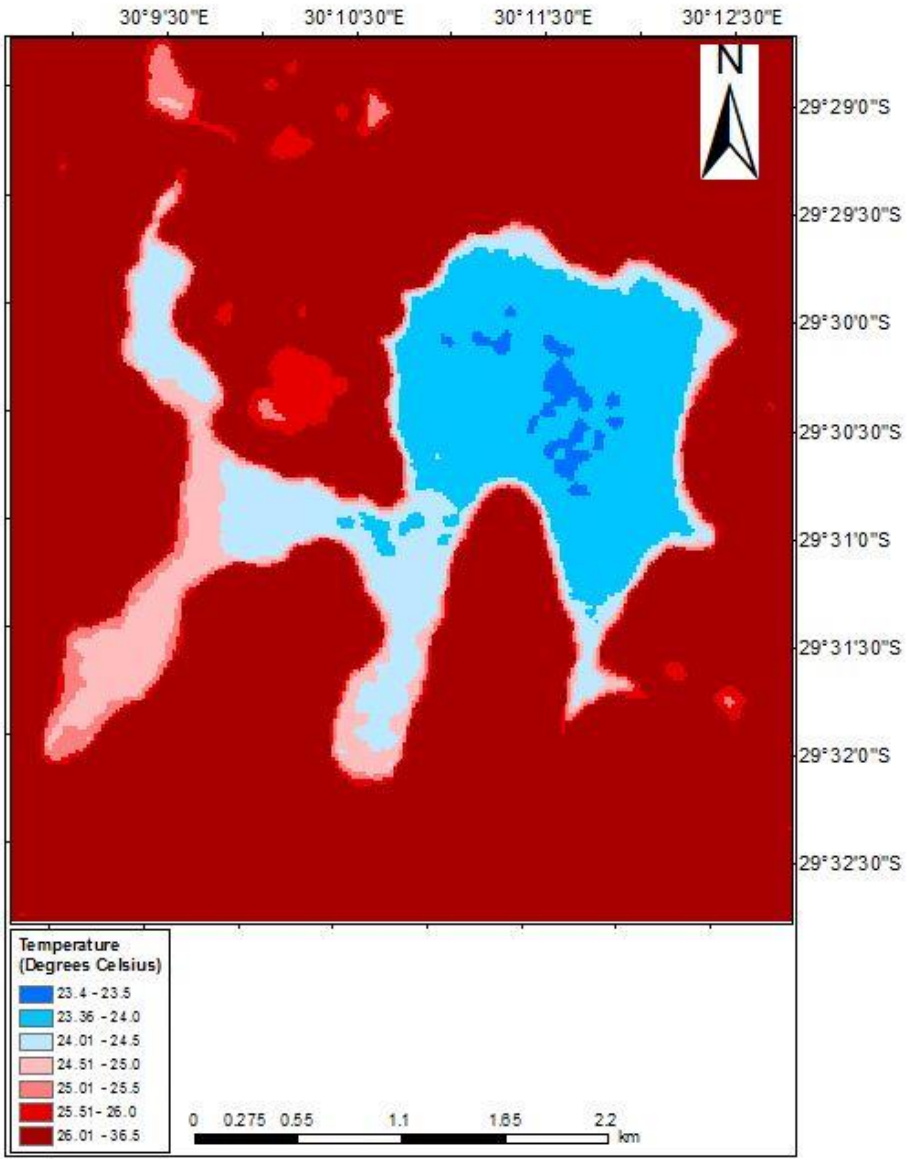


**Figure 4.15: The spatial variability of $SWT$ across Midmar Dam for the 25th February 2016 (cloudless) at 09h50.**

Furthermore, the spatial variability of $SWT$ across Midmar Dam also indicated that water near the shore responded to the atmospheric conditions very quickly compared to the offshore water. Consequently, water near the shore was observed to always be warmer than offshore water by an average of 1.5 $^{o}$C. These observations were consistent with the results reported by Alcântara *et al*. (2010). Furthermore, shallow parts of the dam were 2 $^{o}$C warmer than the deeper part of the dam. Since the north-west was the predominant wind direction during the Landsat-8 overpass time, the south-east water was warmer than north-west by an average of 1.5 $^{o}$C due to warm-surface water being blown from north-west to south-east by wind. The observed average of 1.5 to 2 $^{o}$C variability of $SWT$ across Midmar Dam implies the very low spatial variability of $L_u$ which is temperature dependent. Therefore, the low spatial variability of $SWT$ is associated with low spatial variation of $R_n$ across the dam. These observations indicated that point measurements of $SWT$ are reasonable indicators of the reservoir $SWT$ which is used to compute water-storage heat flux and $L_u$ from water surface at Midmar Dam.

## 4.5 Above-water available energy flux

Above-water available energy flux is the paramount input in energy balance models to estimate open water evaporation and yet is measured directly with greater difficulty because it involves significant financial investment in instrumentation and extensively field work on a reservoir. Consequently, above-water available energy flux is often estimated using the models that utilize meteorological data that are readily available in most standard weather stations. However, for accurate modelling of the above-water available energy flux, it is vital to understand the variability of the above-water available energy flux. To understand the temporal variability of the above-water available energy flux, the two components of the available energy flux (i.e. $R_n$ and water-stored flux) were evaluated.

### *4.5.1 Water-stored heat flux*

The water-stored flux ($G$) was calculated from the 30-min temporal changes in average water temperatures measured at different depths using Eq. (2.4). The daily estimates of $G$ at different water layers were obtained by summing the 30-min $G$ data for each day (00h30 to 24h00). Then, the daily-average $G$ was calculated from $G$ for the different layers of the water profile.

The time series of 30-min temporal variability of $G$ indicated that $G$ was proportional to the depth of water (Figure 4.16). However, the $G$ at different layers of water showed the same

diurnal variability. The minor difference in $G$ stored between the shallowest water layer (0 to 0.02 m) is attributed to shallow (<5 m depth) water reservoirs being well-mixed with little stratification due to the wind-stirring effect as also noted by Gallego-Elvira *et al.* (2011). A running mean of order 3, corresponding to 1.5 h, was used to obtain half-hourly values of $G$. Even with using a running mean, estimates of $G$ fluctuated from negative to positive for each 30-min period, due to turbulent water waves of varying temperature travelling past the thermocouples as also noted by Tanny *et al.* (2008), Mengistu and Savage (2010) as well as Savage (2010). However, $G$ was positive during most of the day and negative during most of the night. These observations are consistent with the results reported by Mahmud *et al.* (2015), suggesting that water acted as a sink of heat during the daytime and a source of heat during the night-time. The maximum heat storage was observed just before the sunset (local time16h00) while the maximum rapid release of stored heat was just after the sunset (local time 18h00).

For the entire study period, the temporal variability of $G$ showed that during some days, heat was stored in water storage ($G$ > 0 W m$^{-2}$) while during other days, heat was released from water storage ($G$ < 0 W m$^{-2}$) (Figure 4.17). The net heat flux loss in the water storage was observed during days with low daily $R_s$ while net heat flux gain was observed during days with high daily $R_s$. For example, during the DOY 73 with daily $R_s$ of 7.1 MJ m$^{-2}$, net heat flux was released from the water storage (-15 MJ m$^{-2}$ was loss between the depth of 0.08 and 0.16 m). However, during the DOY 74 daily $R_s$ of 24.1 MJ m$^{-2}$, net heat was stored in the water storage (31 MJ m$^{-2}$ was stored between the depth of 0.08 and 0.16 m). These observations indicate that $G$ plays a significant role in the daily energy balance and cannot be neglected for accurate estimation of the daily open water evaporation as also noted by a number of authors (e.g. Finch and Hall (2001), Tanny *et al.* (2008), Jensen (2010), Savage (2010) as well as Mengistu and Savage (2010).)

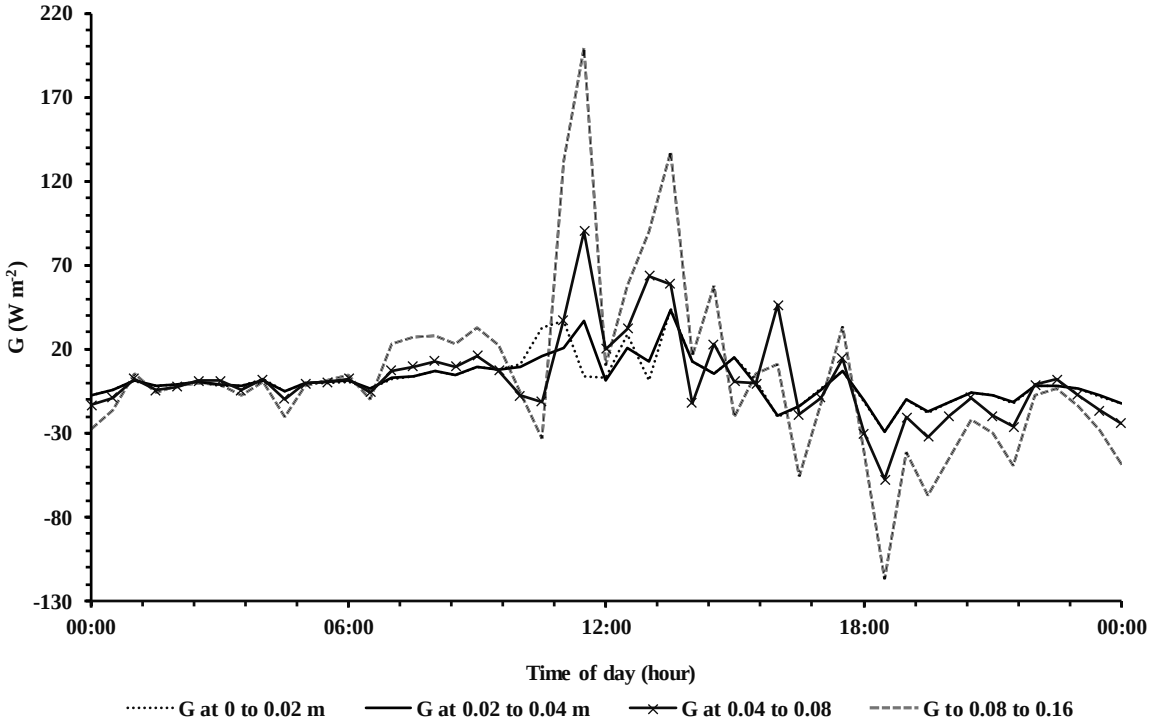


**Figure 4.16: The diurnal variability of *G* measurements at different water depth increments for Midmar Dam for the 1th March 2016 (cloudless).**

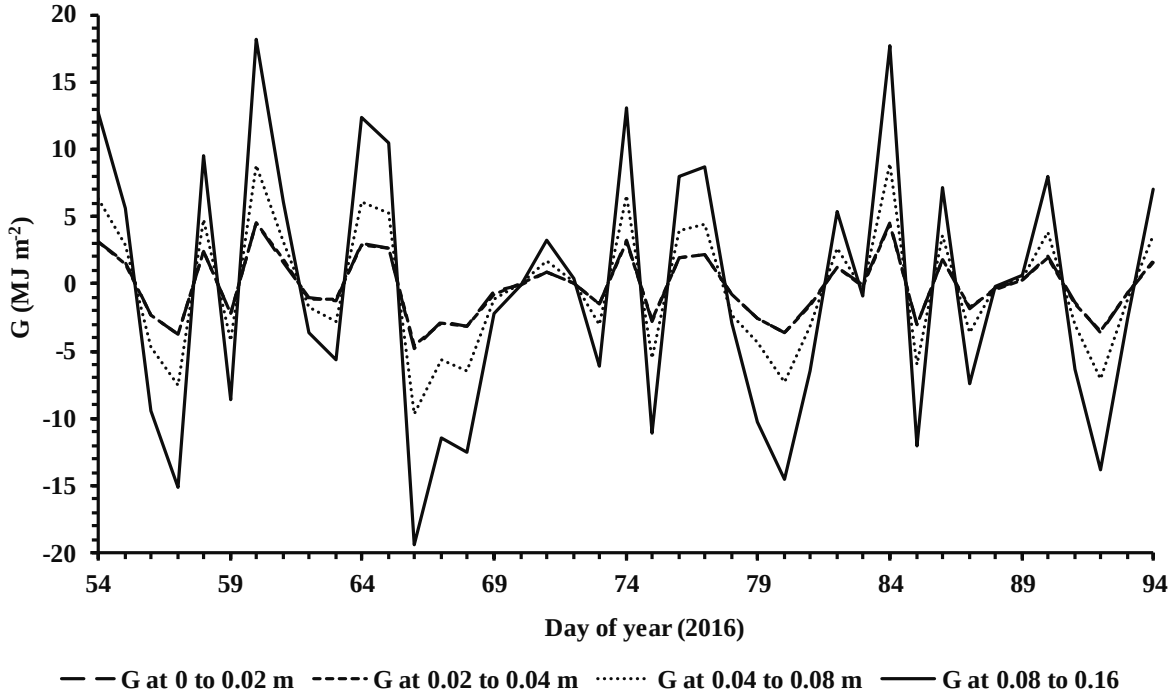


**Figure 4.17: Temporal variability of *G* measurements at different water depth increments for Midmar Dam from 24th February to 4th April 2016.**

### *4.5.2 Variability of the available energy flux components above water*

Estimates of $G$ fluxes of the dam showed a very wide variation that was not attributed to variation in $R_n$ and were unreliable. As an example, during DOY 56, the temporal variation in both $R_n$ and $G$ indicated that $G$ showed a similar diurnal variation to $R_n$ with comparable magnitudes and peaked at the same time as the peak in $R_n$, as also noted by Savage (2010) (Figure 4.18). Maximum of both $R_n$ and $G$ fluxes were observed during the daytime (around 13:30 local standard time) and were negative during night-time. During the daytime, $R_n$ fluxes were positive, corresponding to a source of energy while during night-time, $R_n$ were negative, corresponding to a loss of energy from the water surface as also noted by Alcântara *et al.* (2010).

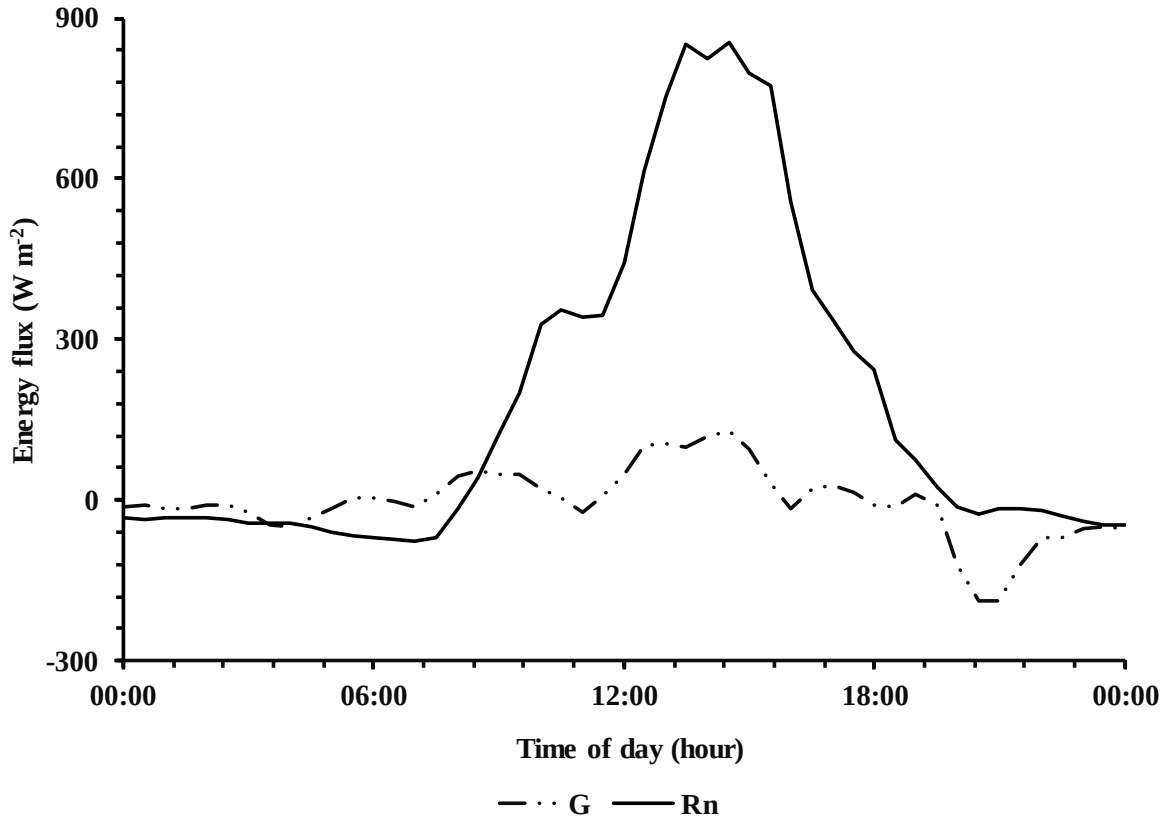


**Figure 4.18: The diurnal variation in the measured 30-min fluxes of $G$ and $R_n$ for the 26th February (DOY 56) 2016 (cloudless).**

However, during DOY 66, the temporal variation in both $R_n$ and $G$ indicated that $G$ showed a similar diurnal variation to $R_n$ but in the late afternoon (around 14h00 local standard time) a large decrease of $G$ to -71 W m$^{-2}$ compared to $R_n$ of 843 W m$^{-2}$ and immediately there was a sudden and unexplained increase of $G$ to 52 W m$^{-2}$ compared to $R_n$ of 455 W m$^{-2}$ (Figure 4.19).

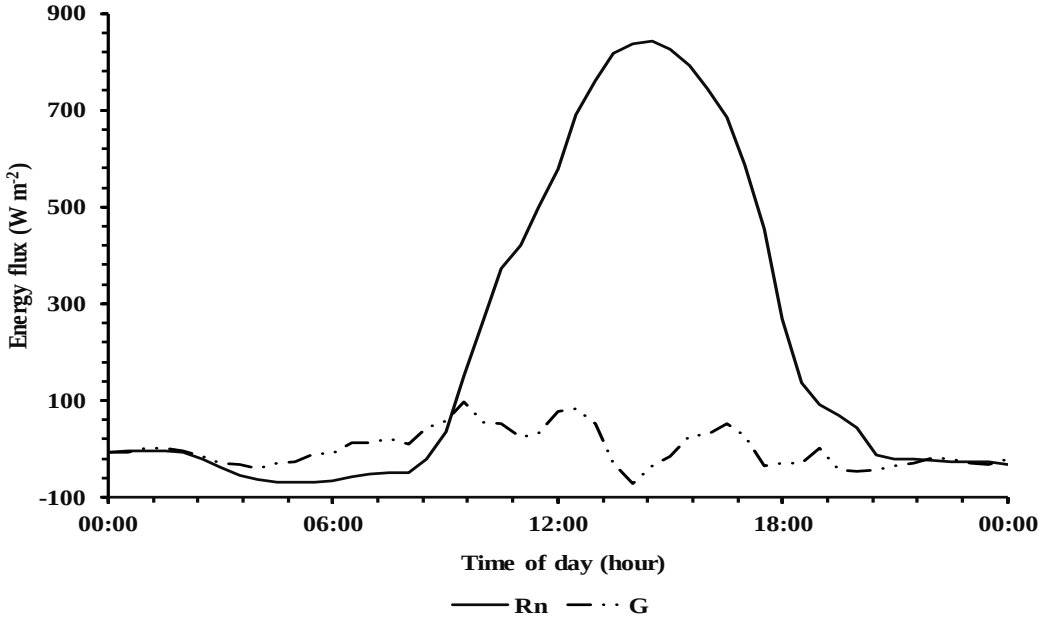


**Figure 4.19: The diurnal variation in the measured 30-min fluxes of $G$ and $R_n$ for the 13th March (DOY 66) 2016 (cloudless).**

For the entire study period, the comparison between the calculated daily-average $G$ and the measured daily $R_n$ indicated that daily $G$ follow the same variability to daily $R_n$ most of the time during the entire study period (Figure 4.20). The regression graph of the $R_n$ and $G$ indicated that daily $G$ accounted for up to 47 % of the daily $R_n$ (Figure 4.21). These observations are consistent with results reported by Mengistu and Savage (2010) at the same study site.

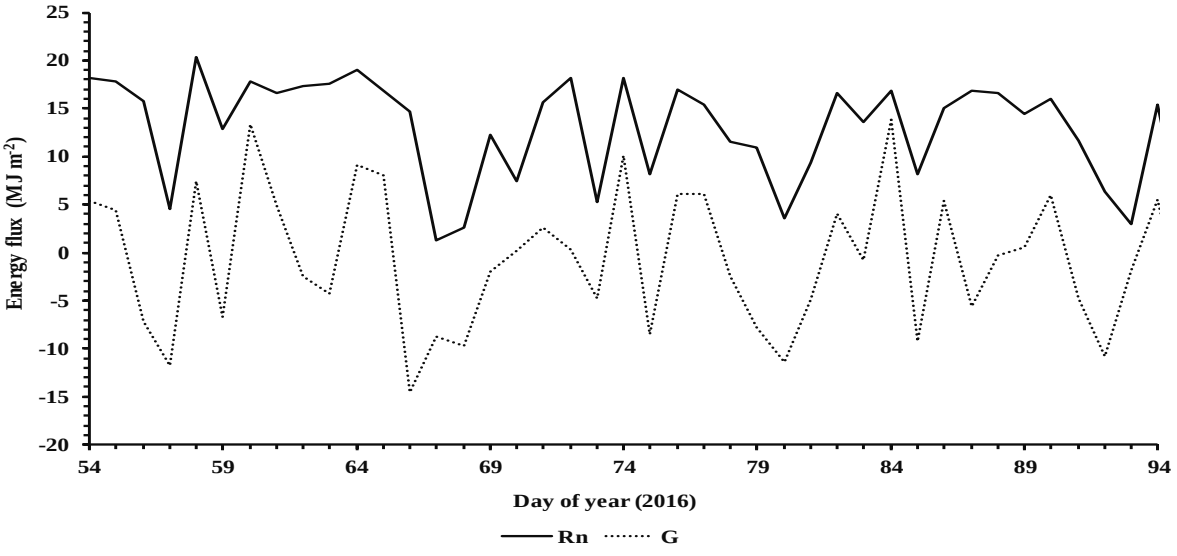


**Figure 4.20: Temporal graph showing the variability of $G$ and $R_n$ measurements for Midmar Dam from 24 February to 4 April 2016.**

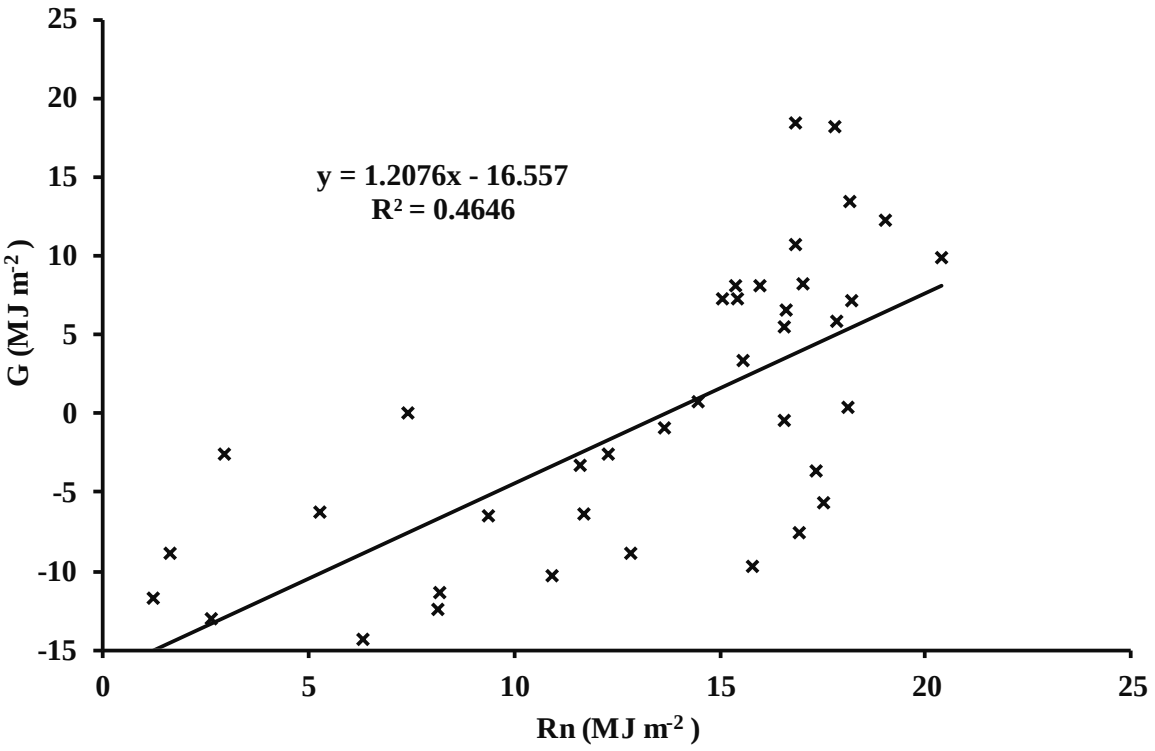


**Figure 4.21: The regression graph of the daily $G$ vs $R_n$ for Midmar Dam from 24 February to 4 April 2016.**

### 4.6 Modelling study at Midmar Dam

The DPMETHS model of Savage *et al*. (2016) that utilises the land-based meteorological data and the concepts of equilibrium temperature to estimate available energy flux at the water storage was new and the promising model that has not been used in any known study in South Africa for open water. To evaluate the performance of the DPMETHS model to simulate available energy flux at water storage, basic meteorological data obtained from the land-based station located near the dam were used as the inputs to the DPMETHS.

#### *4.6.1 Comparisons between land and water meteorological measurements*

Everson (1999) noted that large errors in the model simulations could be introduced using land-based meteorological data that do not represent conditions over open water surfaces. To investigate the relationships between meteorological measurements made over water and land-based measurements, the comparisons were made between 30-min meteorological data from water-based and land-based stations for the period between 24$^{th}$ February to 9$^{th}$ March 2016.

The choice of these data sets was based on quality of hourly data available from the land-based station. The main aim of comparing these data sets was to justify the use of land-based measurements as an input to the DPMETHS model to simulate the available energy fluxes over open water surface at Midmar Dam.

4.6.1.1 Solar irradiance

A comparison between the daily total solar irradiance measured above water surface ($R_{s\,water}$) and that measured at the land surface ($R_{s\,land}$) indicated that about 94 % variation in the $R_{s\,water}$ can be explained by $R_{s\,land}$ (Figure 4.22).

4.6.1.2 Air temperature

Temporal variation in air temperature measured above water ($T_{air\,water}$) and that measured at land surfaces ($T_{air\,land}$) indicated that $T_{air\,land}$ followed the same diurnal variation as $T_{air\,water}$ (Figure 4.23). A comparison between $T_{air\,water}$ and $T_{air\,land}$ indicated that about 97 % variation in the $T_{air\,water}$ can be explained by the $T_{air\,land}$ (Figure 4.24).

4.6.1.3 Wind speed

Temporal variation in wind speed measured above land surface ($U_{land}$) and that measured above water surface ($U_{water}$) indicated that $U_{land}$ followed the same diurnal variation as $U_{water}$ (Figure 4.25). Unexpectedly, $U_{water}$ was maximum during night-time and minimal early in the morning. Furthermore, $U_{water}$ was always greater than $U_{land}$ due to open fetch on the water-based station compared to the land-based station which was closer to the buildings and trees. The smoother surface of open water compared to land could have resulted in greater wind speeds over the water surface than the land. These results are consistent with the observations reported by Finch and Hall (2001).

4.6.1.4 Relative humidity

Temporal variation in relative humidity measured above land surface ($RH_{land}$) and that measured above water surface ($RH_{water}$) indicated that $RH_{land}$ followed the same diurnal variation as $RH_{water}$, relative humidity being maximum during night-time and minimal during daytime (Figure 4.26). A comparison between $RH_{water}$ and $RH_{land}$ indicated that about 85 % variation in the $RH_{water}$ can be explained by the measured $RH_{land}$ (Figure 4.27).

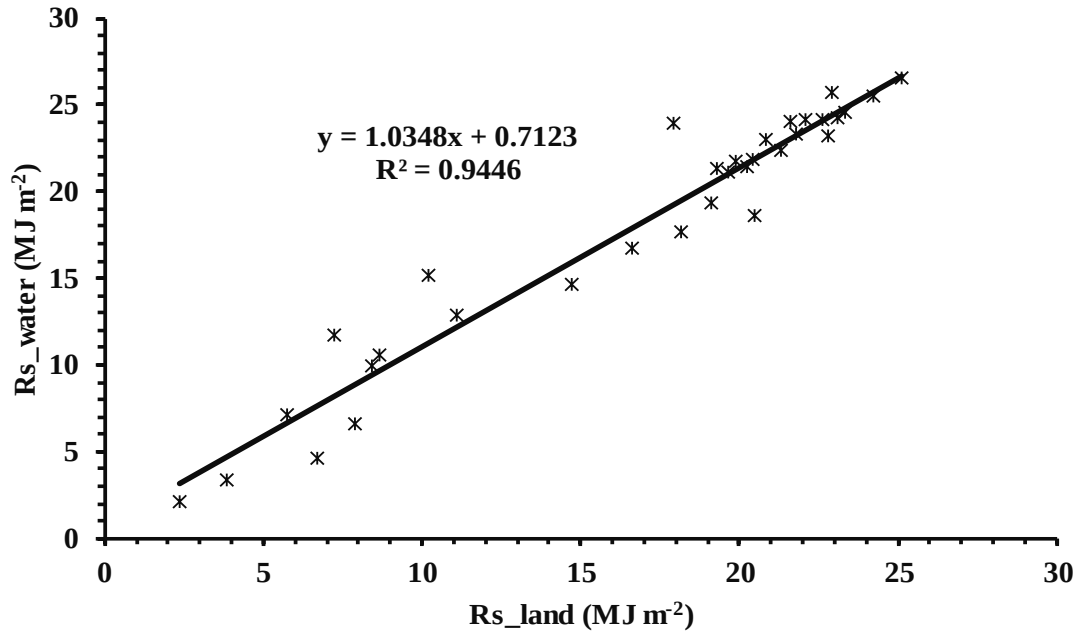


**Figure 4.22: Regression graph of $R_{s\ water}$ and $R_{s\ land}$ for the period between 24th February and 9th March 2016 at Midmar Dam.**

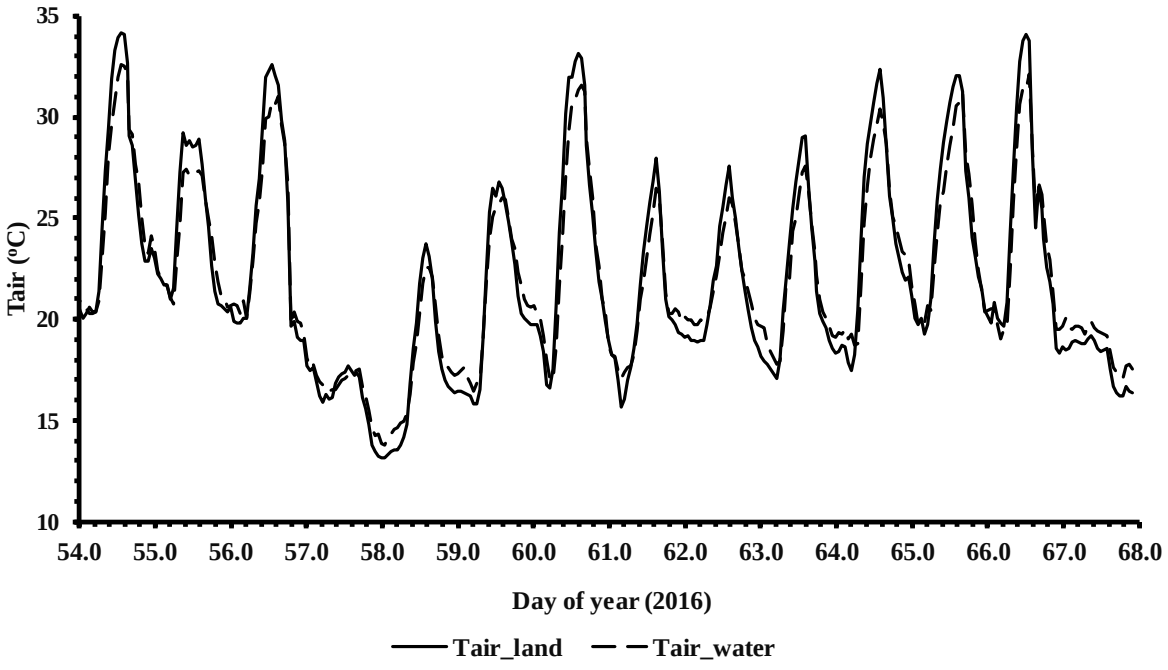


**Figure 4.23: Temporal variation in $T_{air\ water}$ and $T_{air\ land}$ for the period between 24th February and 9th March 2016 at Midmar Dam.**

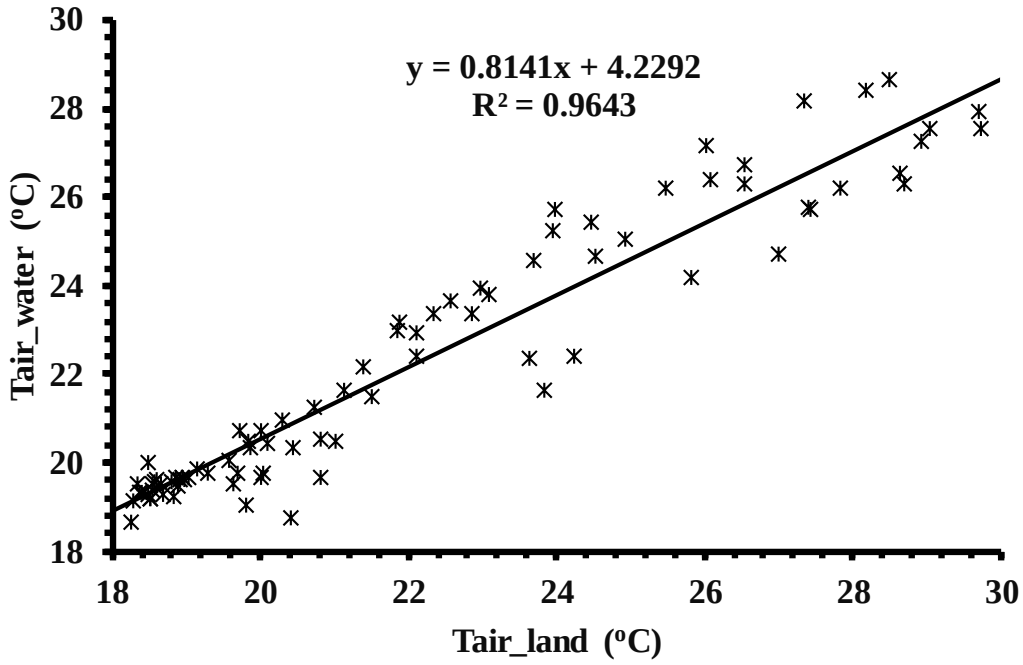


**Figure 4.24: Regression plot of $T_{air\ water}$ vs $T_{air\ land}$ for the period between 24th February and 9th March 2016 at Midmar Dam.**

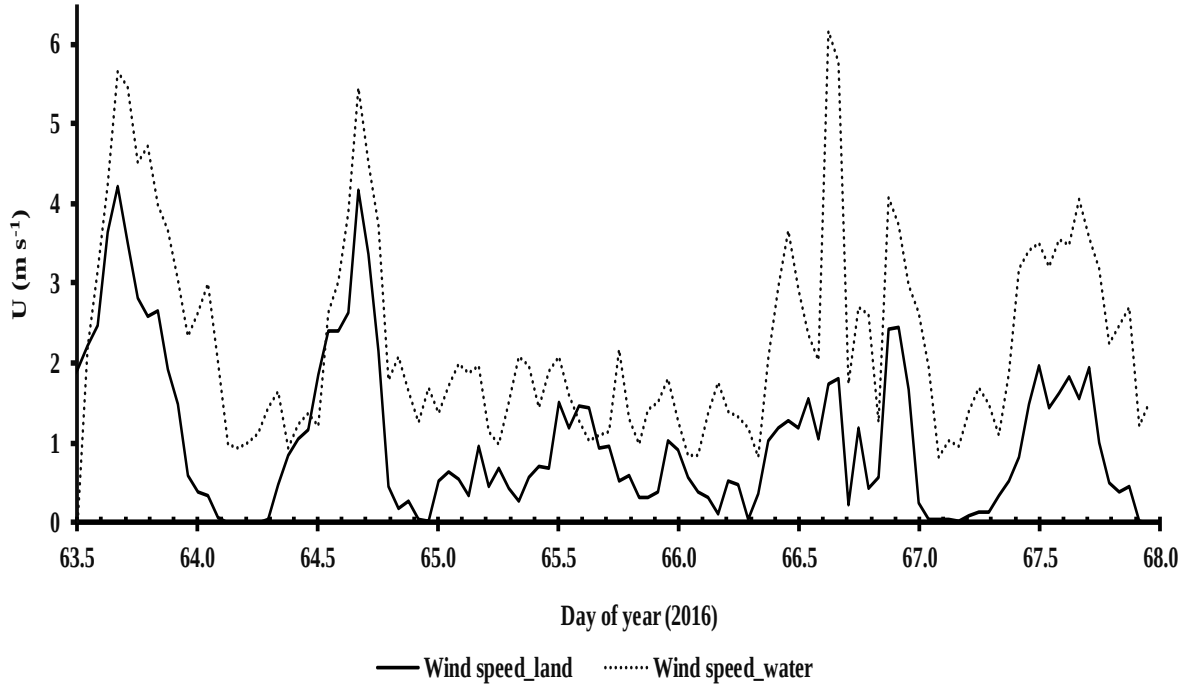


**Figure 4.25: Temporal variation in $U_{water}$ and $U_{land}$ for the period between 24th February and 9th March 2016 at Midmar Dam.**

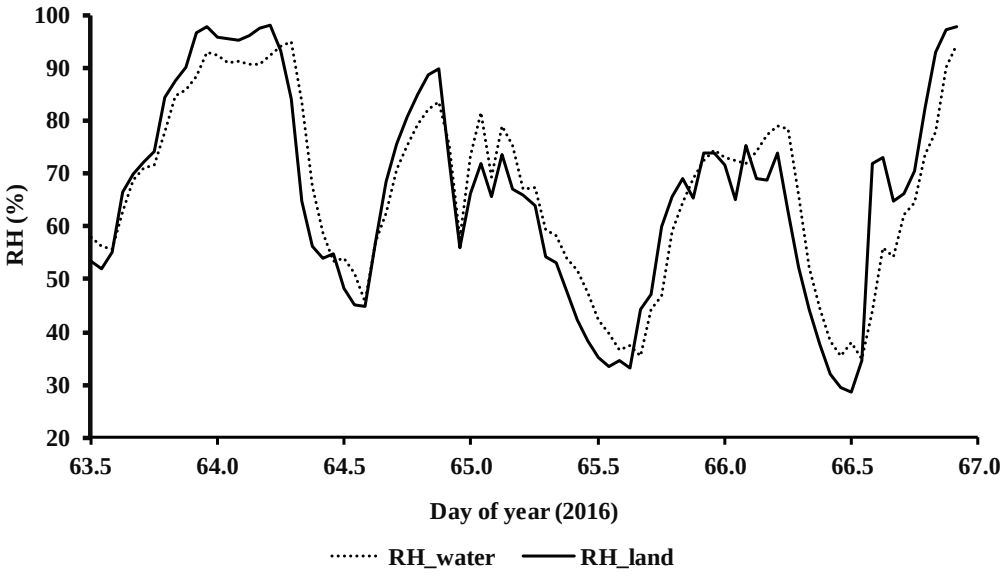


**Figure 4.26: Temporal variation in $RH_{water}$ and $RH_{land}$ for the period between 24th February and 8th March 2016 at Midmar Dam.**

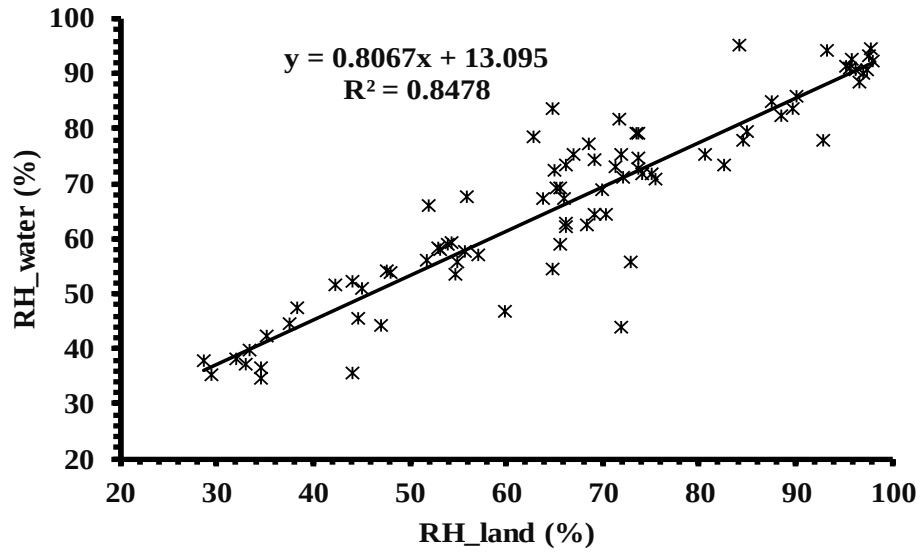


**Figure 4.27: Regression plot of $RH_{water}$ vs $RH_{land}$ for the period between 24th February and 8th March 2016 at Midmar Dam.**

4.6.1.5 General comments

Although there were differences between the measurements made over water and land-based measurements, good relationships were observed between these meteorological measurements. Therefore, there was no need to adjust the land-based data for modelling purposes.

### *4.6.2 Modelling radiative fluxes*

Estimates of $R_s$, $L_d$, and $L_u$ are computed within the DPMETHS during the computation of $R_n$ from the land-based meteorological data using the iterative procedure. To evaluate the performance of the DPMETHS model to simulate $R_n$ above water storage, the comparisons were made between the daily estimates of the radiative fluxes predicted from the DPMETHS model and the daily radiative fluxes measured above water at Midmar Dam.

#### 4.6.2.1 Solar irradiance

The relationship between the daily estimates of $R_s$ predicted from the DPMETHS model and the daily $R_s$ measured above water indicated reasonable agreement (Figure 4.28). The regression graph between estimates of $R_s$ and measured $R_s$ indicated the statistically significant relationship between estimates of $R_s$ and measured $R_s$, with slope ($m$) of 0.58 and regression coefficient ($r^2$) of 0.8 and intercept of 7.16 MJ m$^{-2}$ (Figure 4.29). The $r^2$ indicated that about 80 % variation in the measured $R_s$ can be explained by the model estimates of $R_s$. The root mean square error (RMSE) of 3.71 MJ m$^{-2}$ indicated the model simulates $R_s$ very well. However, the mean bias error (MBE) of 0.50 MJ m$^{-2}$ indicated that the model over-simulated $R_n$ during other days although such a small value of MBE indicated a better model performance. The calculated t-statistic value of 0.8 which was much less than the critical t-value of 2.66 obtained from the statistical tables indicated that estimates of $R_s$ and measured $R_s$ fluxes were not statistically different at the 99.5 % level of confidence.

#### 4.6.2.2 Incoming infrared irradiance

The comparisons between the daily estimates of $L_d$ predicted from the DPMETHS model and the daily $L_d$ measured above water indicated reasonable agreement with both following the same variation (Figure 4.30). However, the model over-simulated the high values of $L_d$ while under-simulated low values of $L_d$. The RMSE of 2.39 MJ m$^{-2}$ indicated the model simulates $L_d$ fairly. However, the MBE of 1.05 MJ m$^{-2}$ indicated that the model often over-simulated $L_d$. The calculated t-statistic value of 3.1 which was greater than the critical t-value of 2.66 obtained from the statistical tables indicated that the estimated $L_d$ and measured $L_d$ fluxes were statistically different at the 99.5 % level of confidence.

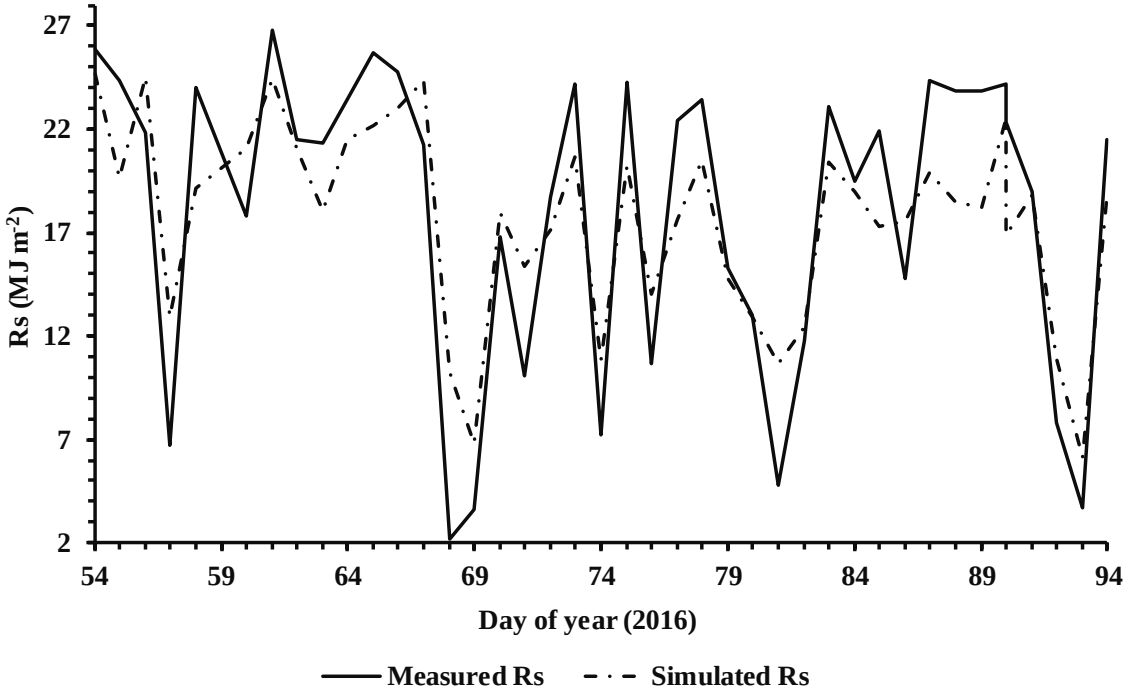


**Figure 4.28: The comparison between the daily measured and the simulated $R_s$ above open water at Midmar Dam from 24th February to 4th April 2016.**

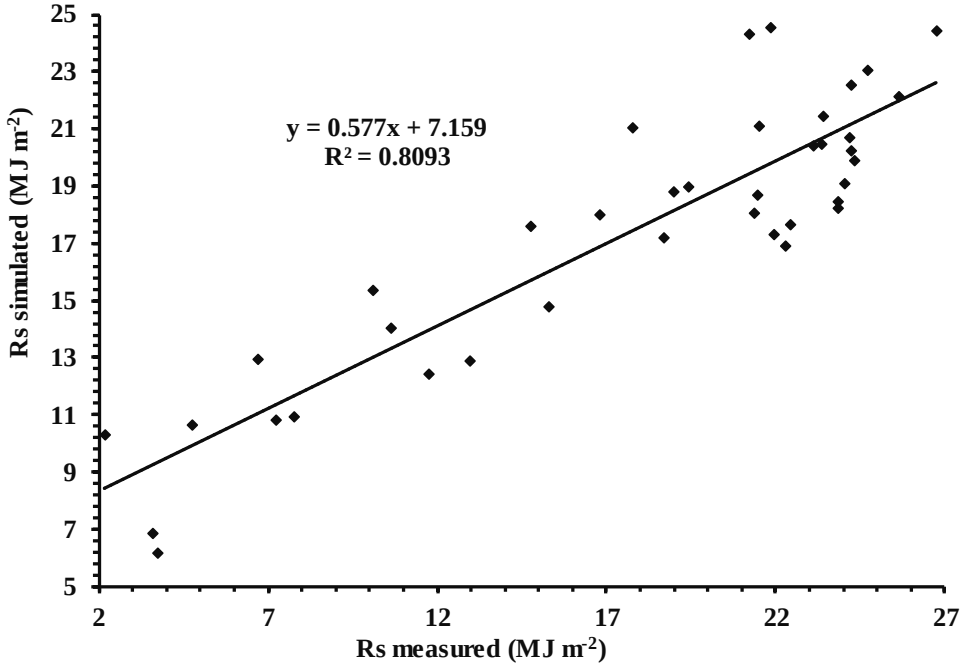


**Figure 4.29: The regression graph of the measured and the simulated $R_s$ above open water at Midmar Dam from 24th February to 4th April 2016.**

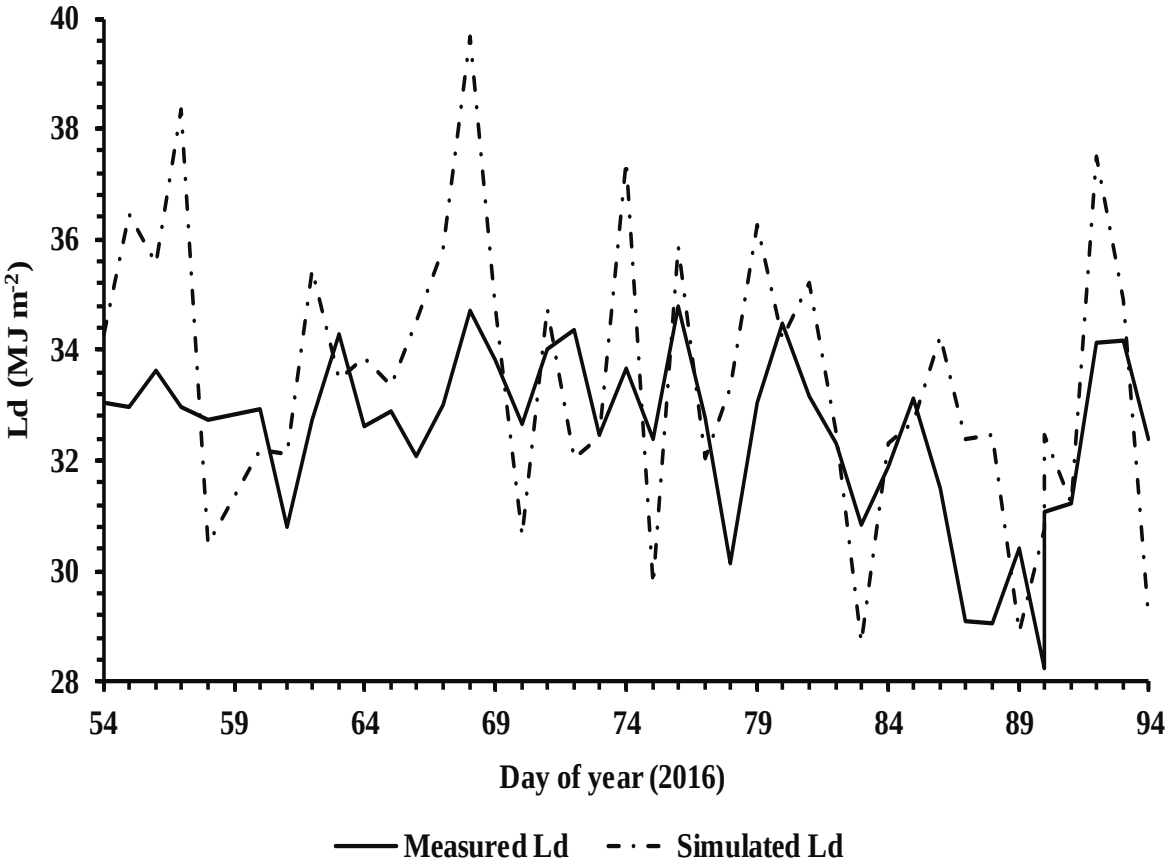


**Figure 4.30: The comparison between the daily measured and the simulated $L_d$ above open water at Midmar Dam from 24th February to 4th April 2016.**

4.6.2.3 Outgoing infrared irradiance

The comparisons between the daily estimates of $L_u$ predicted from the DPMETHS model and the daily $L_u$ measured above water indicated reasonable agreement with both following the same variation (Figure 4.31). The RMSE of 1.30 MJ $m^{-2}$ indicated the model simulates $L_u$ very well. However, the MBE of 0.58 MJ $m^{-2}$ indicated that the model often over-simulated $L_u$ although such a small value of MBE indicated a better model performance. The calculated t-statistic value of 3.1 which was greater than the critical t-value of 2.66 obtained from the statistical tables indicated that the estimated $L_d$ and measured $L_d$ fluxes were statistically different at the 99.5 % level of confidence.

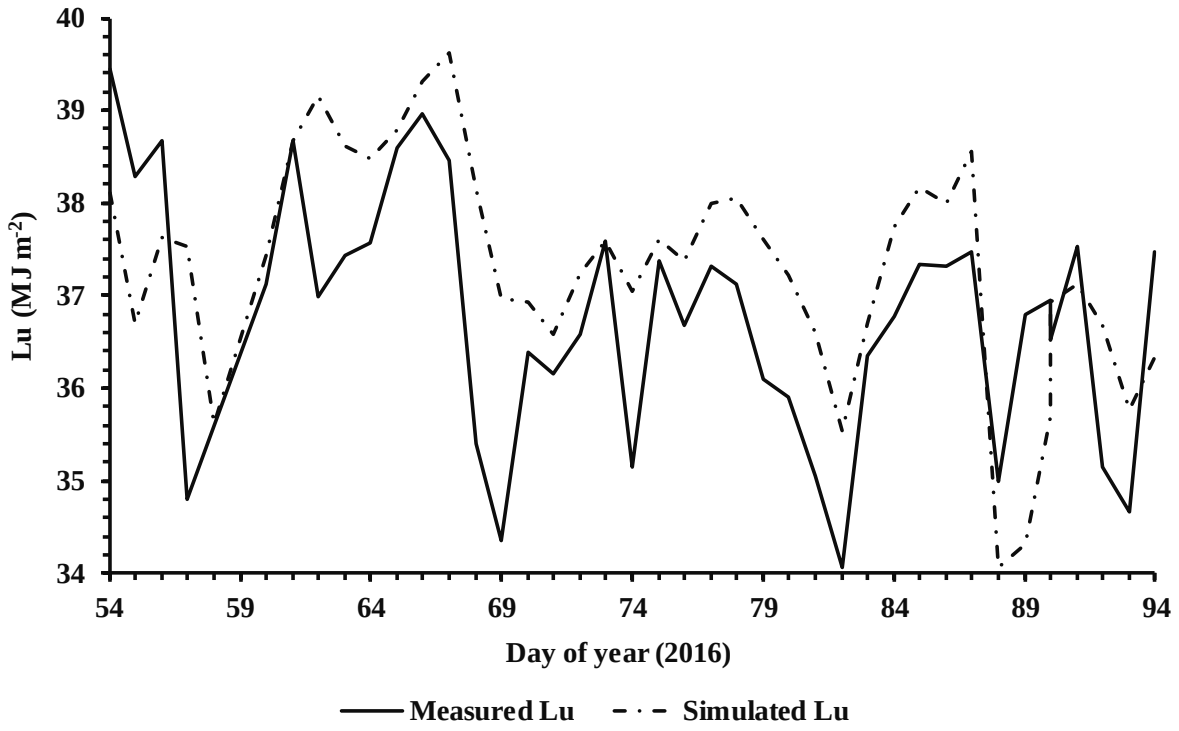


**Figure 4.31: The comparison between the daily measured and the simulated $L_u$ above open water at Midmar Dam from 24th February to 4th April 2016.**

4.6.2.4 Net irradiance

The relationship between the daily estimates of the net irradiance ($R_{ne}$) predicted from the DPMETHS model using standard weather data and the daily net irradiance measured above water ($R_n$) was good (Figure 4.32). The regression graph between $R_n$ and $R_{ne}$ indicated the statistically significant relationship between $R_n$ and $R_{ne}$, with $m$ of 0.76 and $r^2$ of 0.70 and intercept of 3.60 MJ m$^{-2}$ (Figure 4.33). The $r^2$ indicated that about 70 % variation in the $R_n$ can be explained by the $R_{ne}$. The smaller RMSE of 3.04 MJ m$^{-2}$ indicated the model simulates $R_n$ very well. However, the MBE of 0.70 MJ m$^{-2}$ indicated that the model over-simulated $R_n$ during other days although such a small value of MBE indicated a better model performance. The calculated t-statistic value of 1.5 which was less than the critical t-value of 2.66 obtained from the statistical tables indicated that $R_n$ and $R_{ne}$ fluxes were not statistically different at the 99.5 % level of confidence.

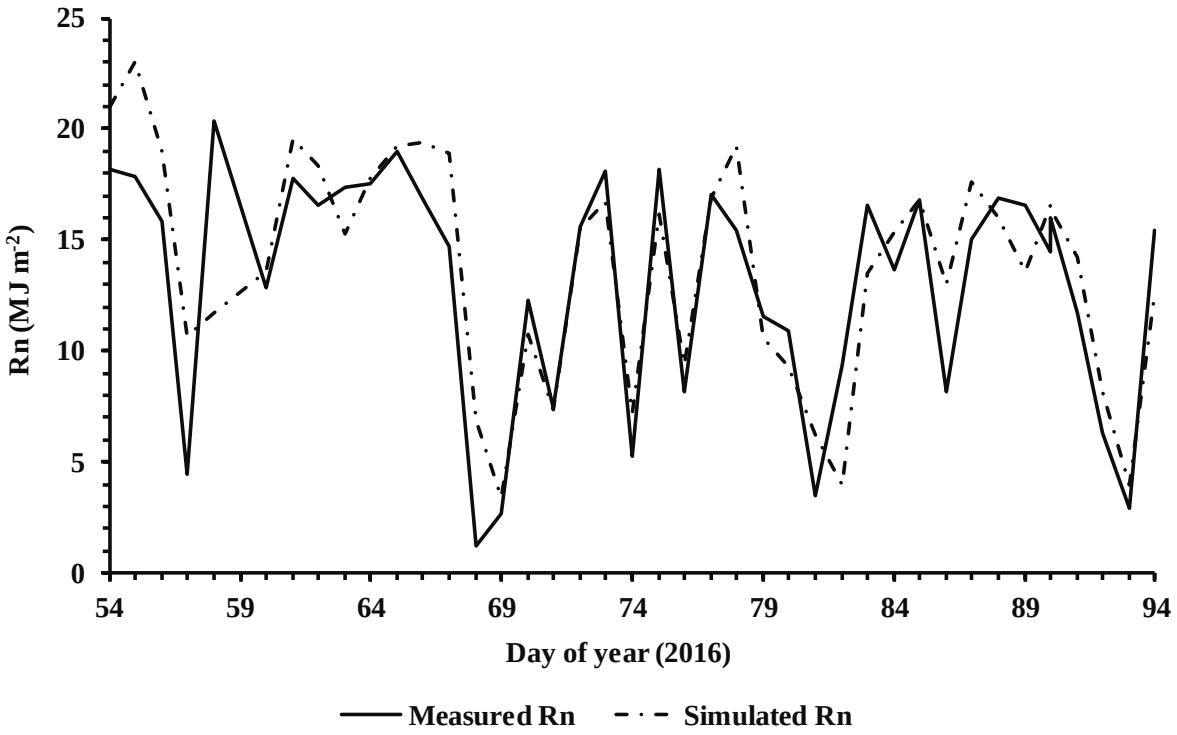


**Figure 4.32: The comparison between the daily measured and the simulated $R_n$ above open water at Midmar Dam from 24th February to 4th April 2016.**

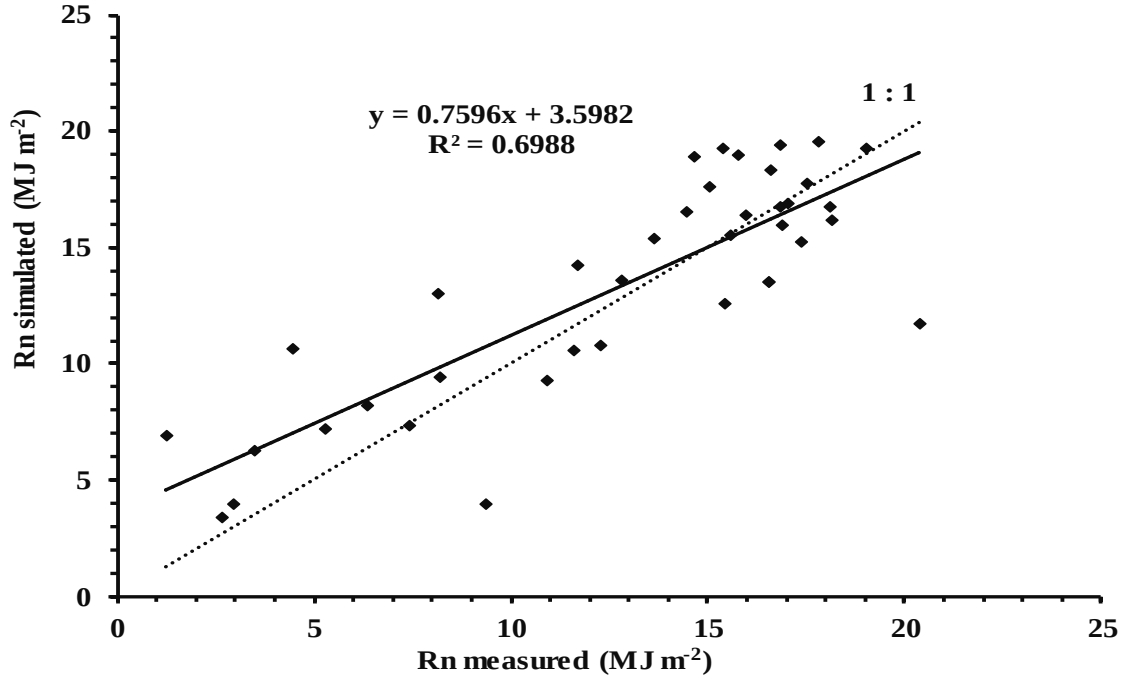


**Figure 4.33: The regression graph of the measured and the simulated $R_n$ above open water at Midmar Dam from 24th February to 4th April 2016.**

4.6.2.5 Overall discussion on modelling of the radiative fluxes at Midmar Dam

Major under-simulations of $R_n$ were observed during overcast days. For example, $R_{ne}$ was 11.75 MJ m$^{-2}$ compared to $R_n$ of 20.38 MJ m$^{-2}$ during the DOY 58 with 100 % relative humidity and minimal air temperature of 16.36 $^{o}$C, occurred just after DOY 57 with 6.35 mm of the daily total rainfall and daily total solar irradiance of 6.69 MJ m$^{-2}$. Furthermore, during the DOY 58, the estimated $L_d$ was 30.49 MJ m$^{-2}$ compared to the measured $L_d$ of 32.73 MJ m$^{-2}$. The under-simulation of $R_n$ during the overcast days is attributed to the under-simulation of $L_d$ due to poor estimation of cloud fraction within the DPMETHS model. The Brunt's formula used in the model to estimate $L_d$ was established only for clear-skies and may be not valid during the overcast days since clouds increase the atmospheric emissivity as also noted by Ortega-Farias (2000). Allan (2011) argue that although cloud fraction can be fairly estimated throughout the day in the model but lacks consistency (visual observations) since whether a given cloud will heat or cool the surface depends on the size of the cloud, the composition of the cloud and the cloud's altitude. Santos *et al.* (2011) also noted that $L_d$ was one of the most difficult components of the radiation balance to estimate. Furthermore, assuming a constant $r$ of 0.08 in the DPMETHS model during computation of $rR_s$ could have resulted in slight under-simulation of $R_n$ fluxes due to over-estimation of $rR_s$ which reduces $R_s$, as illustrated in Section 4.4.1.2 (b).

Major over-simulations of $R_n$ were observed during the days where there was greater contrast between the $SWT$ and $T_{air}$. For example, $R_{ne}$ was 18.92 MJ m$^{-2}$ compared to $R_n$ of 14.67 MJ m$^{-2}$ during the DOY 67 with daily-average $SWT$ of 23.9 $^{o}$C compared to $T_{air}$ of 18.8 $^{o}$C, the estimated $L_u$ was 39.62 MJ m$^{-2}$ compared to $R_n$ of 38.45 MJ m$^{-2}$. The DPMETHS model predicts $L_u$ based on the assumption that the $SWT$ is equal to the $T_{air}$. However, daily-average $T_{air}$ was observed to be less than $SWT$ (Figure 4.14). Alcântara *et al.* (2010) noted that the greater the contrast between the $SWT$ and $T_{air}$, the greater the $L_u$. The model over-simulated $R_n$ in days where the contrast between the $SWT$ and $T_{air}$ was larger due to under-simulated $L_u$ within the model. The DPMETHS model also uses $U_{land}$ as input, however, $U_{water}$ was observed to always be greater than $U_{land}$ (Figure 4.25). The DPMETHS model, a daily model, is dependent on the daily-averaged wind speed and therefore does not explicitly account for night-time $R_n$ which is dominated by $L_u$ that is directly governed by $SWT$. Higher wind speed at night-time than expected, could have resulted in surface cooling and decreased $SWT$.

Consequently, the model slight over-simulated $R_n$ due to under-simulations of $L_u$ during clear, windy days. For example, $R_{ne}$ was 10.67 MJ m$^{-2}$ compared to $R_n$ of 4.48 MJ m$^{-2}$ during the DOY 57 with daily-average $U_{water}$ of 23.9 $^{o}$C.

## 4.7 Modelling study at Stratus station, East Pacific Ocean

The DPMETHS model to estimate the available energy flux for open water evaporation is in its developmental stage and has not been used in any known study. Therefore, the estimates of the radiative flux from the DPMETHS model were tested for goodness of fit against measurements of the radiative flux from the ocean, under different climatic conditions. The ocean data used in this study were acquired at the Stratus station, located off the coast of Peru in South America in the Pacific Ocean. The constant reflection coefficient ($r$) of 0.08 was used to estimates of $rR_s$ from measurements of $R_s$ above the ocean surface. The estimates of $L_u$ from the ocean surface were computed from sea surface temperatures using Eq. 2.1. The daily estimates of the radiative fluxes for $R_s$, $L_d$, and $L_u$ were obtained by summing the hourly data for each day (01h00 to 24h00). Then, the daily $R_n$ of the ocean were computed using Eq. 2.3.

### *4.7.1 Modelling radiative fluxes at Stratus station, East Pacific Ocean*

The DPMETHS model was run for the eastern Pacific Ocean using meteorological daily data of solar irradiance, air temperature, relative humidity, wind speed, wind direction and rainfall measured over water at the ocean as well as the surface area and water depth of the ocean. To evaluate the performance of the DPMETHS model to simulate $R_n$ above the ocean, the comparisons were made between the daily estimates of the radiative fluxes predicted from the DPMETHS model and the daily radiative fluxes measured above water at the ocean.

#### 4.7.1.1 Incoming infrared irradiance

The comparisons between the daily estimates of $L_d$ predicted from the DPMETHS model and the daily $L_d$ measured above the ocean indicated reasonable agreement with both following the same variation (Figure 4.34). The smaller RMSE of 1.72 MJ m$^{-2}$ indicated the model simulates $L_d$ very well. However, the MBE of -1.40 MJ m$^{-2}$ indicated that the model often under-simulated $L_d$ although such a small value of MBE indicated a better model performance. The calculated t-statistic value of 9.3 which was greater than the critical t-value of 2.66 obtained

from the statistical tables indicated that the estimated $L_d$ and measured $L_d$ fluxes were statistically different at the 99.5 % level of confidence.

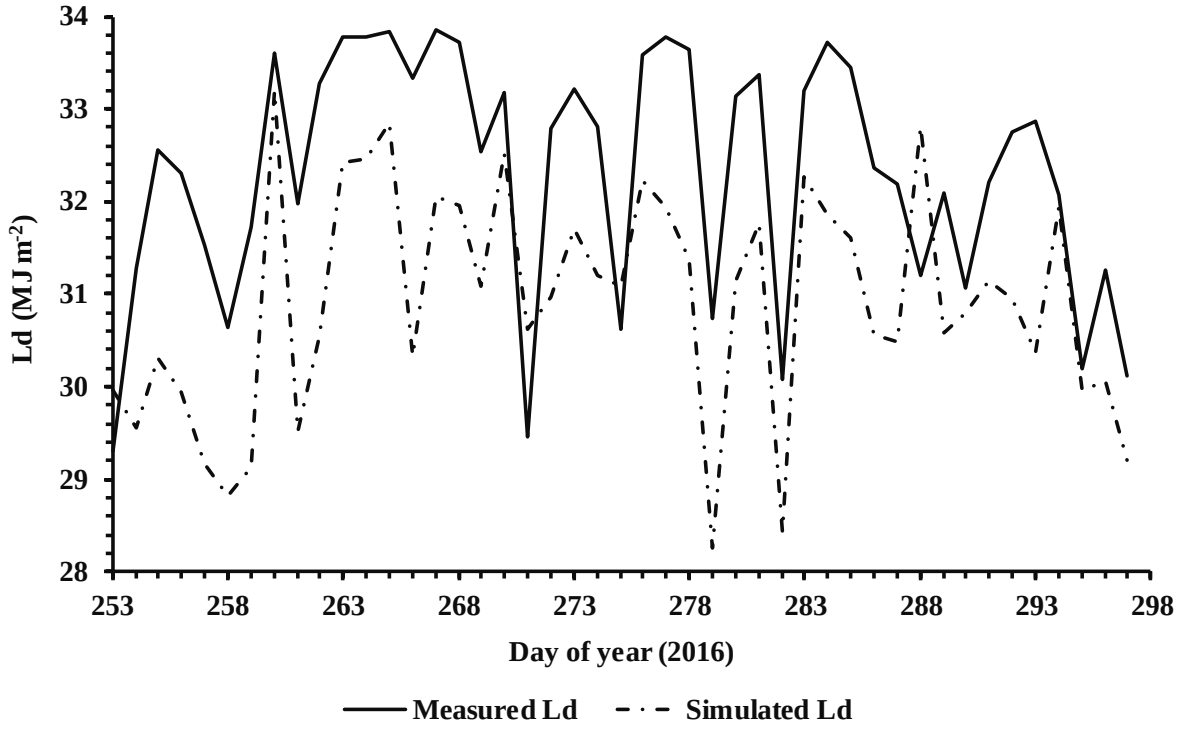


**Figure 4.34: The comparison between the daily measured and the simulated $L_d$ for the Stratus station of the East Pacific Ocean from 10th September to 24th October 2016.**

4.7.1.2 Net irradiance

The relationship between the daily estimates of the net irradiance ($R_{ne}$) predicted from the DPMETHS model and the daily net irradiance measured above water at the ocean ($R_n$) was good (Figure 4.35). The regression graph between $R_n$ and $R_{ne}$ indicated the statistically significant relationship between $R_n$ and $R_{ne}$, with $m$ approaching 0.62 and $r^2$ of 0.76 and intercept of 11.14 MJ m$^{-2}$ (Figure 4.36). The $r^2$ indicated that about 76 % variation in the $R_n$ can be explained by the $R_{ne}$. The RMSE of 5.67 MJ m$^{-2}$ indicated the model simulates $R_n$ very well. However, the MBE of 5.45 MJ m$^{-2}$ indicated that the model often over-simulated $R_n$ although such a small value of MBE indicated a better model performance. The calculated t-

statistic value indicated that $R_n$ and $R_{ne}$ fluxes were not statistically different at the 99.5 % level of confidence.

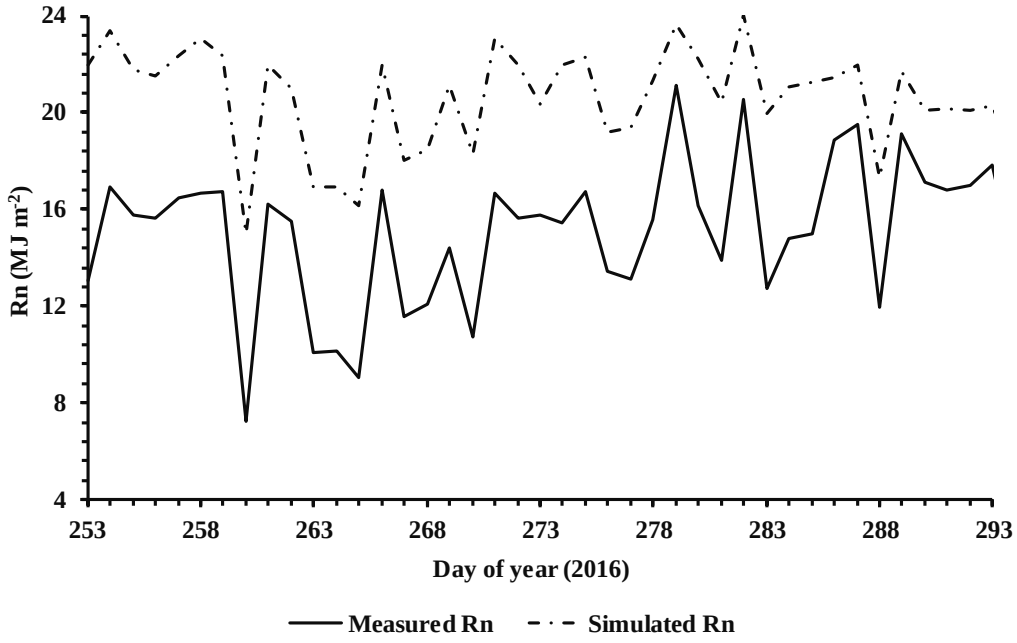


**Figure 4.35: The comparison between the daily measured and the simulated $R_n$ for the Stratus station of the East Pacific Ocean from 10th September to 24th October 2016.**

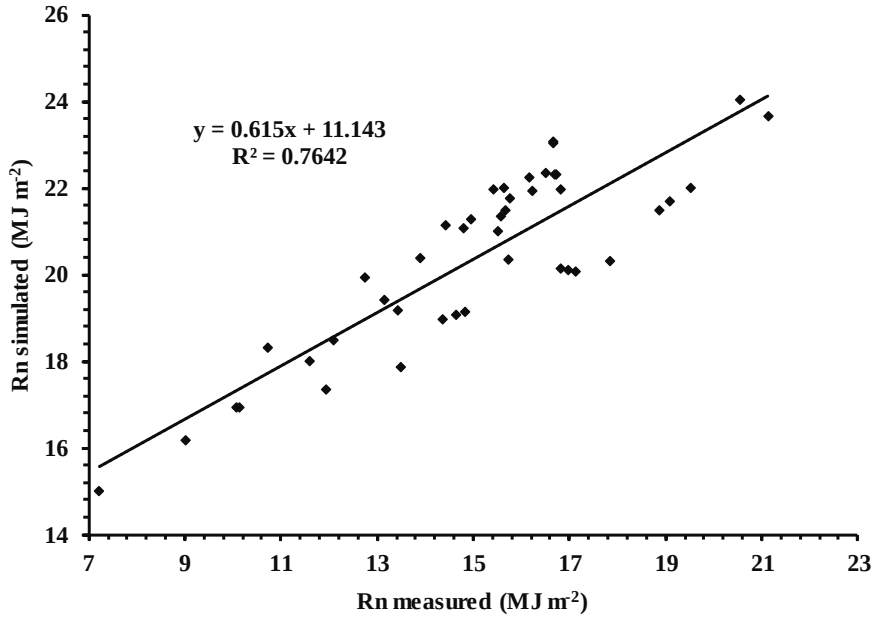


**Figure 4.36: The regression graph of the measured and the simulated $R_n$ for the Stratus station of the East Pacific Ocean from 10th September to 24th October 2016.**

### *4.7.2 Overall discussion on modelling of the radiative fluxes at Stratus ocean station*

Based on the results of the performance evaluation of the DPMETHS model presented above, it is suggested that the application of the DPMETHS model to estimate $R_n$ for open water evaporation is viable. The presence of the low, thick stratus clouds above the ocean, as noted by Nowak *et al.* (2008), emitted greater $L_d$ than expected. The observed poor estimation of $L_d$ within the DPMETHS model is attributed to the failure of the model to simulate the impacts of the low, thick stratus clouds above the ocean. The DPMETHS model only estimated the cloud fraction with no optical properties. However, whether the presence of clouds will have a net cooling or warming effect at the water surface depends on the cloud optical properties such as the cloud's altitude, its size, and the make-up of the particles that form the cloud (Key *et al.*, 1996). The DPMETHS model over-simulated $R_n$ during the entire study period at the ocean where daily data of the water depth and surface area were missing. Despite these problems associated with poor model input data, results produced are generally acceptable and it is believed that the DPMETHS model can be used to estimate $R_n$ for the ocean surface.

## 4.8 Potential impacts of climate change on the radiation balance of Midmar Dam

Climate change has already altered, and will continue to alter the different components of the hydrological cycle such as evaporation (IPCC, 2014). However, the impacts of climate change on evaporation are not yet fully understood given that different components of evaporation will be affected differently (CSIR, 2010). Furthermore, the lack of a long-term record of $R_n$ data over water surfaces hinders the evaluation of the potential impacts of climate change on the radiation balance which is one of the main drivers of evaporation. The availability of long-term meteorological dataset at Cedara station near Midmar Dam enables the unique opportunity to investigate the potential impacts of climate change on the radiation balance of Midmar Dam.

### *4.8.1 Long-term radiation balance of Midmar Dam*

To investigate the potential impacts of climate change on the radiation balance of Midmar Dam, the variation of long-term daily estimates of the radiative fluxes predicted from the DPMETHS model were evaluated. The variation in annual average daily $R_n$ ranged between 6.62 to 9.65 MJ $m^{-2}$ (Figure 4.37). Of particular note is the large increase in annual average daily $R_n$ by an average of 1.23 MJ $m^{-2}$ from year 2005 to 2015.

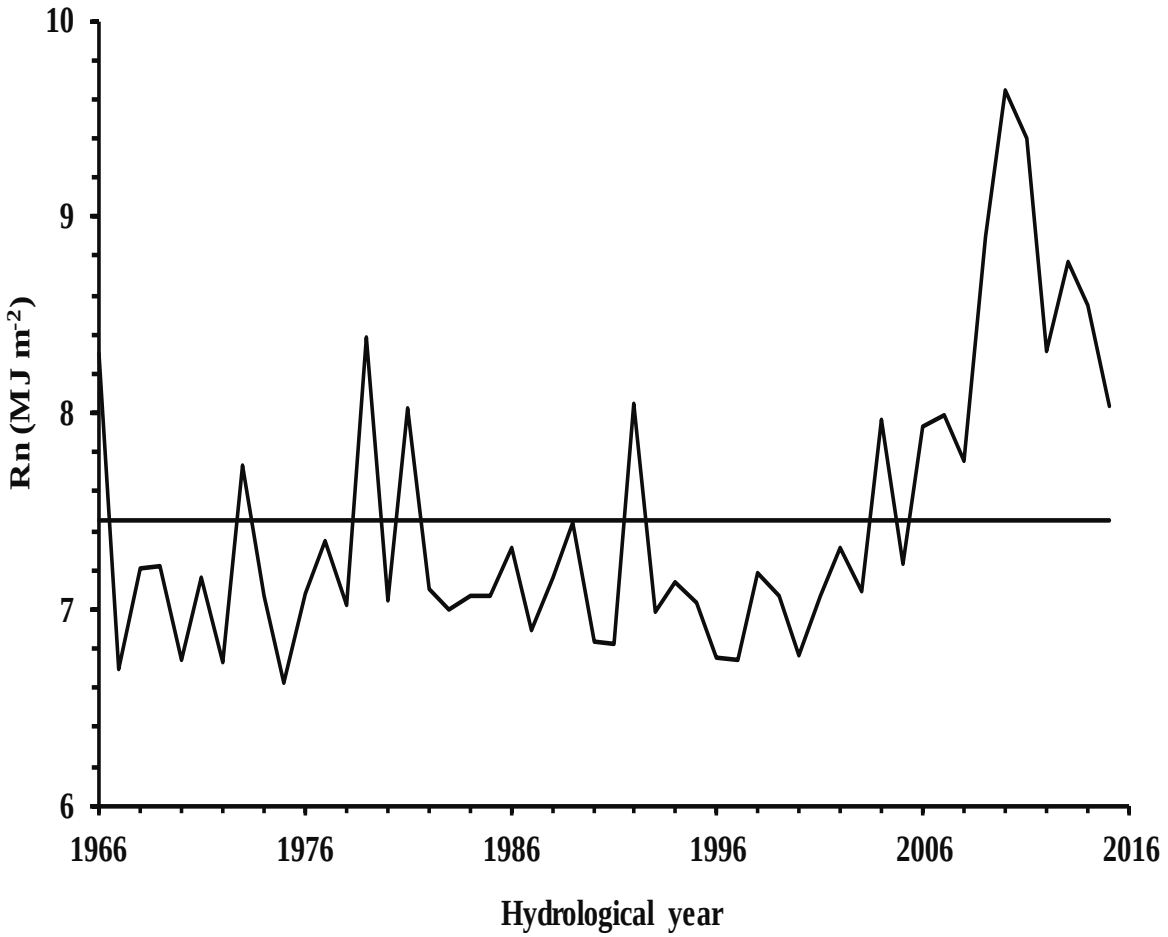


**Figure 4.37: Temporal variation in annual average daily $R_n$ for the period between year 1966 and 2015 (inclusively) at Midmar Dam.**

To investigate the possible cause of the increase in $R_n$ for this period, variation of annual average estimates of $R_s$, $L_u$, and $L_d$ were evaluated. The variation in the annual average daily $R_s$ indiciated that $R_s$ decreased by an average of 1.14 MJ m$^{-2}$ from year 2005 to 2015 (Figure 4.38). Therefore, the variation in annual average daily $R_s$ trend yielded no clue of the possible cause of the increase in $R_n$ between year 2005 and 2015. The variation in the annual average daily $L_u$ trend also yielded no clue of the possible cause of the increase in $R_n$ between year 2005 and 2015 (Figure 4.39). The variation in annual average daily $L_d$ indicated the large increase in $L_d$ by 0.49 MJ m$^{-2}$ per annum from year 2005 to 2015 (Figure 4.40). The large increases in $L_d$ is consistent with the increases in $R_n$ for the period between year 2005 and 2015.

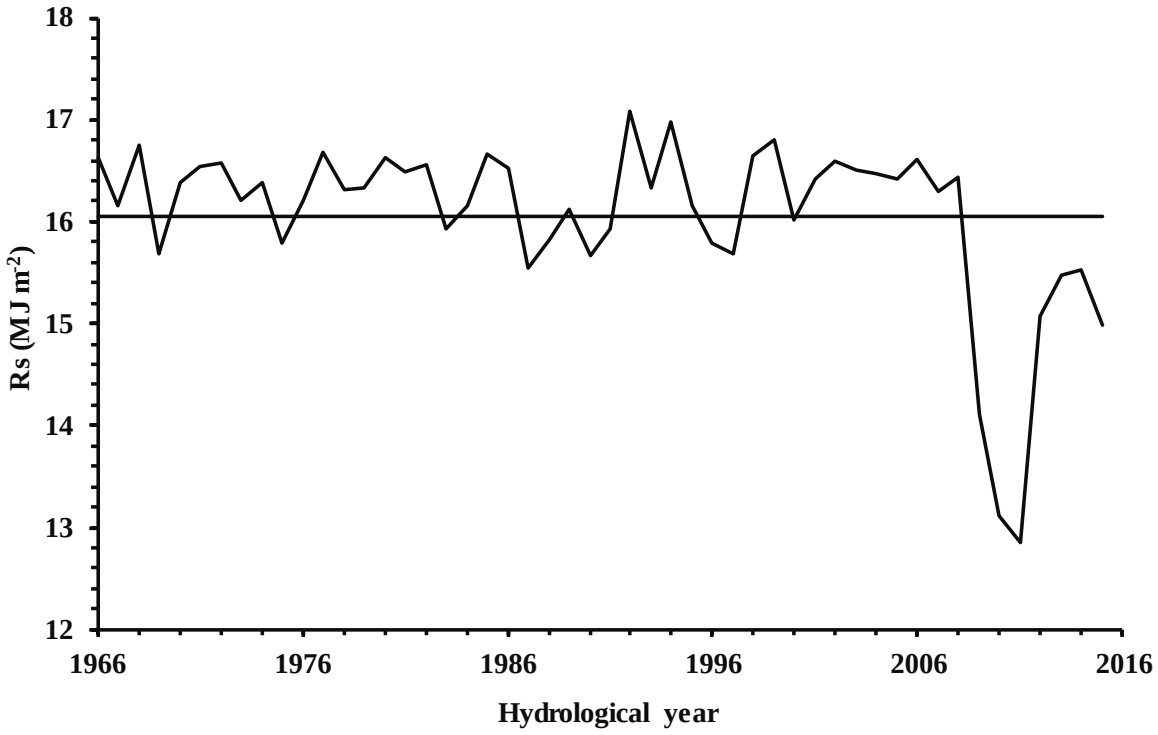


**Figure 4.38: Temporal variation in annual average daily $R_s$ for the period between year 1966 and 2015 (inclusively) at Midmar Dam.**

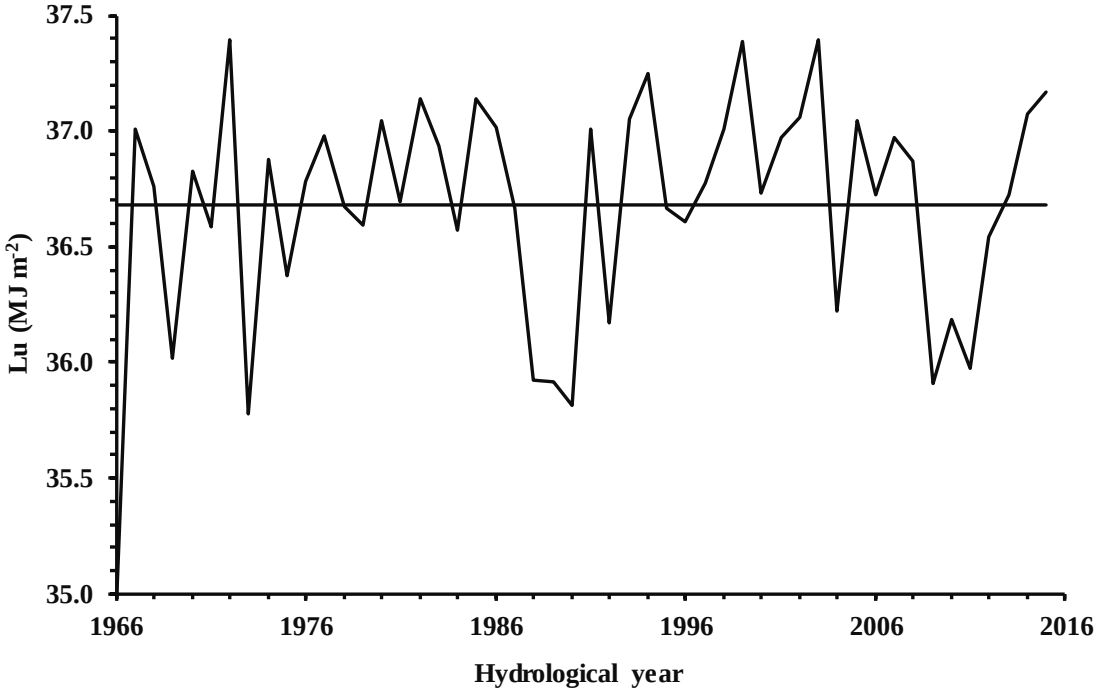


**Figure 4.39: Temporal variation in annual average daily $L_u$ for the period between year 1966 and 2015 (inclusively) at Midmar Dam.**

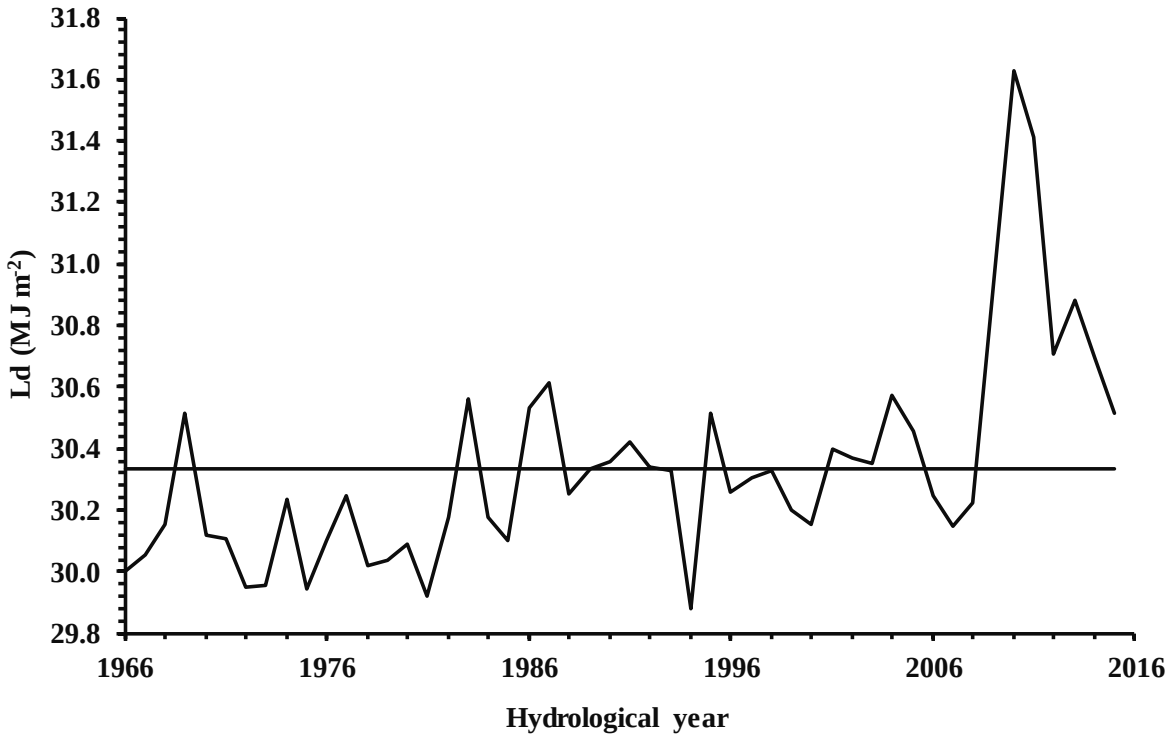


**Figure 4.40: Temporal variation in annual average daily $L_d$ for the period between year 1966 and 2015 (inclusively) at Midmar Dam.**

### *4.8.2 Overall discussion on the potential impacts of climate change on the radiation balance of Midmar Dam*

The large increase in $R_n$ from year 2005 to 2015 is attributed to the increase in $L_d$ for the same period. IPCC (2014) reported that the total carbon dioxide ($CO_2$) emissions have continued to increase over 1970 to 2010 with larger absolute increases between 2000 and 2010, despite a growing number of climate change mitigation policies. The increase in $L_d$ is consistent with the increase in total $CO_2$ emissions reported globally since $CO_2$ is a very strong absorber and emitter of infrared radiation. The presence of high concentrations of $CO_2$ in the atmosphere prevented most of $L_u$ from escaping into the space through the atmospheric window. The absorbed $L_u$ was then reradiated back to water surface as $L_d$ and resulted in an increase in $L_d$ which caused a change of the radiation balance. Consequently, the average air temperatures increased by an average of 0.36 $^oC$ per annum from year 2005 to 2015 (Figure 4.41). These findings are consistent with the observed increase in global average temperatures over the past 50 years due to the observed increase in anthropogenic greenhouse gas concentrations reported by IPCC (2014). However, the change in the radiation balance did not change the global average air

temperature instantaneously. Instead, the impacts of the changes in the radiation balance were felt more five years later where 2010 was the hottest year. The lag between when radiation imbalance occurs and when the impact on air temperature becomes fully apparent is mostly because of the large heat capacity of the global ocean. Consequently, the large amount of energy absorbed by the ocean for evaporation, partially buffers the global warming as a results of climate change as also noted by Ramanathan and Feng (2009).

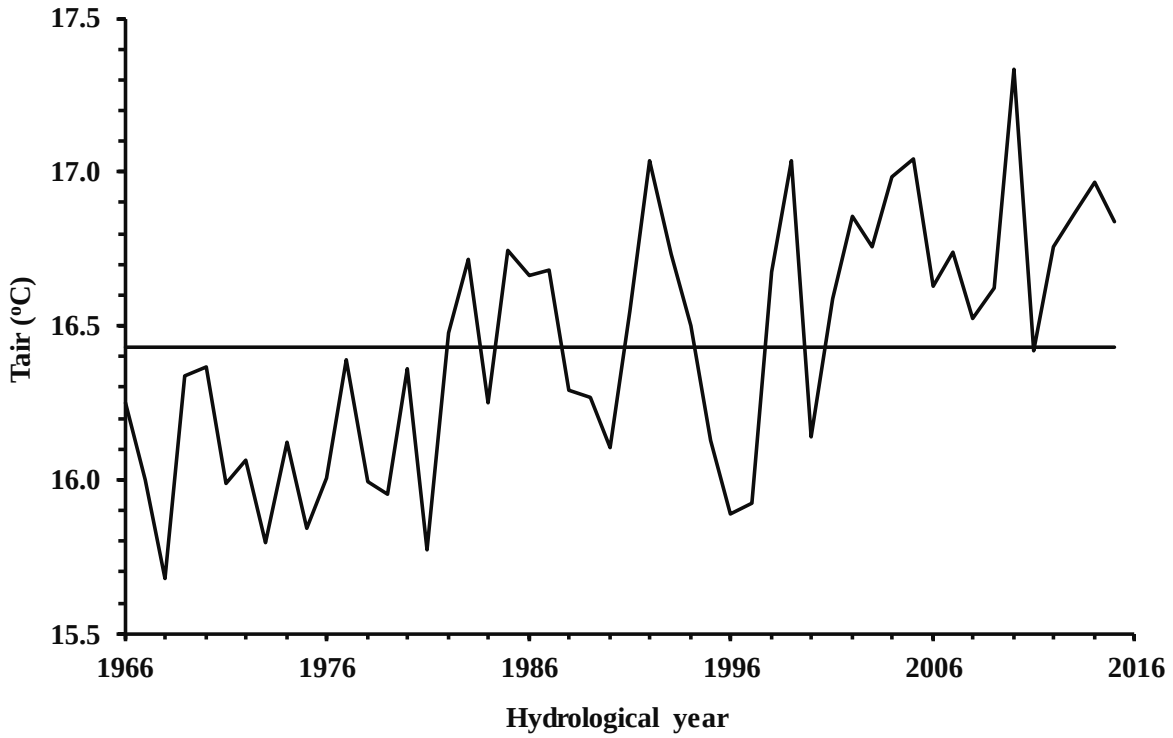


**Figure 4.41: Temporal variation in annual average daily air temperature for the period between year 1966 and 2015 (inclusively) at Midmar Dam.**

### *4.8.3 General comments*

This study showed evidence of the impacts of climate change on the radiation balance of Midmar Dam. Climate changes attributed to the increasing concentrations of $CO_2$ threaten to increase the long-term air temperatures of the earth with consequent increase in $R_n$ due to increases in $L_d$.

# CHAPTER 5 : CONCLUSIONS AND RECOMMENDATIONS FOR FURTHER RESEARCH

## 5.1 Introduction

The main aim of this study was to understand the factors enhancing temporal and spatial variability of the radiation balance at water storage and to evaluate the performance of the DPMETHS model to simulate available energy flux above open water at Midmar Dam and for an eastern Pacific Ocean site. The objectives of the research were:

- To improve an understanding of the variability of the radiation balance and available energy above open water storage and assessing the factors that affect the radiation balance above open water;
- To evaluate the performance of the DPMETHS model to simulate the daily available energy flux at Midmar Dam and at the ocean Pacific Ocean;
- To investigate the potential impacts of climate change on the radiation balance of Midmar Dam.

## 5.2 Findings

The cloud cover, reflection coefficient of water ($r$), air temperature ($T_{air}$) and surface water temperature ($SWT$) were the main factors that control the temporal and spatial variability of radiation balance above open water surface. The net irradiance ($R_n$) fluxes were minimal during an overcast day compared to a clear-sky day and this indicated that clouds had an average cooling effect on the water surface of Midmar Dam. The $r$ directly determined the amount of the incoming solar irradiance ($R_s$) absorbed by the water surface and a turbid water body reflected more $R_s$. The observed $r$ values showed the strong diurnal variation and there was high water reflectivity at lower sun's angles. For the entire study period, daily $r$ ranged between 0.05 and 0.14 and the daily-average $r$ of 0.08 was observed. The $SWT$ controls the outgoing infrared irradiance ($L_u$) while $T_{air}$ affects water vapour pressure which controls the incoming infrared irradiance ($L_d$). Minimum $T_{air}$ and $SWT$ values were observed just before the sunrise while maximum temperatures were observed during the late afternoon. However, during the daytime, $T_{air}$ was greater than $SWT$ while during the night-time the observations were inverted.

The range in diurnal $SWT$ measurements was less than that for $T_{air}$ due to greater specific heat capacity of water compared to air. The spatial variation of $R_n$ above open water is mainly due to the spatial variability in $SWT$ since with constant emissivity, $L_u$ depends on $SWT$ alone. The *in-situ* measurement of $SWT$ compared well to the Landsat-8 estimate of $SWT$. Water near the shore responded to the atmospheric conditions very quickly compared to the offshore water. Consequently, water near the shore was observed to always be warmer than offshore water by an average of 1.5 $^{o}$C. Furthermore, shallow parts of the dam were 2 $^{o}$C warmer than the deeper part of Midmar Dam. The observed average of 1.5 to 2 $^{o}$C variability of $SWT$ across Midmar Dam implies the very low spatial variability of $L_u$ which is temperature dependent. Therefore, the low spatial variability of $SWT$ is associated with low spatial variation of $R_n$ across the dam. The spatial variability of $SWT$ across the dam indicated that point measurements of $SWT$ are reasonable indicators of the reservoir $SWT$ which is used to compute the water-stored heat flux ($G$) and $L_u$ from the water surface at Midmar Dam.

The $R_n$ was the dominant component of the available energy flux over water surface at Midmar Dam. During daytime, $R_n$ fluxes were positive, corresponding to a source of energy while during night-time, $R_n$ fluxes were negative, corresponding to a loss of energy from the water surface. The variability of the available energy flux at water storage indicated that $G$ showed a similar diurnal variation to $R_n$ with comparable magnitudes and peaked at the same time as the peak in $R_n$. For the entire study period, the temporal variability of $G$ showed that during some days, heat was stored in water storage ($G > 0$ W m$^{-2}$) while during other days, heat was released from water storage ($G < 0$ W m$^{-2}$). Therefore, $G$ plays a significant role in the daily energy balance and cannot be neglected for accurate estimation of the daily open water evaporation. Even with using a running mean, estimates of $G$ often showed very wide variation due to turbulent water waves of varying temperature travelling past the thermocouples. Consequently, estimates of $G$ fluxes of Midmar Dam showed a very wide variation that was not attributed to variation in $R_n$ and were unreliable.

This study showed that daily $R_n$ can be simulated well from standard weather station data using the DPMETHS model at Midmar Dam. The under-simulation of $R_n$ during overcast days were attributed to under-simulation of $L_d$ due to poor estimation of cloud fraction using the Brunt's

formula that was established only for clear-skies. Furthermore, assuming a constant $r$ of 0.08 in the DPMETHS model during computation of $rR_s$ resulted in slight under-simulation of $R_n$ fluxes due to over-estimation of $rR_s$ which reduces $R_n$. The relative lack of validity of the assumption that the $SWT$ is equal to the $T_{air}$ together with the use of wind speed measured at the land-based station which was less than the wind speed at water surface as a model inputs resulted in the model under-simulating $L_u$ which resulted on the over-simulation of $R_n$ on some of the days. The presence of the low, thick stratus clouds above the ocean emitted greater $L_d$ than expected and resulted on the poor simulations of $L_d$ for Stratus station at eastern Pacific Ocean. Despite the problems associated with poor model input data, results produced are generally acceptable and it is believed that the DPMETHS model can be used to estimate $R_n$ for the ocean surface.

This study showed evidence of the impacts of climate change on the radiation balance of Midmar Dam. Climate changes attributed to the global increase in the concentrations of total carbon dioxide threaten to increase the long-term air temperatures of the earth with consequent increase in $R_n$ due to increases in $L_d$.

### 5.3 Challenges and recommendations for future research

Despite the free availability of the Landsat-8 data which provide synoptic and frequent acquisition of data over large areas, remote sensing is at its developmental stage and satellite-derived $SWT$ need to be calibrated with ground truth $SWT$ data which is not readily available at Midmar Dam. The main limitation of Landsat-8 is that satellites acquire data once in every 16 days at any given location and does not record data at night. Furthermore, satellites acquire data at local time 09h50, where the main factors driving $SWT$ are minimal and images collected with cloud fraction of more than 60 % are discarded. Consequently, Landsat-8 data are not reliable representations of the temporal variability of daily $SWT$. The thermal infrared data from Landsat-8 is corrected for the solar elevation and atmospheric emissivity for quantitative assessment of $SWT$ using empirical equations which introduce uncertainties in derived estimates of $SWT$. Only one Landsat-8 image was used in this study to assess spatial variability of $SWT$. It is recommended that in future studies on such large dams, more cloudless Landsat-

8 images should be collected and compared with *in-situ* measurements of $SWT$ from stations installed permanently across the dam to represent the variability in $SWT$ observed in this study.

This study showed that $R_n$ can be simulated well from standard weather station data using the DPMETHS model. The DPMETHS model performed successfully on the Midmar Dam study and to a lesser extent at the ocean with stratus clouds and missing daily data of the water depth. The estimation of the cloud fraction within the DPMETHS model needs to be modified to account for optical cloud properties. This is because whether the presence of clouds will have a net cooling or warming effect at the water surface depends on the cloud optical properties such as cloud's altitude, its size, and the make-up of the particles. The limitations of the DPMETHS model is that it is complex and requires dam characteristics such as water depth and surface area which may be not readily available at the dam of interest. Furthermore, the lack of a long-term record of $R_n$ data over water surface hindered the evaluation of the DPMETHS model to simulate seasonal variability of $R_n$. In future studies, the DPMETHS model should be validated in different water storages of different sizes representing the wide range of climatic conditions across all regions. Furthermore, a better and reliable method of measuring or estimating $G$ is required since $G$ fluxes were measured with great difficulty using thermocouples. Consequently, model estimates of $G$ were not compared to unreliable measurements of $G$ in this study. The lack of reliable measurements of $G$ limited the evaluation of the DPMETHS model to compute $G$ from land-based meteorological data. One of the limitations of the DPMETHS model is that the model utilizes the daily meteorological data which might not be a true representation of climatic conditions for the entire day, since most of the model inputs demonstrated a wide range of diurnal variability. For future research, it is recommended that a sub-daily model that also estimates available energy flux for open water evaporation based on land-based meteorological data is used for similar studies for improved estimates of available energy flux.

### 5.4 Final comments and summary

The DPMETHS model is a new and promising method for estimating the daily available energy flux for daily open water evaporation using readily available meteorological data. Consequently, the DPMETHS model can reduce the costs of estimating open water evaporation using the energy balance techniques by eliminating the need for measuring the net irradiance

with greater difficulty using the expensive net radiometers mounted above water. The lack of the long-term records of available energy flux data collected over water will still limit the evaluation and verification of the DPMETHS model in different water storages of different sizes across different climatic conditions. Therefore, more data need to be collected above water using permanent stations for extended periods.

# CHAPTER 6 : REFERENCES


Alcântara EHD, Stech JL, Lorenzzetti JA, Bonnet MP, Casamitjana X, Assireu AT, de Moraes Novo EML. 2010. Remote sensing of water surface temperature and heat flux over a tropical hydroelectric reservoir. Remote Sensing of Environment 114(11): 2651-2665.

Alcântara EHD, Stech JL, Lorenzzetti JA, Novo EML. 2011. Time series analysis of water surface temperature and heat flux components in the Itumbiara Reservoir (GO), Brazil. Acta Limnologica Brasiliensia 23(3): 245-259.

Allan RP. 2011. Combining satellite data and models to estimate cloud radiative effect at the surface and in the atmosphere. Meteorological Applications 18(3): 324-333.

Allen RG, Pereira LS, Raes D, Smith M. 1998. Crop Evapotranspiration-Guidelines for computing crop water requirements-FAO Irrigation and drainage paper 56. FAO, Rome 300(9): D05109. Available at: http://s3.amazonaws.com/academia.edu.documents/40878584/Allen_FAO1998.pdf?AWSAccessKeyId=AKIAJ56TQJRTWSMTNPEA&Expires=1477267084&Signature=hzg2Jt%2FGGQSPf7i5GDYFBCM8DyU%3D&response-content-disposition=inline%3B%20filename%3DAllen_FAO1998.pdf [Accessed 3 March 2015].

Arya PS. 2001. Introduction to micrometeorology (Vol. 79). Academic Press. New York, USA.

Blonquist JM, Allen RG, Bugbee B. 2010. An evaluation of the net radiation sub-model in the ASCE standardized reference evapotranspiration equation: implications for evapontransipiration prediction. Agricultural Water Management 97: 1026–1038.

Brotzge JA, Duchon CE. 2000. A field comparison among a domeless net radiometer, two four-component net radiometers, and a domed net radiometer. Journal of Atmospheric and Oceanic Technology 17(12): 1569-1582.

Brunt D. 1934. Physical and Dynamical Meteorology. Cambridge University Press.UK

Brutsaert W. 1982. Evaporation into the Atmosphere, Reidel Publishing Company, Dordrecht, Holland.

Brutsaert W. 2013. Evaporation into the atmosphere: theory, history and applications (Vol. 1). Springer Science & Business Media. New York, USA.

CSIR. 2010. A CSIR perspective on water in South Africa-2010. CSIR Report No. CSIR/NRE/PW/IR/2011/0012/A. Available at: http://www.csir.co.za/nre/docs/CSIR%20Perspective%20on%20Water_2010.PDF [Accessed 25 February 2015].

de Bruin HAR. 1982. Temperature and energy balance of a water reservoir determined from standard weather data of a land station. Journal of Hydrology 593: 261–274.

Department of Water Affairs and Forestry. 2007. Information on South African dams. Hydrological Services, Department of Water Affairs and Forestry. South Africa. Available on http://www.dwaf.gov.za/hydrology/dwafapp2_wma/ [Accessed 6 March 2015].

Dong A, Grattan SR, Carroll JJ, Prashar CRK. 1992. Estimation of daytime net radiation over well-watered grass. Journal of Irrigation and Drainage Engineering 118(3): 466-479.

Dozier J. 1980. A clear-sky spectral solar radiation model for snow-covered mountainous terrain. Water Resources Research 16 (4): 709-718.

Duan Z. 2014. Estimating water balance components of lakes and reservoirs using various open access satellite databases. PhD thesis, Delft University of Technology, The Netherlands.

DWAF. 2013. National Water Resource Strategy: Water for an Equitable and Sustainable Future. Department of Water Affairs Pretoria, South Africa. Available at: https://www.dwa.gov.za/nwrs/LinkClick.aspx?fileticket=CIwWyptzLRk%3D&tabid=91&mid=496 [Accessed 14 March 2016].

Edinger JE, Duttweiler DW, Geyer JC. 1968. The response of water temperatures to meteorological conditions. Water Resources Research 45: 1137–1143.

Everson CS. 1999. Evaporation from the Orange River: quantifying open water resources. Water Research Commission. Report No.683/1/99. Available at: http://www.wrc.org.za/Knowledge%20Hub%20Documents/Research%20Reports/683-1-99.pdf [Accessed 23 February 2015].

Federer CA. 1968. Spatial variation of net radiation, albedo and surface temperature of forests. Journal of Applied Meteorology 7(5): 789-795.

Finch J, Hall R. 2001. Estimation of open water evaporation. A review of methods. Environment Agency. Bristol, UK.

Finch JW, Calver A. 2008. Methods for the quantification of evaporation from lakes. Available at: http://nora.nerc.ac.uk/14359/1/wmoevap_271008.pdf [Accessed 4 March 2015].

Finch JW, Gash JHC. 2002. Application of a simple finite temperature difference model for estimating evaporation from open water. Journal of Hydrology 255: 252–259.

Finch JW. 2001. A comparison between measured and modelled open water evaporation from a reservoir in south-east England. Hydrological Processes 1514: 2771–2778.

Fraederich K, Erath BG, Weber G. 1977. A simple model for estimating the evaporation from a shallow water reservoir. Tellus 29: 424-434.

Gates DM. 1980. Longwave and total radiation. In Biophysical Ecology (pp. 148-180). Springer New York, USA.

Geraldo-Ferreira E, Soria-Olivas J, Gómez-Sanchis AJ, Serrano-López A, Velázquez-Blazquez A, López-Baeza E. 2011. Modelling net radiation at surface using ‘‘*in-situ*” netpyrradiometer measurements with artificial neural networks. Expert Systems with Applications 38(11): 14190-14195.

Granger RJ, Hedstrom N. 2011. Modelling hourly rates of evaporation from small lakes. Hydrology and Earth System Sciences 15(1): 267-277.

Hargreaves GH, Samani ZA. 1982. Estimation of potential evapotranspiration. Journal of Irrigation and Drainage Division, Proceedings of the American Society of Civil Engineers 108: 223-230.

Hatzianastassiou N, Vardavas I. 2001. Shortwave radiation Budget of the Southern Hemisphere using ISCCP C2 and NCEP-NCAR climatological data. Journal of climate.14(22): 4319-29.

Henderson-Sellers B. 1986. Calculating the surface energy balance for lake and reservoir modeling: A review. Reviews of Geophysics 24(3): 625-649.

Howell JR, Menguc MP, Siegel R. 2010. Thermal radiation heat transfer. CRC Press. USA.

Huntington JL, McEvoy D. 2011. Climatological estimates of open water evaporation from selected Truckee and Carson River basin water bodies, California and Nevada. Desert Research Institute. Available at: http://www.dri.edu/images/stories/divisions/dhs/dhsfaculty/JustinHuntington/Huntington_an__McEvoy_2011.pdf [Accessed 25 May 2015].

IPCC. 2014: Climate Change 2014: Synthesis Report. Contribution of Working Groups I, II and III to the Fifth Assessment Report of the Intergovernmental Panel on Climate Change [Core Writing Team, R.K. Pachauri and L.A. Meyer (eds.)]. IPCC, Geneva,

Switzerland, 151 pp. Available at: https://www.ipcc.ch/pdf/assessment-report/ar5/syr/SYR_AR5_FINAL_full.pdf [Accessed 28 April 2015].

Iziomon MG, Mayer H, Matzarakis A. 2000. Empirical models for estimating net radiative flux: A case study for three mid-latitude sites with orographic variability. Astrophysics and Space Science 273(4): 313-330.

Jacobs AF, Heusinkveld BG, Kraai A, Paaijmans KP. 2008. Diurnal temperature fluctuations in an artificial small shallow water body. International Journal of Biometeorology 52(4): 271-280.

Jensen ME. 2010. Estimating evaporation from water surfaces. In: Proceedings of the CSU/ARS Evapotranspiration Workshop (Vol. 15). Available at: http://ccc.atmos.colostate.edu/ET_Workshop/ET_Jensen/ET_water_surf.pdf [Accessed 2 March 2015].

Keijman J, Koopmans R. 1973. A comparison of several methods of estimating the evaporation of Lake Flevo, Proc. IAHS (Helsinki) Symposium on Hydrology of Lakes pp. 225–232.

Key JR, Silcox RA, Stone RS. 1996. Evaluation of surface radiative flux parameterizations for use in sea ice models. Journal of Geophysical Research: Oceans 101(2): 3839-3849.

Kipp & Zonen, Delft, Netherlands, 2014. Instruction manual: CNR4 net radiometer. Kipp & Zonen, Delft, Netherlands.

Koberg GE. 1964. Methods to compute long-wave radiation from the atmosphere and reflected solar radiation from a water surface. US Government Printing Office pp. 107-136. Available at: http://pubs.usgs.gov/pp/0272f/report.pdf [Accessed 12 March 2015].

Kristovich DA, Laird NF. 1998. Observations of widespread lake-effect cloudiness: Influences of lake surface temperature and upwind conditions. Weather and Forecasting 13(3): 811-21.

Lamaro AA, Mariñelarena A, Torrusio SE, Sala SE. 2013. Water surface temperature estimation from Landsat 7 ETM+ thermal infrared data using the generalized single-channel method: Case study of Embalse del Río Tercero (Córdoba, Argentina). Advances in Space Research 51(3): 492-500.

Li ZL, Tang BH, Wu H, Ren H, Yan G, Wan Z, Sobrino JA. 2013. Satellite-derived land surface temperature: Current status and perspectives. Remote Sensing of Environment 131: 14-37.

Liou KN. 2002. An introduction to atmospheric radiation (Vol. 84). Academic Press. Canada.

Liu WT. 1993. Evaporation from the ocean (Vol. 265). Cambridge University Press. UK.

Lorenzzetti JA, Araújo CAS, Curtarelli MP. 2015. Mean diel variability of surface energy fluxes over Manso Reservoir. Inland Waters (2): 155-172.

Mahmud AA, Baten MA, Khan MB, Miyata A. 2015. Diurnal pattern of energy fluxes over rice field. Journal of Environmental Science and Natural Resources 6(1): 1-6.

McCuen RH, Asmussen LE. 1973. Estimating the effect of heat storage on evaporation rates. Hydrological Sciences Journal 18(2): 191-196.

McJannet DL, Cook FJ, Burn S. 2013. Comparison of techniques for estimating evaporation from an irrigation water storage. Water Resources Research 49(3): 1415-1428.

McJannet DL, Webster I, Stenson M, Sherman B. 2008. Estimating open water evaporation for the Murray-Darling Basin: A report to the Australian Government from the CSIRO Murray-Darling Basin Sustainable Yields Project. CSIRO, Australia. Available at: https://publications.csiro.au/rpr/download?pid=procite:0921ff52-a841-4574-b599-5f28a8716783&dsid=DS1 [Accessed 13 February 2015].

McKenzie RS, Craig AR. 2001. Evaluation of river losses from the Orange River using hydraulic modelling. Journal of Hydrology 241: 62-69.

McMahon TA, Peel MC, Lowe L, Srikanthan R, McVicar TR. 2013. Estimating actual, potential, reference crop and pan evaporation using standard meteorological data: a pragmatic synthesis. Hydrology and Earth System Sciences 17(4): 1331-1363.

Mengistu MG, Savage MJ. 2010. Open water evaporation estimation for a small shallow reservoir in winter using surface renewal. Journal of Hydrology 380(1): 27-35.

Monteith JL. 1965. Evaporation and the environment. In Symposia of the society for experimental biology 19: 205-234.

Mukheibir P, Sparks D. 2003. Water resource management and climate change in South Africa: visions, driving factors and sustainable development indicators. Report for Phase I of the Sustainable Development and Climate Change project. Energy and Development Research Centre (EDRC), University of Cape Town. Available at: http://idprc.org/wp-content/uploads/2015/08/Water_resource_management-in-Southern-Africa.pdf [Accessed 23 February 2015].

Mukheibir P. 2007. The impact of climate change on small municipal water resource management: The case of Bredasdorp, South Africa. Available at: https://open.uct.ac.za/handle/11427/17197 [ Accessed 20 February 2015].

Nowak D. Vuilleumier L, Ohmura A. 2008. Radiation transfer in stratus clouds at the BSRN Payerne site. Atmospheric Chemistry and Physics Discussions 8(3): 11453-11485.

Ohring G, Clapp P. 1980. The effect of changes in cloud amount on the net radiation at the top of the atmosphere. Journal of the Atmospheric Sciences 37(2): 447-454.

Page JK, Rodgers GG, Souster CG, Le Sage SA. 1979. Predetermination of irradiation on inclined surfaces for different European centres. Final Report, Vol. 2, EEC Solar Energy Programme, Project F, Sheffield. Sheffield. Available at: http://www.osti.gov/scitech/biblio/7035353 [Accessed 17 March 2015].

Ramanathan V, Barkstrom BR, Harrison EF. 1989. Climate and the Earth's radiation budget. International Agrophysics 5(3-4): 171-181.

Ramanathan V, Feng Y. 2009. Air pollution, greenhouse gases and climate change: Global and regional perspectives. Atmospheric Environment 43:37-50.

Rozenstein O, Qin Z, Derimian Y, Karnieli A. 2014. Derivation of land surface temperature for Landsat-8 TIRS using a split window algorithm. Sensors 14(4): 5768-5780.

Santos CACD, Silva BBD, Rao TVR, Satyamurty P, Manzi AO. 2011. Downward longwave radiation estimates for clear-sky conditions over northeast Brazil. Revista Brasileira de Meteorologia 26(3): 443-450.

Savage MJ, Abraha MG, Moyo NC, Babikir ESN. 2014. Web-based teaching, learning and research using accessible real-time data obtained from field-based agrometeorological measurement systems. South African Journal of Plant and Soil 33(1): 13-23.

Savage MJ, Everson CS, Odhiambo GO, Mengistu MG, Jarmain C. 2004. Theory and practice of evaporation measurement, with special focus on surface layer scintillometry as an operational tool for the estimation of spatially averaged evaporation. Water Research Commission Report No. 1335/1/04, p204, ISBN 1-77005-247-X. Available at: http://www.wrc.org.za/Knowledge%20Hub%20Documents/Research%20Reports/1335-1-04.pdf [Accessed 23 March 2015].

Savage MJ, Heilman JL. 2009. Infrared calibration of net radiometers and infrared thermometers. Agricultural and Forest Meteorology 149: 1279-1293.

Savage MJ, Pasi JM, Myeni L, Clulow AD. 2016. Open water evaporation measurement using micrometeorological methods. Unpublished Water Research Commission Report No. K5/2335.

Savage MJ. 2010. Sensible heat flux for estimating evaporation. D.Sc.Agric. thesis, University of KwaZulu Natal, Pietermaritzburg, South Africa.

Savage MJ. 2012. Agrometeorology and environmental biophysics. Unpublished lecture notes, AMET210P1, University of KwaZulu-Natal, Pietermaritzburg, South Africa.

Schott JR., Barsi JA, Nordgren BL, Raqueno NG, de Alwis D. 2001. Calibration of Landsat thermal data and application to water resource studies. Remote Sensing of Environment 78(1): 108-117.

Schulze RE. 2011. Approaches towards practical adaptive management options for selected water-related sectors in South Africa in a context of climate change. Water SA 37(5): 621-646.

Sima S, Ahmadalipour A, Tajrishy M. 2013. Mapping surface temperature in a hyper-saline lake and investigating the effect of temperature distribution on the lake evaporation. Remote Sensing of Environment 136: 374-385.

Simpson D, Dickens C. 2006. Potential water quality impacts on Midmar Dam from the proposed Khayelisha social housing project. Institute of Natural Resources, Gauteng, South Africa. Available at: http://rava.qsens.net/themes/water_template/mgeni-catchment/Proposed%20Khayelisha%20housing%20project.pdf/at_download/file [Accessed 16 March 2015].

Sinclair TR, Shiraiwa T, Hammer GL. 1992. Variation in crop radiation-use efficiency with increased diffuse radiation. Crop Science 32(5): 1281-1284.

Steissberg TE, Hook SJ, Schladow SG. 2005. Characterizing partial upwellings and surface circulation at Lake Tahoe, California–Nevada, USA with thermal infrared images. Remote Sensing of Environment 99(1): 2-15.

Swancar A. 2015. Comparison of evaporation at two central Florida lakes, April 2005-November 2007 (No. 2015-1075). US Geological Survey. Available at: https://pubs.usgs.gov/of/2015/1075/ofr20151075.pdf [Accessed 8 June 2016].

Tanny J, Cohen S, Assouline S, Lange F, Grava A, Berger D, Teltch B, and Parlange MB. 2008. Evaporation from a small water reservoir: Direct measurements and estimates. Journal of Hydrology 351(1-2): 218-229.

Timofeyev YM, Vasil′ev AV. 2008. Theoretical Fundamentals of Atmospheric Optics. Cambridge Int Science Publishing. UK.

United States Geological Survey. 2013. Using the USGS Landsat 8 Product. Available at: http://landsat.usgs.gov/Landsat8_Using_Product.php [Accessed 3 May 2016].

Valiantzas JD. 2006. Simplified versions for the Penman evaporation equation using routine weather data. Journal of Hydrology 331(3): 690-702.

van Dijk M, van Vuuren SJ. 2009. Destratification induced by bubble plumes as a means to reduce evaporation from open impoundments. Water SA 35:158–167.

Walpole RE, Myers RH. 1989. Probability and Statistics for Engineers and Scientists. 4th Edn., Macmillan. UK.

Wang K, Liang S. 2009. Estimation of daytime net radiation from shortwave radiation measurements and meteorological observations. Journal of Applied Meteorology and Climatology 48(3): 634-643.

Wang W, Xiao W, Cao C, Gao Z, Hu Z, Liu S, Shen S, Wang L, Xiao Q, Xu J, Yang D, Lee X. 2014. Temporal and spatial variations in radiation and energy balance across a large freshwater lake in China. Journal of Hydrology 511: 811-824.

Winter TC, Buso DC, Rosenberry DO, Likens GE, Sturrock JrA, Mau DP. 2003. Evaporation determined by the energy-budget method for Mirror Lake, New Hampshire. Limnology and Oceanography 48(3): 995-1009.